Università
Ca'Foscari
Venezia

Corso di Dottorato di ricerca in
SCIENZA E GESTIONE DEI
CAMBIAMENTI CLIMATICI
Stream di Climatologia Dinamica

ciclo XXX

Tesi di Ricerca

Interactions between ice shelves and ocean in Antarctica:

grounding line dynamics and ocean properties

Settore Scientifico-disciplinare di afferenza: FIS/06

Coordinatore del Dottorato
ch. prof. Carlo Carraro

Supervisori
Dr. Florence Colleoni
Dr. Dorotea Iovino
Dr. Simona Masina

Dottorando
Enea Marco Montoli
Matricola 956161

Contents

Abstract

The collapse of Antarctic ice shelves and the related shrinking of the Antarctic ice sheet induced by the loss of buttressing is projected as a consequence of ongoing and future climate changes. One of the area of major concerns is the West Antarctic Ice Sheet, especially because of its unstable dynamical conditions, being a marine ice sheet grounded on a bedrock mostly characterized by a retrogade slope.
By means of idealized numerical experiments performed with both GRISLI and with the finite-elements state-of-the-art ice-flow model Úa, the impacts of different existing ocean basal melting formulations on the dynamics of the grounding line are investigated.
Running conceptual simulations on idealized topographies, is investigated the interplay between different pre-existing formulations of basal melting, changes in the sub-ice-shelf bedrock morphology, variations of the climate forcing and calving rates in determining grounding line evolution. One of the main findings is that, in cold climate conditions, ocean basal melting completely takes over calving in driving grounding line dynamics. On the other hand, in warmer climates, the contribution of calving is no more negligible in terms of grounding line evolution and, depending on the initial grounding line position, the calving process acts as a positive/negative feedback on grounding line migration. Also, the 1D plume model by Jenkins(1991) is coupled to both GRISLI and Úa to evaluate its performance on the entire Antarctica Ice Sheet and on the most sensitive glaciers in Antarctica (Pine Island and Totten Glacier). The sensitivity of Pine Island and Totten Glacier to the various ocean basal melting formulation is tested using ocean temperature and salinity observed in the vicinity of those glaciers. The choice of an ocean basal melting formulation largely influence the grounding line migration and the ice discharge rate to the ocean. Moreover, the coupled 1D plume model represents, in comparison with observations, the most robust and accurate formulations among all the ones tested.

Thesis overview

The first chapter presents a brief overview of the Antarctic Ice Sheet features and its interactions with the atmosphere and the surrounding Ocean. A short review of the fundamental equations describing ice dynamics, a detailed summary of ice-shelf dynamics and an overview on the Marine Ice Sheet Instability Theory is also provided.
The second chapter explores the methods of this Ph.D. thesis, illustrating the employed ice-sheet models and the tested ocean basal melting formulations. In particular, a special focus is given to a coupled 1D ocean basal melting plume model, specifically developed and coupled in this thesis.
In the third chapter, by means of idealized experiments, the competition between ocean melting and calving in driving grounding line migration is investigated, along with the impacts of different climate forcings.
The Pine Island and Totten Glacier sensitivity to various ocean basal melting formulations is presented in the fourth chapter, where are evaluated the impacts of the melting formulations on grounding line migration and ice discharge to the ocean. Finally, the limitations and the implications of this Ph.D. thesis are discussed in the last chapter, along with the future perspective of this work.

Scientific motivations and questions The retreat of Antarctic ice shelves and the related shrinking of the Antarctic Ice Sheet (AIS) induced by the loss of buttressing is projected as a consequence of ongoing and future climate changes.
One of the area of major concerns is the West Antarctic Ice Sheet (WAIS), inducing an unstable dynamical behaviour, mostly grounded on a bedrock located below sea level and characterized by a retrogade slope (Schoof 2007). Pine Island Glacier (PIG), which has been found to be the largest contributor to sea-level rise (SLR) from the WAIS in the recent years (Shepherd 2001, Park 2013), is of particular interest for the evolution of the AIS. Similarly to PIG, Totten Glacier, characterized by the largest thinning rate in East Antarctica, has an estimated potential contribution to SLR of at least 3.5 m (Li et al. 2015, Greenbaum et al. 2015), has also been evidenced as an area to monitor. Recent projections shows that by 2100, some of the ice shelves would have partially collapsed, due to both ocean warming impacting on the grounding line stability of the ice shelves and marine terminating glaciers and to an increase in surface melt (DeConto & Pollard 2016).
The interactions between ocean and ice shelves generate basal melting, which is one of the key process influencing the grounding line dynamics and the ocean circulation in the polar areas. However, despite its importance, there is still no clear consensus about which formulations of ocean basal melting, among the existing ones (Hellmer & Olbers. 1989, Jenkins 1991, Martin et al. 2011, Pollard & DeConto 2012) has to be considered the most robust and reliable to model those interactions within stand-alone ice-sheet models.
In between those simple parameterization and the coupling with an ocean model, there exist some ocean melting formulations that retain the essential physics of the ice-ocean interaction without a significative increase in the computational cost (Jenkins, 1991; Helmer and Olbers, 2009). In this thesis, the 1D ocean basal melting plume model by Jenkins (1991) is developed and coupled to two ice-sheet models.
Along with basal melting, calving also has a major role in the evolution of an ice sheet, although the description of the dynamic of the calving front of ice sheets and glaciers,

is still poorly constrained and understood (Peyaud 2006, Levermann & Joughin 2012). By means of numerical experiments performed with the GRISLI ice-sheet model (Ritz et al. 2001), the Úa ice-flow model (Gudmundsson 2012) and with a coupled 1D ocean basal melting plume model, the thesis adresses the following scientific questions:

- What is the relative importance of calving and ocean basal melting on the grounding line evolution?
- How does the mean background climate state affect those processes and thus the grounding line evolution?
- What is the impact of different ocean basal melting formulations on:
  - the rate and magnitude of basal melting induced by the ocean in the cavities
  - the magnitude of grounding line migration

INTRODUCTION

1.1 Antarctica: ice and water

An ice sheet is defined as a mass of ice lying on bedrock and greater than $50,000\ km^2$ (Douglas Benn 2010). At present, the only existing ice sheets are located in Antarctica and in Greenland. An ice sheet is generally divided in three different regions, depending on the ice flow regime and on the ice being grounded or floating (Greve & Blatter 2009).

- A grounded inner part, characterized by ice flowing because of internal deformation and, depending on ice basal temperature, by sliding at the base.
- Ice-streams, characterized by fast-flowing grounded ice, mostly driven by horizontal longitudinal stresses.
- Ice shelves, the floating extensions of an ice sheet, characterized by the same flow regime as ice streams, except at the base where no friction occurs (basal drag equals zero).

The transition area from which the ice starts to float is called the grounding line (or grounding zone), and its dynamics is of particular importance for the evolution and the stability of an ice sheet (Schoof 2007,Weertman 1974).

1.1.1 The Antarctic Ice Sheet

The Antarctic Ice Sheet is the largest ice sheet on Earth with an area of 13.5 million km^2 and a volume of 25.4 million km^3, equivalent to circa 60 m of equivalent sea-level (mSLEFretwell et al. 2013). The AIS can be divided in three parts. Two main chuncks of ice separated by the Transantarctic mountains: the larger East Antarctic Ice Sheet (EAIS, about 54 mSLE) and the smaller West Antarctic Ice Sheet (WAIS, about 6 mSLE). The third part is the Antarctic Peninsula, a collection of outlet glaciers and ice shelves currently dynamically independent from the WAIS (figure 1.1)
The EAIS can be roughly described as a flat dome with a mean elevation of 2,500 m and with a descending ice flow towards the coasts and across the Transantarctic Mountains and with an ice discharge in the ocean gathered in several big ice streams (Fretwell et al. 2013, Lythe C. & Vaughan 2001). On the other hand, the WAIS has a more complex structure, with three prominent ice domes related to three main catchment basins: the Weddel, the Ross and the Amundsen Sea sectors (Zwally et al., 2015). Ice flowing from the first two basins is mainly discharged in the Ronne and the Ross ice shelves, respectively, while the ice coming from the Amundsen Sea catchment area is drained by Pine Island Glacier, Thwaites Glacier and several other smaller ice streams and outlet glaciers (figure 1.1) (Bindschadler 2006). From extension and volume point of view, most of the EAIS is considered to be a stable feature of the AIS, even during the past warmest interglacial periods (e.g. Marchant 2002, Siegert 2008, Pollard & DeConto 2009). On the opposite, the largely marine-based WAIS is thought to be more vulnerable to climate variability. Marine records sediment from the Ross Sea Project ANDRILL have shown that the WAIS collapsed frequently at least over the past 5 Myrs (Naish et al 2009, Pollard and DeConto 2009). This is because contrary to the EAIS, the WAIS is mostly grounded on a bedrock below sea level and thus potentially subjected to the

Marine Ice Sheet Instabilty in response to ocean warming (Fretwell et al. 2013, Schoof 2007, Mercer 1978).

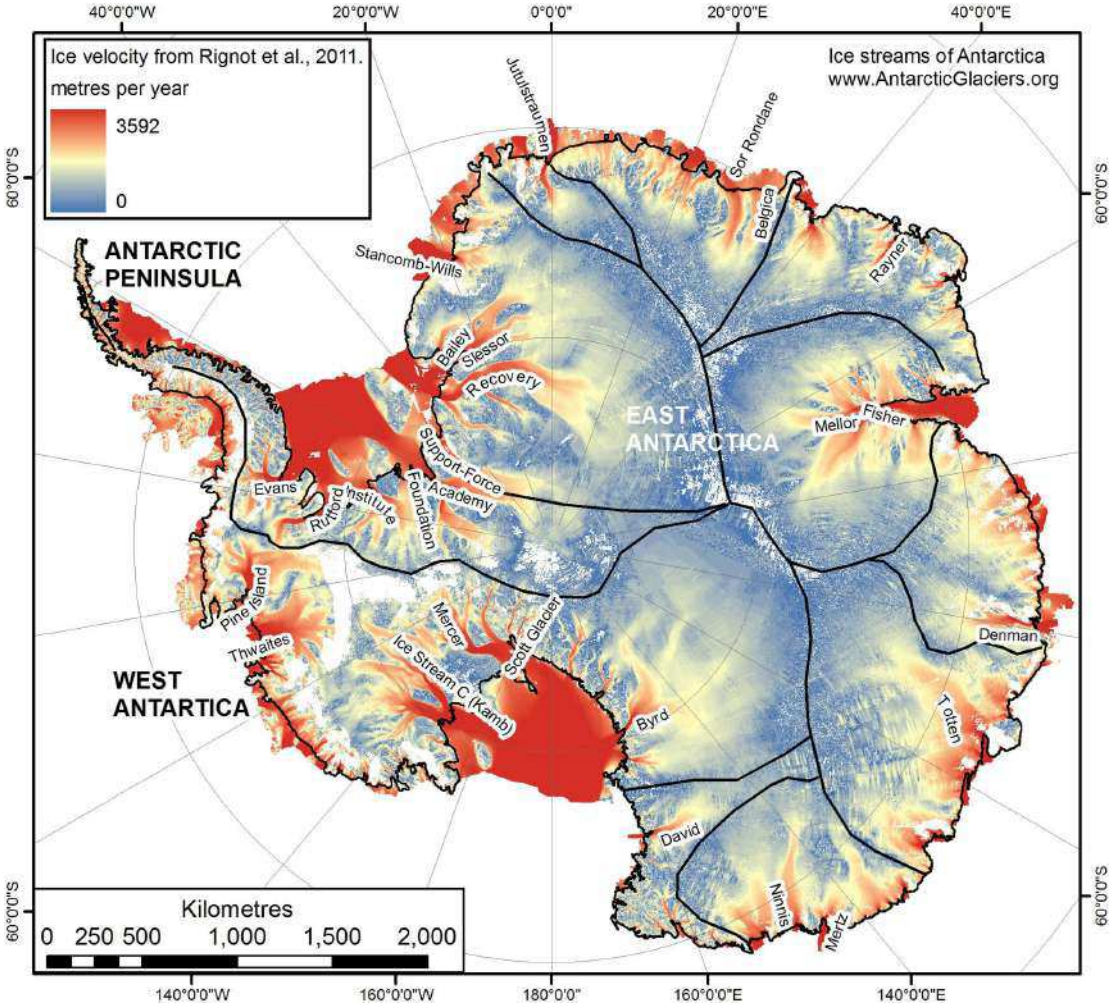

Figure 1.1: *Observed ice flow velocities and geographical description of Antarctica. The drainage basins are separated by thick black lines. After Rignot & Scheuchl. 2011*

1.1.2 Interactions between the Antarctic Ice Sheet and Climate

The Southern Hemisphere polar areas are deeply different from the Northern Hemisphere polar areas. The southern high latitudes, and hence Antarctica, are thermodynamically quasi-insulated from the rest of the planet by a very intense atmospheric westerly flow and by the oceanic Antarctic Circumpolar Current. As a result of this low energy transport, together with the high elevation of the AIS, the climate of Antarctica is way much colder and drier than any area of the Arctic region. This explains why the Antarctic Polar Plateau is the coldest place on Earth. The mean annual air temperature at the Russian Vostok Station near the centre of the Antarctic continent is -55.4°C, with summer and winter means of -31.6°C and -66°C respectively (Turner 2005, Douglas Benn 2010). Milder conditions can be found in the coastal regions, with mean annual temperatures around -10 °C. The Antarctic precipitation distribution has a maximum over the low-elevation areas, where travelling low pressures advect mois-

ture from the surrounding open ocean. This moisture is then discharged on surface as winds impact on the ice sheet margins or on the Antarctic mountains. Mean annual precipitation averaged over Antarctica is around 195 mm/yr, but is typically three to five times higher than this along the coasts and at least three times lower on the plateau (Douglas Benn 2010).
Because of low air temperatures, no surface melting occurs in Antarctica, except on the ice shelves and on the Antarctic Peninsula. Consequently, surface mass balance is positive over the entire AIS, and follows essentially the spatial pattern of precipitation (Lenaerts 2012). Another prominent atmospheric feature of the AIS is the intense katabatics wind field, formed by cold, dense air subsiding on the polar plateau flowing down the steep vertical drops along the coast. Katabatic winds reach their highest intensity at the steep edge of the AIS, while in the interior, on the flat area of the polar plateau, the katabatic winds are relatively mild. These descending winds have a huge impact on the AIS and on the surrounding ocean. Due to the persistent blowing from the coasts toward the ocean, katabatic winds, are able to push away the sea ice, opening polynias. The polynias are a source of heat and moisture to the atmosphere but, most importantly, they foster the sea-ice production that impacts the ocean deep water formation(Barber & Massom. 2007). Moreover, in the WAIS and in the Antarctic Peninsula, spring/summer warm dry winds highly impacts on ice shelves stability. These Fohn winds lead to the melting of the ice-sheet surface by blowing away the snow, exposing the darker ice and decreasing the local albedo thus contributing to the creation of melt pools (Lenaerts 2017, et al. 2017).

Around Antarctica, the Southern Ocean extends from the Antarctic continent to the southern reaches of New Zealand and South America, connecting the Indian, Pacific and Atlantic Oceans. The Southern Ocean is of paramount importance for the global circulation and oceanic heat transport. It is also the home of the Antarctic Circumpolar Current (ACC), driven by strong westerly winds and by the temperature differences between the subtropics and the cold Antarctic continent, flows continuously eastward around Antarctica. The ACC is responsible for most of the zonal transport of water masses and for the climate conditions over Antarctica (Orsi S. & Nowlin. 1995). Closer to the Antarctic continent, the wind flow direction changes orientation, reversing from eastward to westward. This Polar Easterlies along the coast drive a narrow coastal current (the Antarctic Along Slope Current) which flows westward against the dominant eastward flowing ACC, also forming the Weddel, the Australian and the Ross Sea gyres. In the Southern ocean three main fronts are generally identified: the Subtropical front (STF), the Subantarctic Front (SAF) and the Antarctic Polar Front (APF). The region between the Antarctic continent and the APF is usually defined as the Antarctic zone, while the region between the APF and the SAF is called the Subantarctic zone. Figure 1.2 shows the interplay of strong zonal currents, meridional flow caused by deep convection, convergences and divergences, and water mass formation and spreading. More specifically, the westerly of winds move the surface waters, north under the influence of the Coriolis Force, thus allowing the upwelling of deep waters. The surface water, cold and dense, sinks at the Polar Front to form Antarctic Intermediate Water (AAIW) (Wüst, 1935), which sinks northward at intermediate depths(McCartney, 1982). Some of the surface water reaches the SAF, where it sinks to form Sub-Antarctic Mode Water (Hanawa and Talley, 2001).

South of the divergence zone, where upwelling takes place, the inflowing North Atlantic Deep Water is transformed into Circumpolar Deep Water and raised to the surface where it interacts with ice and atmosphere (Linny 2016). The surface waters reaching the coastal shallow continental shelves lose buoyancy because of cooling by contact with ice and by collecting the brine rejected during sea-ice formation during winter (Figure 1.19). The surface waters become dense enough to sink and they cascade down the continental shelf (Baines and Condie, 1998; Foldvik et al. 2004) and slope to form the Antarctic Bottom Water (AABW), which spreads around Antarctica (Orsi et al, 1999). The circulation over the shallow continental shelf and under the ice shelves cavity is further described later on, in section 1.3.

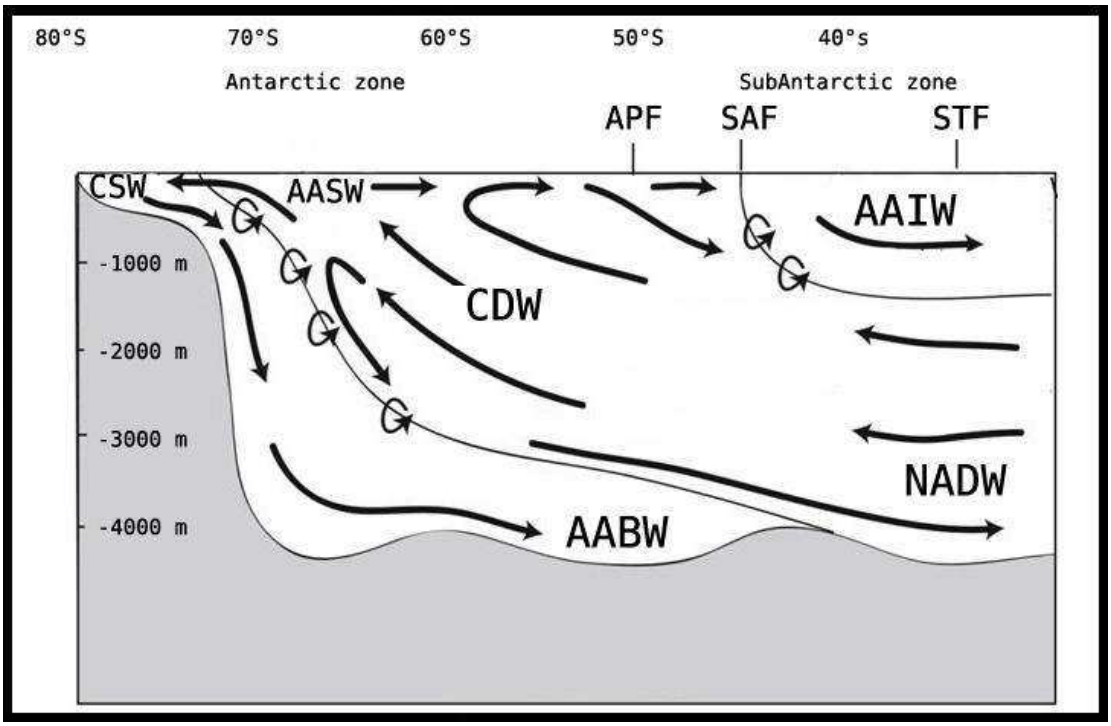

Figure 1.2: *A schematic meridional section for the Southern Ocean showing the main water masses and the simplified meridional circulation. Acronyms: Antarctic Surface Water (AASW), Circumpolar Deep Water (CDW), Antarctic Intermediate Water (AAIW), Antarctic Bottom Water (AABW), North Atlantic Deep Water (NADW), Continental Shelf Water (CSW), Antarctic Polar Front (APF), SubAntarctic Front (SAF) and Subtropical Front (SBF)*

.

The described three-dimensional ocean circulation results in a complex characterization of water masses, as shown from a conceptual cross section for temperature and salinity of the Pacific sector in figure 1.3. The upwelling Circumpolar Deep Water is identified by a band of salty water around Antarctica, to the north and south of which the signature of the fresher downwelling Antarctic Surface Water is observed. In the Pacific sector of the WAIS, Circumpolar Deep Water is found on the continental shelf (Thoma 2008, Wahlin 2010), while in the Weddel Sea, sea-ice formation produces Shelf Water (SW), distinguishable from the Circumpolar Deep Water by an higher salinity.
A meridional temperature gradient in upper-layer represents the downwelling and the relatively warm AASW in the north, while the SW is generally colder (at the seawater

surface freezing point) as a result of the seasonal influence of sea ice growth and of the low atmospheric temperature. The Pacific sector experiences intrusions of CDW along the coasts of WAIS, leading to shelf water masses with higher temperatures than the other polar water masses and thus with potential to melt the ice-sheet.(Thoma 2008, Wahlin 2010, Linny 2016).

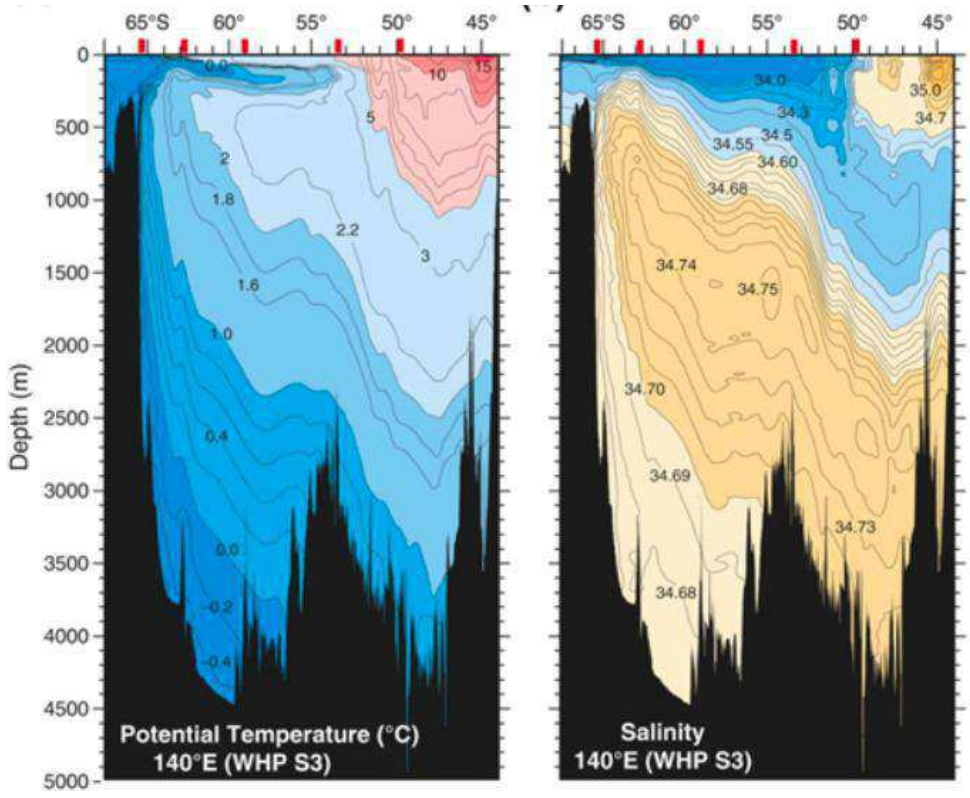

Figure 1.3: *Vertical section of the 140 °E, Pacific Sector (this occean area has been chosen because of its relevance to this thesis). Left: potential temperature (°C). Right: salinity. After Linny 2016.*

1.1.3 Past, present and future

Geological evidence shows that the Antarctic Ice Sheet has changed considerably since 34 million years ago, when the glaciation started (Wilson et al 2013, DeConto 2003). The volume and extension of the AIS has considerably fluctuated during the last 30 million of years, being driven and in turn driving major changes in climate and in the global sea level (Siegert 2008).
For example, during the Last Glacial Maximum (21000 years ago), the AIS stretched up to the continental shelf edge. Geomorphological evidences collected on the continental shelf have proven the past existence of paleo ice streams during the LGM, indicative of a dynamic, sensitive and fast-flowing ice sheet (Cofaigh & Morris 2002, Gooledge et al. 2012, 2014). However, for years the Antarctic Ice Sheet has been considered insensitive to global warming (Solomon et al. 2007). This was partially due to the difficulties and uncertainties in estimating the total mass balance of the AIS. Thanks to recent evidence from the WAIS showing a dynamical response to ongoing climate changes (Scambos 2000, Turner 2005, Naish et al. 2009, Pritchard et al. 2012, Favier & Gudmundsson

2014) several speculations have been made about a possible irreversible grounding line retreat and a rapid deglaciation in the future (Weertman 1974, Vaughan 2008).

This hypothesized rapid ice-sheet retreat of the WAIS is related to the Marine Ice Sheet Instability theory (MISI), stating that ice flow rates and migration of grounding line are strongly coupled, and potentially subject to destabilizing feedbacks (see section 1.2.2). Collected data are, in general, not enough and scarsely distributed to asses if the current evolution of the entire WAIS is influenced by MISI or not, but recent studies have shown that parts of the WAIS surely are and can respond rapidly to atmospheric and oceanic forcings (Joughin & Medley 2008, Favier & Gudmundsson 2014). In the last two decades many ice shelves in the Antarctic Peninsula have retreated or collapsed, leading to an increase in ice discharge from the interior (Rott & Nagler. 1996, Scambos 2004). However, the 20th century retreat of large ice shelves (e.g. the recent calving of Larsen C) do not sistematically result from the MISI but from different processes, as for example the formation of meltpond at the ice shelf surface or mechanical weaknesses (Scambos & Fahnestock. 2003, Kulessa 2017).

Neverthless farther south from the Antarctic Peninsula the WAIS, with a potential sea-level-rise future contributions of 3 metres (Bamber 2009), is showing a strong response to the ongoing climate changes (Joughin & Medley 2008, Favier & Gudmundsson 2014). Within the last decades evidence of ice stream thinning and acceleration have been collected (Shepherd 2001, Joughin & Holland 2010). The most dramatic changes have occured on the largest ice stream, Pine Island Glacier (figure 1.1), but changes have been observed for the other major ice streams. Currently Pine Island Glacier has been considered responsible for 20 percents of the total ice loss from the WAIS over the 20th century, with a grounding line retreat of almost 1 km per year between 1992 and 2011 (Rignot 1998, Rignot & Scheuchl 2014). This retreat has been caused mainly by the thinning of the floating part of the glacier accompanied by acceleration of the flow caused by a reduced buttressing (Rignot & Thomas. 2002, Joughin 2003, Rignot & Meijgaard 2008).

These changes were attributed mostly to increase in ocean basal melting due to more frequent intrusions of CDW (Jenkins 2010, Jacobs 2011). Moreover, the grounding line of Pine Island Glacier is currently located over a steep retrograde portion of the underlying bedrock, that, as shown in Favier & Gudmundsson 2014, could represent the main factor determining its future irreversible retreat (figure 1.4). Another sensitive and particularly active area is Totten Glacier, East Antarctica (1.1). Totten Glacier is the primary outlet of the Aurora Subglacial Basin, discharging around 70 Gt/yr and characterized by the largest thinning rate in EAIS (around 0.7 m/yr at the grounding line) with a detected grounding line retreat of 1 to 3 km in the last 17 years (Khazendar 2013, Li et al. 2015). The thinning has been attributed to an enhanced ocean basal melting due to intrusion of CDW, similarly to what is in act in the Amundsen Sea (Greenbaum et al. 2015).

Projections for the future of Antarctica shows that by 2100, some of the ice shelves would have probably partially collapsed, due to both ocean warming impacting on the grounding line stability under the ice shelves and also because of an increase in surface melting. The contribution to sea-level rise has been estimated to 0.30 - 1 meter by 2100 and more than 13 metres by 2500 considering the RCP 2.6 and RCP 8.5 scenarios. (figure 1.5, Cornford & Vaughan 2015, DeConto & Pollard 2016).

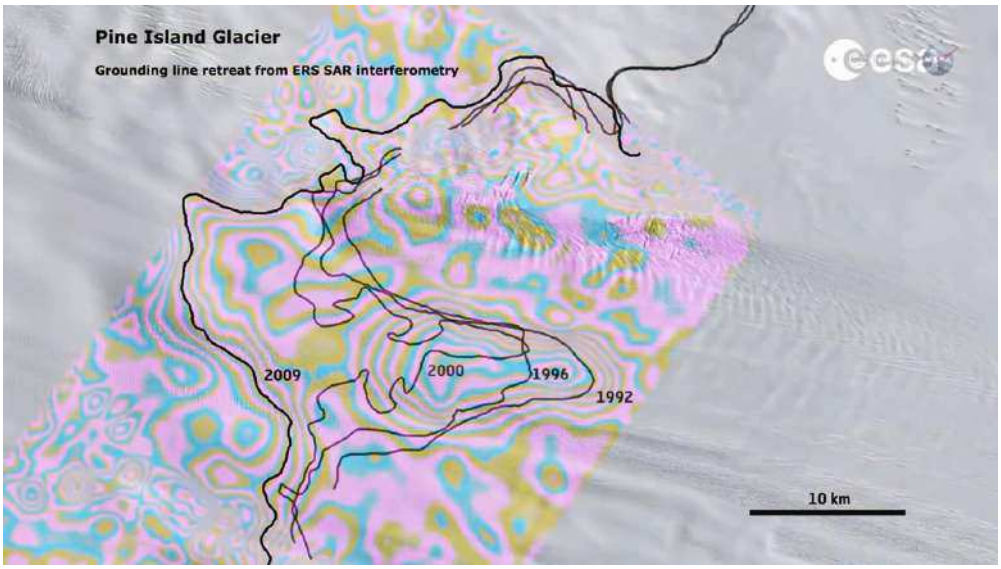

Figure 1.4: *Observed grounding line migration for Pine Island Glacier from 1992 to 2011.From Joughin & Holland 2010 and ESA*

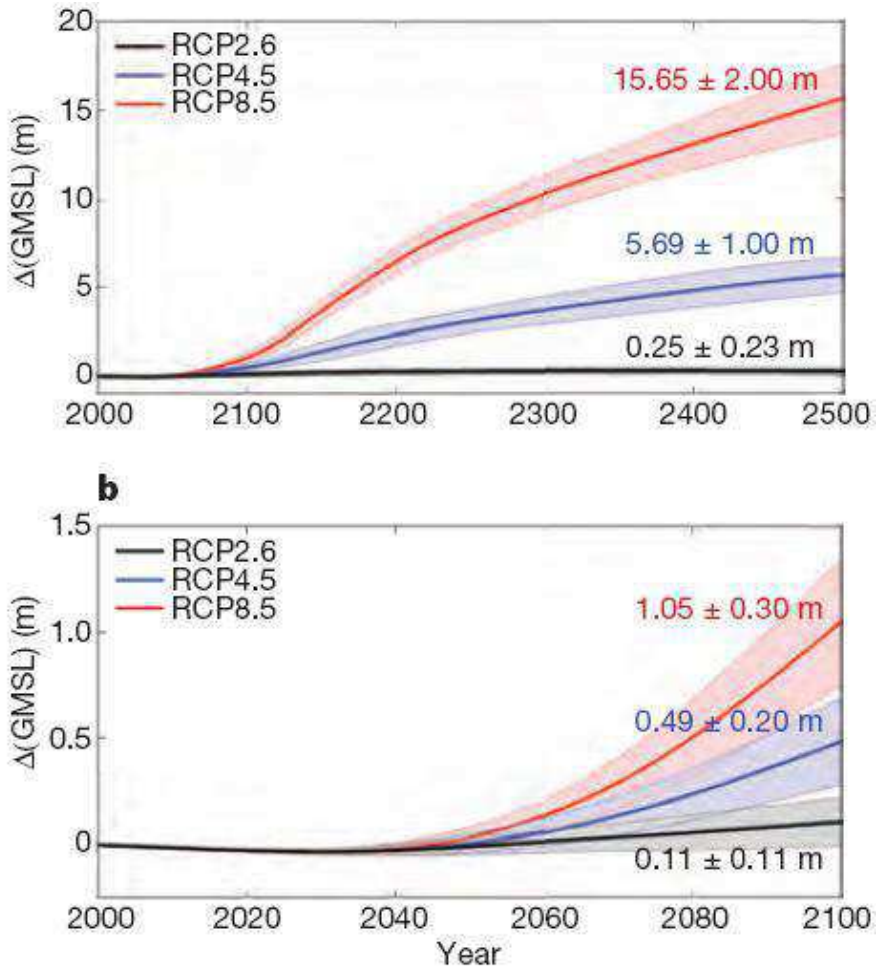

Figure 1.5: *a, RCP ensembles to 2500. b, RCP ensembles to 2100. Changes in Global Mean Sea Level relative to 2000. DeConto & Pollard 2016*

1.2 Ice dynamics in a nutshell

Ice dynamics describes the motion of large bodies of ice considered in first approximation as non-Newtonian, incompressible, viscous fluid ultimately driven by gravity, temperature and resistance at the bottom. This section focus is on ice sheet dynamics.

1.2.1 Fundamental equations

The fundamental equations governing the dynamics and the thermodynamics of an ice sheet can be obtained combining the conservation of mass, momentum and energy to determine velocity $\mathbf{u} = (u, v, w)$:

$$\frac{\partial \rho}{\partial t} + \nabla \cdot (\rho \mathbf{u}) = 0 \tag{1.1}$$

$$\rho \frac{\partial \mathbf{u}}{\partial t} = \nabla \cdot \tau + \rho \mathbf{g} \tag{1.2}$$

$$\rho c \left(\frac{\partial T}{\partial t} + \mathbf{u} \cdot \nabla T \right) = \nabla (\kappa \nabla T) + Q_i \tag{1.3}$$

where ρ is the ice density, τ the stress tensor of deformation, $\mathbf{g}$ the acceleration of gravity, c the heat capacity of ice, T the ice temperature, κ the thermal conductivity of ice and Q_i the deformational heat (Colleoni et al. 2014).
Under the assumption of ice to be incompressible and with constant density, the continuity equation 1.1 can be written as follows:

$$\nabla \cdot \mathbf{u} = \frac{\partial u}{\partial x} + \frac{\partial v}{\partial y} + \frac{\partial w}{\partial z} = 0 \tag{1.4}$$

Then, vertically integrating equation 1.4 from the ice base b to the ice surface s and defining ice thickness h as the elevation minus the ice base elevation ($h = s - b$), a vertically integrated equation for mass conservation is obtained.

$$\frac{\partial h}{\partial t} + \frac{\partial (h\, u)}{\partial x} + \frac{\partial (h\, v)}{\partial y} = s_m - b_m \tag{1.5}$$

where s_m and b_m represent the surface mass balance ($s_m = accumulation - melting$) and the melting at the base, respectively (Greve & Blatter 2009).
Equation 1.5 describes the time evolution of an ice mass: it relates the time variation of ice thickness to ice flow velocities and to the surface mass balance and the basal processes (calving, although its importance as an ice sink, does not enter directly in equation 1.5).
Applying dimensional scaling considerations with typical values of ice-sheet horizontal extension and thickness (Greve & Blatter 2009), the acceleration terms in equation 1.2 can be neglected, obtaining the following simplified version for the conservation of momentum, called the *Stokes Equations*:

$$\frac{\partial \tau_{xx}}{\partial x} + \frac{\partial \tau_{xy}}{\partial y} + \frac{\partial \tau_{xz}}{\partial z} = 0 \tag{1.6}$$

$$\frac{\partial \tau_{yx}}{\partial x} + \frac{\partial \tau_{yy}}{\partial y} + \frac{\partial \tau_{yz}}{\partial z} = 0 \tag{1.7}$$

$$\frac{\partial \tau_{zx}}{\partial x} + \frac{\partial \tau_{zy}}{\partial y} + \frac{\partial \tau_{zz}}{\partial z} = \rho g \tag{1.8}$$

In order to dynamically describe the evolution of an ice mass, in addition to the aforementioned equations 1.6 to 1.8, we also need a rheological constitutive law for ice that describes how it deforms under an applied stress and at a given temperature. The general constitutive law for ice, called Glen's law (Greve & Blatter 2009), can be written as:

$$\mathsf{D} = A\left(T'\right)\tau_\star^{n-1}\tau^{\mathrm{D}} = \frac{1}{\eta}\tau^{\mathrm{D}} \tag{1.9}$$

where D is the strain-rate tensor, τ^{D} is the deviator stress tensor, T' the temperature corrected for the melting point dependence on hydrostatic pressure, $\tau_\star$ is the effective stress and η the ice viscosity. The n exponent in the Glen's law is usually set to 3 (Greve & Blatter 2009).
The pressure-melting point corrected temperature T' is calculated from the surface s to the base b of the ice sheet, as given by:

$$T' = T + T_{\mathrm{p}} = T + 9.76 \cdot 10^{-8}\rho g\left(s - b\right) \tag{1.10}$$

The effective stress has the following expression:

$$\tau_\star = \sqrt{\frac{1}{2}\mathrm{tr}\left(\tau^{\mathrm{D}}\right)^2} \tag{1.11}$$

The so-called rate-factor $A\left(T'\right)$ follows an Arrhenius law and can thus be expressed as:

$$A\left(T'\right) = A_0 \exp\left(-\frac{E_0}{RT'}\right), \tag{1.12}$$

where A_0 is a constant coefficient, E_0 is the activation energy and R is the universal gas constant (Greve & Blatter 2009).

To obtain the most comprehensive description of ice flow, the Stokes equations (1.6 to 1.8) and the Glen's law (1.9) must be combined, through the relationship relating stress deviator τ^{D} to pressure p.

$$\tau = \tau^{\mathrm{D}} - p\,\mathsf{I}, \tag{1.13}$$

where I is the second order unit tensor and p is hydrostatic pressure.
After some manipulations, the set of the *full Stokes equations* for ice dynamics is obtained:

$$\frac{\partial}{\partial x}(2\eta\frac{\partial u}{\partial x}) + \frac{\partial}{\partial y}(\eta\frac{\partial u}{\partial y} + \eta\frac{\partial v}{\partial x}) + \frac{\partial}{\partial z}(\eta\frac{\partial u}{\partial z} + \eta\frac{\partial w}{\partial x}) - \frac{\partial p}{\partial x} = 0 \tag{1.14}$$

$$\frac{\partial}{\partial x}(\eta\frac{\partial u}{\partial y} + \eta\frac{\partial v}{\partial x}) + \frac{\partial}{\partial y}(2\eta\frac{\partial v}{\partial y}) + \frac{\partial}{\partial z}(\eta\frac{\partial v}{\partial z} + \eta\frac{\partial w}{\partial y}) - \frac{\partial p}{\partial y} = 0 \tag{1.15}$$

$$\frac{\partial}{\partial x}(\eta\frac{\partial u}{\partial z} + \eta\frac{\partial w}{\partial x}) + \frac{\partial}{\partial y}(\eta\frac{\partial v}{\partial z} + \eta\frac{\partial w}{\partial y}) + \frac{\partial}{\partial z}(2\eta\frac{\partial w}{\partial z}) - \frac{\partial p}{\partial z} = \rho g \tag{1.16}$$

The viscosity η in the *full Stokes equations* is dependent on temperature (via the flow law coefficient $A\left(T'\right)$), also melting and sliding at the base are related to ice temperature. Sliding and melting occur, at the first order, depending whether or not the ice sheet base has reached the melting-point temperature. Thus, to have a satisfactory description of ice dynamics, the evolution of ice vertical temperature has to be taken into account.

The ice-mass thermodynamics evolves according to equation 1.3 where three distinct terms can be identified:

$$Advection : \mathbf{u} \cdot \nabla T \tag{1.17}$$

$$Diffusion : \nabla(k \nabla T) \tag{1.18}$$

$$Sinks/sources : \mathrm{Q}_i \tag{1.19}$$

Using the same scaling considerations applied to the momentum conservation equations, the horizontal heat conduction terms can be neglected, obtaining the following simplified energy conservation equation:

$$\rho c \left(\frac{\partial T}{\partial t} + \mathbf{u} \cdot \nabla T \right) = \frac{\partial T}{\partial z} \left(\kappa \frac{\partial T}{\partial z} \right) + Q_i \tag{1.20}$$

In order to solve equation 1.20, upper and lower surface boundary conditions are needed. At the ice sheet surface, the air temperature is prescribed as an upper Dirichlet boundary condition, while the boundary condition at the bottom is of the Neumann type.
At the ice sheet base, the contribution of the geothermal heat flux G_h, along with heating by sliding friction, enters the vertical gradient of temperature at the base

$$\frac{\partial T}{\partial z} = \frac{\mathrm{G}_h + \tau_b \cdot \mathbf{u}_b}{k} \tag{1.21}$$

where τ_b is basal drag and u_b is the basal velocity, (Paterson 1994).
The basal velocity can be expressed through two formulations. One, as in Rutt(2009), is

$$\mathbf{u}_b = -B_{sl} \rho g h \nabla s \tag{1.22}$$

with B_{sl} a sliding coefficient, set to zero if a no-slip condition is wanted and the composite term $\rho g h \nabla s$ that defines, for slow-flowing ice, an expression for the drag τ_b at the ice-sheet base

$$\tau_b = \rho g h \nabla s \tag{1.23}$$

Another formulation for the velocity at the base was developed by Weertman 1957,

$$\mathbf{u}_b = -k_{sl} (\rho g h)^3 (\nabla s \cdot \nabla s)^{\frac{1}{2}} \frac{\nabla s}{N} \tag{1.24}$$

with k_{sl} an adimensional coefficient and N the effective pressure, expressed as:

$$N = \rho g h - \rho_W \tag{1.25}$$

where ρ_W is the meltwater density at the base of the grounded ice.
Using effective pressure N, the basal drag related to the different flow regimes can also be expressed as:

$$Slow : \tau_b = fN \tag{1.26}$$

$$Fast : \tau_b = -c_f N \mathbf{U} \tag{1.27}$$

$$Floating : \tau_b = 0 \tag{1.28}$$

Where f is a coefficient for slow-flowing ice, c_f for fast-flowing ice and $\mathbf{U}$ is the vertical-averaged ice velocity (Paterson 1994, Greve & Blatter 2009).

1.2.2 Ice shelves dynamics and Marine Ice Sheet Instability

In Antarctica ice shelves cover the 44 percents of the entire coast line, with a total area of 1540000 km^2 (Fretwell et al. 2013). Although to the first order ice shelves do not contribute directly to ocean mass increase (Jenkins & Holland. 2007), their removal would drastically affect the discharge of ice from the ice sheet interior. This concern was first raised in 1978, when Mercer proposed that rising temperatures could have catastrophic consequences on the WAIS, triggering the collapse of several ice shelves (Mercer 1978).
Mercer proposed a threshold for ice-shelves stability based on the mean annual air temperature and he suggested that peripheral ice shelves actually play a major buttressing role for discharge of inland ice. Hence, their break up could accelerate the water discharge, leading to rapid collapse of the WAIS and to a consequent substantial sea level rise. This hypothesis is at the foundations of the Marine Ice Sheet Instability theory.

Ice shelves dynamics When the ice flows toward the coasts and meets a sufficiently cold ocean, the ice does not melt immediately and if accumulation is large enough it starts to float, eventually spreading freely or being confined in embayments. An ice shelf is, for most of its area, fully floating and hence characterized by zero basal drag. However, islands or embayments generate resistances to flow through lateral stresses and/or lateral drags at the rocky/icy boundaries (Paterson 1994, Douglas Benn 2010).
The evolution of an ice shelf is driven by the longitudinal stresses arising from gravitational and buoyant forces in balance with spreading by ice creep, with surface/basal mass balance and with calving. When an ice shelf is surrounded by lateral rock/slow-flowing-ice walls or characterised by one/many ice rises is defined as a confined ice shelf. On the other hand, an unconfined ice shelf is defined as an ice shelf freely spreading on open ocean water (Paterson 1994, Douglas Benn 2010, Van der Veen 2017).
This distinction is crucial to determine the effects that the expansion or disintegration of an ice shelf has on the ice sheet dynamics. In fact, the resistance from the lateral walls and ice rises heavily opposes the ice shelf flow, reducing the spreading rate to a lower value than would be observed in the case of a free spreading ice shelf (Van der Veen 2017).
The force balance of a confined ice shelf is typically dominated by lateral resistance that, via strain heating and crevassing at the flowing boundaries, makes the ice softer (lowering viscosity) and increases the velocity gradients at the ice-shelf margins. Moreover, confined ice shelves are also thicker and steeper than unconfined ones, as a result of lateral drag. But, more importantly, the prominent dynamical effect is that drag around ice shelf margins contributes to delay the flow of upstream ice.
This buttressing effect is often described as backpressure, mainly intended and defined as the downglacial integrated resistance to flow associated with lateral drag and resistance from ice rises (Van der Veen 2017). Considering an ice shelf oriented in the x direction the backpressure can be written in the following general form:

$$\sigma_b = \frac{1}{h}\int_x^L \frac{h\tau_s}{W} d\overline{x} \tag{1.29}$$

Here τ_s is the shear stress at the margins, W denotes the half-width of the shelf and $x = L$ is the portion of the shelf considered.

This backpressure reduces the spreading rate $\dot{D}_{xx}$:

$$\dot{D}_{xx} = (\frac{\tau^f_{xx} - \sigma_b}{A(T')})^n \tag{1.30}$$

where τ^f_{xx} is the stretching stress for an unconfined ice shelf on which the driving stress is balanced entirely by gradients in longitudinal stress and is given by

$$\tau^f_{xx} = \frac{\rho g}{2}(1 - \frac{\rho}{\rho_W})h \tag{1.31}$$

In the case of a thinning or a shortening the ice shelf, the spreading rate (by creep) $\dot{D}_{xx}$, for a given ice thickness, increases.
This increase results from a decrease in the backpressure mainly because:

- if an ice shelf thins the available surface on which lateral drag can act reduces, as well as the ice shelf depth, possibly causing the ungrounding of pinning points.
- a less extended ice shelf has smaller lateral surfaces on which friction can act

However, independently from the causes, a variation of creep rate implies in turn a change in thickness. To a deeper understanding of the creep rate-thickness relation it is instructive to go back to the continuity equation 1.1 (in the x direction)

$$\frac{\partial h}{\partial t} = -\frac{\partial (h\,u)}{\partial x} + s_m - b_m \tag{1.32}$$

expanding $\frac{\partial (h\,u)}{\partial x}$ and using 1.30, 1.31 we obtain the continuity equation in the following form:

$$\frac{\partial h}{\partial t} = \underbrace{-\frac{u \partial h}{\partial x}}_{\text{Advection}} \underbrace{- h \left(\frac{Ch - \sigma_b}{2A(T')} \right)^n}_{\text{Creep thinning}} + \underbrace{s_m - b_m}_{\text{Surface-Basal mass balance}} \tag{1.33}$$

where C is:

$$C = \frac{\rho g}{2}(1 - \frac{\rho}{\rho_W}) \tag{1.34}$$

Equation 1.33 is valid for ice flow in general and can thus be specifically applied only at the grounding line without loss of any generality.
Thus the evolution of an ice shelf is ultimately determined by the ice fluxes at the grounding line, by creep deformation thinning and by accumulation, surface and basal melting (Van der Veen 2017).

Marine Ice Sheet Instability The creep thinning term $h \left(\frac{Ch - \sigma_b}{2A(T')} \right)^n$ represents the key to understand how MISI works and in particular the ice-thickness-dependent feedback.
Feedbacks acting on the ice-shelf evolution because of MISI are schematized in figure (1.6).

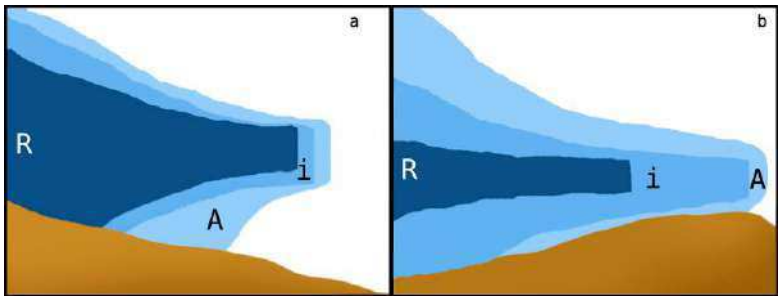

Figure 1.6: *Interaction between grounding-line migration and basal topography. The panel on the left represents a stable configuration with the bed sloping downward from the ice-sheet interior. The panel on the right represents an unstable situation. Profiles labeled i represent the initial geometry, and profiles labeled A and R represent the geometry after advance and retreat, respectively.*

The left frame of figure 1.6 shows a seafloor that slopes downard from the ice-sheet interior. In the case of an advancing grounding line due to, for example, an increase in ice advection, the ice thickness at the grounding line increases, leading to a larger creep thinning, which slows the rate of advance. On the contrary, with a retreating grounding line, creep thinning decreases, thus delaying the retreat. For this kind of geometry, the interaction between creep thinning and ice thickness provides a negative feedback, slowing both the advance and retreat of the grounding line.
On the other hand, the right frame of figure 1.6 illustrate a situation where a positive feedback occurs. The advance of the grounding line leads to a decrease in creep thinning allowing the grounding line to advance further, while a retreat results in increased creep thinning and accelerated retreat (Van der Veen 2017).
The above simplified system is complicated by the eventuality that the ice shelf may be confined and thus being more stable to both grounding line retreat or advance. As an example, considering a confined ice shelf with the calving front located mostly at the end of the confining embayment, an advance of the grounding line would result in a less expanded ice shelf (because the floating area decreases). Thus, reminding the backpressure expression 1.29, an advancing ice sheet reduces the backpressure at the grounding line, resulting in a larger creep thinning, that slows down advance. On the contrary, a retreat of the grounding line increases the backpressure, which slows down the retreat. If the ice shelf becomes sufficiently large, the position of the grounding line may stabilize (Benn et al. 2014, Van der Veen 2017).
The first attempt to analytically describe the behaviour of the grounding line was made in 1974 by Weertman, who derived an expression for the ice flux at the grounding line for a 2D ice sheet evolving on a constant-slope-isostatically-adjusting bedrock below sea level (Weertman 1974). In this setting, a small advance of the grounding line increases the size of the ice sheet, its grounded portion and the size of the grounded accumulation basin, consequently raising the amount of precipitation accumulated up the grounding line. Weertman (1974) proposed that, when the increase in total accumulation exceeds the increase in ice flux across the grounding line, the ice sheet continues to grow until it reaches the edge of the continental shelf break. Viceversa, when the total accumulation is less than the ice flux across the grounding line, the ice sheet will retreat.
That is, steady grounding line positions can be found by comparing the ice flux across the grounding line with the integrated upstream accumulation. Following this assumption, an ice sheet resting on a below-sea-level horizontal bedrock before isostatic adjustment

is unherently unstable. Depending on how deep the bed is below sea level, a small perturbation in grounding line position can cause:

- a continued grounding line retreat and marine ice sheet disappeareance;
- a grounding line and ice sheet advance up to the continental shelf break.

Viceversa, for a bed sloping away from the ice divide, a stable configuration is possible (Weertman 1974, Van der Veen 2017).
The first comprehensive analysis of the grounding line stability has been presented by Schoof in 2007. In Schoof (2007), applying a boundary layer and a linear stability analysis, an updated and model-oriented expression for the ice 1D flux across the grounding line is derived. The main result consists in showing analytically that discrete equilibrium states for the grounding line exist and are determined by balance bewteen discharge flux across the grounding line and total upglacier accumulation (figure 1.7, Schoof 2007). Moreover, in 2013, Pegler (2013) suggested a new mechanism for how the position of the grounding line can be established in situations where a marine ice sheet is confined laterally. The authors found, in strong contrast to Weertman (1974) and Schoof (2007), that the position of the grounding line is determined independently of the dynamics of the sheet upstream of the grounding line, and depends only on geometry and the flux delivered into the ice shelf.

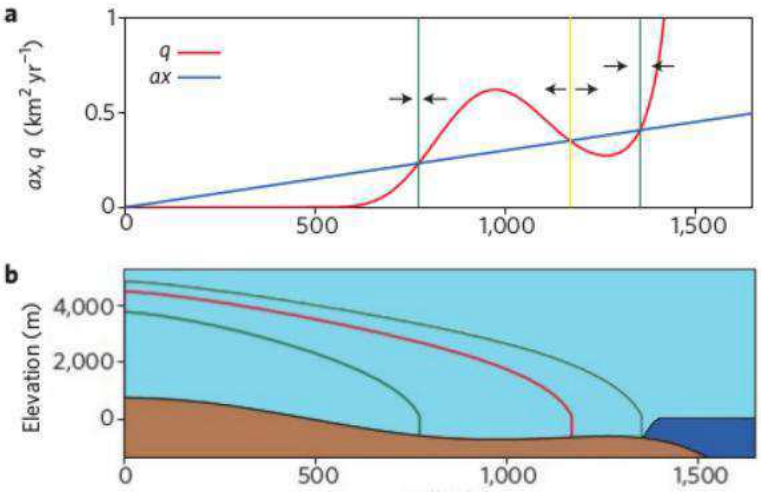

Figure 1.7: *Equilibrium states and their relation with ice fluxes at the grounding line and total accumulation according to Schoof(2007). Accumulation (qx), ice fluxes at the grounding line (q). After Joughin & Alley 2011*

In parallel with the analytical studies of Weertman and Schoof, the ice-sheet modeling community has tackled the grounding line problem using a wide variety of numerical models. These models differ in their approximations of the flow of the grounded portion, boundary conditions at the grounding line (e.g. prescribing the ice fluxes across the grounding line using the Schoof equation adapted in 3D for ice flux at the grounding line), numerics and other factors (Schoof 2007, Van der Veen 2017). The early study of Van der Veen suggested that marine ice sheets may be more stable than supposed and that the removal of fringing ice shelves does not lead to complete disintegration of the ice sheet (Van der Veen 1985). Neverthless the inner instability of marine ice sheet was reaffirmed by Durand 2009 who showed unstable behaviour on an upsloping bed using

a full stokes numerical model. On the other hand, Nick et al. (2010) showed that the grounding line dynamics is less sensitive to bedrock topography as previously suggested, resulting in stable position also on retrograde bed slopes, in agreements with Gudmundsson 2012. This was confirmed also by Goldberg and Schoof (2017) that considered the flow of laterally confined marine-terminating outlet glaciers. They found that, by contrast with unbuttressed marine ice sheets, ice flux can decrease with increasing depth to bedrock at the grounding line, reversing the usual stability criterion for steady grounding line location. Thus allowing stable grounding line states also on retrograde bedrock slopes.
In general, modeling studies have produced contrasting results and no general statement could be made about the feedbacks between grounding line dynamics yet. The reason for several studies appearing inconclusive is related to the fact that there is a heavy dependence on how grounding line is numerically implemented.
Vieli and Payne (2005) assessed the strong effect that computational grid size has on how the grounding line dynamics is simulated and in particular, for finite differences models, that the numerical implementation has a huge impact on these feedbacks (Docquier & Pattyn. 2011).
In the context of the Marine Ice Sheet Model Intercomparison Projects (MISMIP, MISMIP3D, MISMIP+) several ice-sheet models, with topography and model fields varying only in one horizontal dimension, were compared in terms of their grounding-line dynamics with the semi-analitic solution provided by Schoof (Schoof 2007). What emerged from the benchmarks is that steady-state grounding line positions strongly differ depending on resolution, stress approximation and numerical methods of spatial discretization (Pattyn 2012, Pattyn 2013).
The MISI has been presented as a theory to describes how an ice-shelf-sheet system responds to a change of the initial grounding line position in response to a given perturbation. There are several possible perturbations able to induce migration of the grounding line and consequent positive or negative feedbacks. As seen above, as the grounding line migrates forward because of a change in ice advection, the size of the catchment area changes together with an increase in total accumulation triggering a positive feedback that amplifies the distance of migration.
On a centennial time scale, also large eustatic changes in sea level provide the most powerful stimulus for grounding line migration. Together with an immediate shift of the grounding line, in order to preserve hydrostatic equilibrium, the possible formation or disappearance of ice rises can stabilize or destabilize the ice shelf.
On decadal time scale, two effective perturbations are in act: the breakup of floating ice shelves with the following release of backstress and the increase in submarine melting associated with intrusion of realtively warm ocean water under the subshelf cavities. In the last decades, growing consensus is pointing in the direction of ice-ocean interaction as the main responsible for the observed changes in Antarctica (see section 1.3 and Thomas 1973, Thomas 1979, Pritchard et al. 2012, Rignot et al. 2013, Depoorter et al. 2013, Van der Veen 2017)

Calving Calving is considered to be the fastest way through which ice is rapidly transferred from grounded ice to a surrounding water environment (Douglas Benn 2010). The calving process involves the detachment of blocks of ice from an ice mass to form icebergs,

ranging in size from small blocks to large tabular icebergs (Paterson 1994, Douglas Benn 2010).
A wide range of calving environments exist: from small icebergs typical of the Greenland Ice Sheet to the large tabular icebergs of Antarctica. Moreover, significant observed distinctions amongst icebergs populations come also from the ice mass being cold, temperate, grounded or floating (*e.g.* temperate glaciers do not form floating tongues). In terms of calving rates Greenland is characterized by very high rates while Antarctica by very low and episodic events (Douglas Benn 2010. In particular, calving by the AIS is usually characterized by long period of inactivity, puntuacted by the detachment of large tabular icebergs, originating giant rifts cutting through the ice shelves (Glasser & Scambos 2008). Currently calving accounts for almost 1000 Gt/yr ($3mm/yr$) of mass loss from the AIS (see figure 1.10, Rignot et al. 2013).
The mechanics of calving involves birth and propagation of fractures through the ice, caused by the local stress regime, presence of pre-existing cracks, strength of the ice and of surface meltwater. Yet, the factors controlling calving rates remain a major topic of debate with the need for a physically-based description of the calving process still unsatisfied (Bassis 2011).

1.3 Ice-Ocean interaction

Due to the very low air temperatures at the higher latitudes in the Southern Hemisphere, the current ice sheet mass evolution of Antarctica is not affected much by the atmospheric forcings. Instead, it is strongly influenced by the interaction between the ice and the ocean through basal melting, in particular at the grounding line (Holland & Jenkins 1999, Rignot et al. 2013). It is in fact widely recognized that ocean basal melting is a huge driver of the inland ice sheet changes (Holland et al. 2008). In addition, insulating the continental shelf seas from the polar atmosphere, ice shelves also influence ocean properties and circulation through the release of glacial meltwater (Foldvik & Gammelsrød. 1988).
The interaction between the ocean water masses and the AIS takes place at the boundary between these two systems: within the sub-ice-shelf cavity. The few direct and inferred observations below the ice shelves (Fricker 2001, Lewi & Perkin 1986) have shown the presence of an overturning circulation driven by a thermohaline mechanism usually referred as "*ice pump*" (Lewi & Perkin 1986, Jacobs 1992). As a result of the sloping ice shelf draft and the pressure dependence of the seawater freezing point of seawater, the ambient ocean water is able to melt the ice and to produce, through mixing of melt and ambient ocean water, the colder and less dense Ice Shelf Water (ISW).
Due to its cold temperature and low salinity, the Ice Shelf Water is buoyant in comparison to the generally warmer and saltier ambient ocean water and is hence able to rise along the ascending ice shelf draft entraining ambient ocean water and melting the ice (or forming marine ice through a refreezing process) until the buoyancy remains positive (Dinniman & Timmermann 2016). To accurately describe the sub-ice-shelf processes, both the dynamics of the ocean circulation and the thermodynamics of the ice-ocean interactions have to be taken into account.

1.3.1 Thermodynamics

In an ice-water mixture, all the phase changes do generally take place at the thermodynamic equilibrium temperature, the freezing point. The melting or freezing processes are described by three fundamental equations: the seawater state equation, the heat and salt balance equations (Hellmer & Olbers. 1989, Holland & Jenkins 1999).
A linearized version of the seawater state equation for the freezing point is usually considered (Millero & Shin. 1978), to express the relationship between temperature T_b and salinity S_b at the ice–ocean interface,

$$T_b = a_0 S_b + b_0 + c_0 z_b \tag{1.35}$$

where a_0, b_0, c_0 values are reported in table A.1 while z_b is the considered ocean depth. At the ice–ocean interface, the balance between the sources/sinks of latent heat (melting/refreezing) and the heat fluxes from ice and water, is described by an heat exchange equation:

$$Q_I^T - Q_W^T = Q_{latent}^T = -\rho \dot{m} L_f \tag{1.36}$$

with

$$Q_W^T = -\rho_W C_{pW} \gamma_T (T_b - TW) \tag{1.37}$$

Here Q_I^T and Q_W^T are the ice and water heat fluxes, ρ the ice density, ρ_W the water density, $\dot{m}$ the rate of melting (positive) or freezing (negative), L_f the fusion latent heat for ice, C_{pW} the seawater specific heat capacity, and γ_T the thermal exchange velocity. T_B and T_W are the freezing point temperature (thus the temperature at the boundary) and the ambient water temperature.
Similarly to equation 1.36, an analogous balance equation can be written for salinity with the salinity fluxes due to ice freezing or melting in equilibrium with salt fluxes from the water.

$$Q_I^S - Q_W^S = \rho \dot{m} (S_I - S_b) \tag{1.38}$$

with

$$Q_W^S = \rho_W \gamma_S (S_b - S_W) \tag{1.39}$$

Here Q_W^S is the water salt flux, S_I the ice salinity, S_b the salinity at the boundary, S_W the salinity of the ambient water and γ_S the salt exchange velocity. In the equation 1.38, the term Q_I^S for the diffusive flux of salt into the ice shelf is set to zero (Holland & Jenkins 1999). The same for S_I, set to zero as well because the marine ice that forms at the ice shelf base due to basal freezing of seawater (with brine trapped in it), has been measured to have very low salt concentration (Dinniman & Timmermann 2016).
In both equation 1.37 and equation 1.39, an exchange velocity term is present (γ_T, γ_S). The choice of appropriate thermal and salt exchange velocities is the key to realistically diagnose melt rates (Holland & Jenkins 1999). The thermal and salinity exchange velocities represent the transfer of heat and salt through the oceanic boundary layer. In general, they can be assumed of the same order of magnitude only in the fully turbulent part of the boundary layer, while the turbulent diffusivity is generally almost suppressed close to the ice–ocean interface (Holland & Jenkins 1999). Where the suppression is great enough for molecular diffusion to become the dominant transfer mechanism, heat will diffuse more rapidly than salt. So, in general, γ_S has a smaller value than γ_T. The most

used parameterization of the salt and heat exchange velocities are the ones proposed by Kader & Yaglom 1972, that assumed the ice-ocean interface to be hydraulically smooth.

$$\gamma_T = \frac{C_d^{\frac{1}{2}} U}{2.12ln(C_d^{\frac{1}{2}} Re) + 12.5Pr^{\frac{2}{3}} - 9} \tag{1.40}$$

$$\gamma_S = \frac{C_d^{\frac{1}{2}} U}{2.12ln(C_d^{\frac{1}{2}} Re) + 12.5Sc^{\frac{2}{3}} - 9} \tag{1.41}$$

Where C_d is the quadratic drag coefficient with the associated ocean velocity U, Pr the Prandtl number, Sc the Schmidt number, and Re the Reynolds number defined as:

$$Re = \frac{UD}{\nu} \tag{1.42}$$

where ν is the kinematic viscosity and D the thickness of the fluid layer considered.
The fundamental quantity connecting the ice and the ocean is the basal melt rate $\dot{m}$. From an ice-shelf perspective, it contributes to the continuity equation 1.33 and is thus able to affect the ice-shelf evolution ($\dot{m}$ enters in the s_b term in the continuity equation). On the ocean side, the melted ice is responsible not only for sea level rise but, more importantly, for being the ultimate driver of the sub-ice-shelf circulation (see subsection 1.3.2). The dependence on temperature of the ocean basal melt rate $\dot{m}$ has been proven, by means of numerical experiments, to be quadratic because of the fact that, together with a direct dependence on temperature, an additional linear temperature dependence is present in the exchange velocity γ_T (Holland et al. 2008).

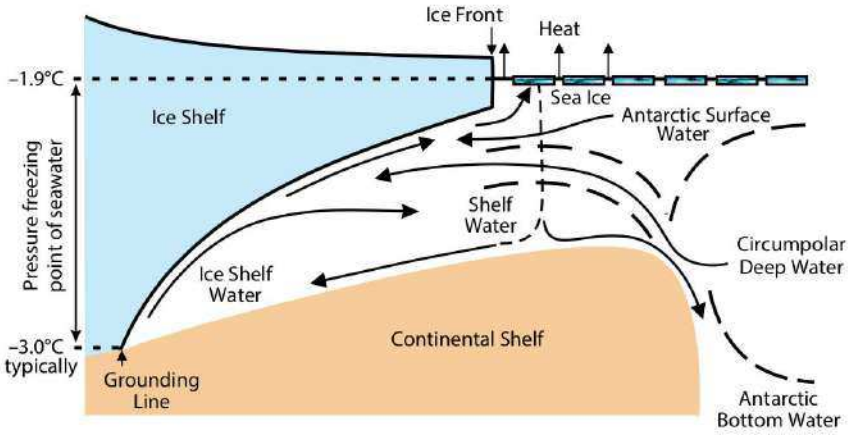

Figure 1.8: *Schematic showing circulation over the Antarctic continental shelf and how it relates to the different ice shelf basal melting modes (see 1.3.3). Sea ice formation generates cold (-1.9° C) and salty High Salinity Shelf Water that, being the densest water mass on the shelf, can advect to the deepest parts of the ice shelf cavity where it causes melting due to the pressure dependence of the freezing point (Mode 1). Warm (∼1° C) Circumpolar Deep Water advects onto the continental shelf and into the ice shelf cavities, leading to very high melt rates(Mode 2). Antarctic Surface Water is often cold, but it can be warmed in the summer, leading to strong seasonality in the melt rate near the ice shelf front (Mode 3). These three modes are the product of vertical and horizontal motions inside the sub-ice-shelf cavity. Thus a realistic model of the sub-ice-shelf ocean dynamics should include all the three spatial dimensions. From (Dinniman et al., 2016)*

1.3.2 Dynamics

To fully describe the dynamics in the ice-shelf cavity, the Newton's second law of motion, modified for a rotating reference frame, can be considered:

$$\rho_w \frac{D\bar{U}}{Dt} + \rho 2\bar{\Omega} \times \bar{U} = \nabla \cdot \tau - \rho g \bar{k} \tag{1.43}$$

with $\bar{\Omega}$ the Earth rotation rate and τ the Cauchy stress tensor expressed as

$$\tau_{ij} = -p\delta_{ij} + \rho\nu(\frac{\partial u_i}{\partial x_j} + \frac{\partial u_j}{\partial x_i}) \tag{1.44}$$

To better understand the fundamental forces that drive the ocean dynamics in the sub-shelf cavity, equation 1.43 can be split in a horizontal and vertical component and then dimensionally scaled. The horizontal component can be written as

$$\frac{U^2}{L} + \Omega U = -\frac{1}{\rho}\nabla_h p + \nu\frac{U}{L^2} + \nu\frac{U}{H^2} \tag{1.45}$$

In a sub-ice-shelf cavity the typical spatial dimensions are length $L \sim 10^5 m$, depth $H \sim 10^2 m$, horizontal velocity $U \sim 10^{-1} m s^{-1}$, rotation $\Omega \sim 10^{-4} s^{-1}$ and time $\sim \frac{L}{U}$; thus equation 1.45 takes the following form

$$\cancel{10^{-7}} + 10^{-5} = -\frac{1}{\rho}\nabla_h P + \cancel{\nu 10^{-11}} + \cancel{\nu 10^{-5}} \tag{1.46}$$

Although turbulent viscosity is high, the magnitude of the viscous term is small ($\nu \sim 10^{-6} m^2 s^{-1}$) and thus molecular viscosity forces are negligible together with the acceleration term.
In these aforementioned simplifications, the Coriolis term balances the pressure gradient. However both the viscous and the acceleration terms can become important where the velocity is high or the relevant length scale is small.
For motion beneath ice shelves, the vertical component of equation 1.43 is

$$\frac{U^2 H}{L^2} + \Omega U = -\frac{1}{\rho}\frac{\partial P}{\partial z} + \nu\frac{UH}{L^3} + \nu\frac{U}{HL} \tag{1.47}$$

Its dimensional scaled version is

$$\cancel{10^{-10}} + \cancel{10^{-5}} = -\frac{1}{\rho}\frac{\partial P}{\partial z} + \cancel{\nu 10^{-14}} + \cancel{\nu 10^{-8}} \tag{1.48}$$

Thus to a first approximation, the vertical pressure gradient is mainly balanced by gravity, allowing ocean pressure to be diagnosed directly from the density distribution.

$$\frac{\partial p}{\partial z} = -\rho g \tag{1.49}$$

Following this approximation, the circulation below a shelf is governed by a balance between the pressure gradient force and the Coriolis acceleration (geostrophic balance):

$$2\Omega_z v = \frac{1}{\rho}\frac{\partial p}{\partial x} \tag{1.50}$$

$$-2\Omega_z u = \frac{1}{\rho}\frac{\partial p}{\partial y} \tag{1.51}$$

Hence, ocean water in the cavity flows perpendicular to the pressure gradient and, although an homogeneous fluid is generally vertically rigid, vertical shear is also possible due to the eventual presence of an horizontal density gradient. This becomes clear differentiating equations 1.51 in the vertical direction:

$$f\frac{\partial v}{\partial z} = \frac{1}{\rho}\frac{\partial}{\partial z}(\frac{\partial p}{\partial x}) = \frac{1}{\rho}\frac{\partial}{\partial x}(\frac{\partial p}{\partial z}) = -\frac{g}{\rho}\frac{\partial \rho}{\partial x} \tag{1.52}$$

The above horizontal density gradient is generated, together with pressure gradients, by phase changes that are able to influence the density of the water near the sloping ice shelf draft. Horizontal density gradients represent the real direct forcing on and the ultimate driver for the large-scale circulation beneath an ice shelf.
Below an ice shelf there is a generally large surface slope, typically balanced by the pressure gradient imposed by ice. However, due to ice-ocean thermodynamics processes, phase changes can influence the density of the water near the ice shelf base and tilt the isopycnals allowing water to move.

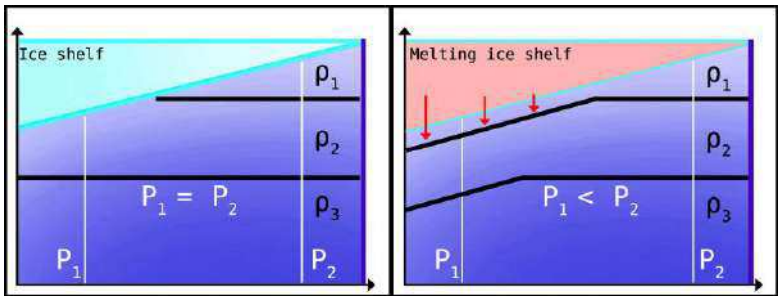

Figure 1.9: *The effects of phase changes on isopycnals (ρ is water density and P is pressure). On the left hand side the isopycnals are horizontal and no water motion is allowed. On the right hand side, thanks to ice melting, the isopycnals tilt, allowing water to flow.*

Furthermore, where friction dominates, drag is able to reduce the perpendicular-to-pressure-gradient velocity disrupting the geostrophic balance between the Coriolis term and the pressure gradient force. As a consequence the flow in the frictional Ekman layer acquires a component down the pressure gradient causing a net inflow transport perpendicular to the geostrophic flow and proportional to the geostrophic velocity and to the layer thickness.
The resulting cavity circulation is a sheared flow, predominantly in geostrophic balance, with friction becoming important near the ice shelf draft and seabed.The circulation enhances turbulent mixing, entraining heat up to the ice shelf draft and sustaining the circulation.

1.3.3 Melting modes

Sampling the ocean properties in proximity or below ice shelves is not an easy task. Together with the logistic cost of an observational campaign in Antarctica, the environmental conditions make the field work logistically challenging. Observational records are still sparse, but thanks to last years effort, an increasing number of data have been collected and put together via direct or indirect methods. The most up-to-date datasets for ocean basal melting in Antarctica are the ones by Rignot et al. 2013 and Depoorter

et al. 2013.

Figure 1.10 shows the basal melt rates and their wide variety in magnitude and spatial distribution. Several factors act in determining the melt rate distribution: the effects of the ocean and atmospheric circulation on the water masses close and below the shelf, the geometrical features of the ice-shelf base and both the depth and the distance of the grounding line from the continental shelf break (Holland et al. 2008, Jacobs 1992, Dinniman & Timmermann 2016).

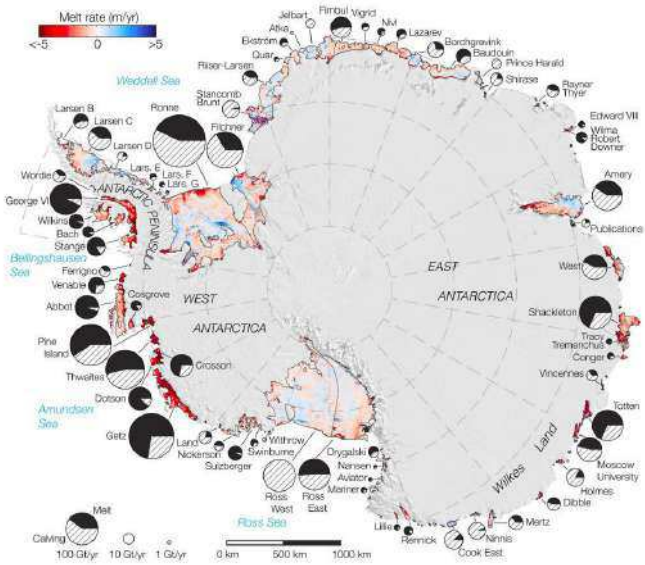

Figure 1.10: *Ocean basal melting rates inferred from observed changes in ice elevation and ice flow divergence. The contribution, in Gt/yr from calving and basal melting is reported. From Rignot et al. 2013*

Ocean basal melting is summarized in three melting modes by Jacobs 1992 (table 1.1):

- Mode 1: ocean melting is due to the cold, saline and dense Shelf Water (HSSW) formed on the Antarctic continental shelves, as a result of brine rejection during sea ice formation.
- Mode 2: ocean melting is due to the intrusions of warm and salty Circumpolar Deep Water (CDW) characterised by a high melting potential (CDW can be 4°C warmer than the local freezing point).
- Mode 3: ocean melting is due to the Antarctic Surface Water (AASW), characterized by a cold core of winter Water and a fresher and warmer upper layer.

.

Melting mode	Avg melt rates	Water mass	Area
Mode 1	$\sim 0.1\ m/yr$	cold and salty HSSW	Weddel and Ross Sea
Mode 2	1 - 10 m/yr	warm and salty CDW	West Antarctic Seas
Mode 3	0.1 - 1 m/yr	cold and fresh AASW	East Antarctic Seas

Table 1.1: *Melting modes features and associated Antarctic sectors*

METHODS

In this chapter are presented the ice-sheet models used in the thesis and the numerical ice-flow approximations on which they rely. Moreover is given an overview of the implemented ocean basal melting formulations.Special attention is given to the 1D coupled plume model by Jenkins (Jenkins 1991) developed and coupled to the two ice-sheet models during the Ph.D. Both for the modeling approximations and for the ice sheet models the treatment is essential and almost limited to what is of any importance to this thesis, more details on ice-flow approximations and ice-sheet models can be found in the related and cited literature.

2.1 Ice Sheet Models

Ice-sheet models are numerical tools that solve equations representing the physical processes driving the evolution of an ice sheet. There is a great variety of ice-sheet models of different physical complexities. The differences result from how many stress components are taken into account into the solution of the ice dynamics equations. Solving the *full Stokes equations* gives the most complete and close to reality representation of a real ice flow but, on the other hand, a full-Stokes-ice-sheet model is higly computationally demanding, which reduce the type of numerical experiments that can actually be performed with the current computational resources and capabilities. To overcome the computational cost issue, a hierarchy of models solving the approximated full Stokes equations have been developed (Kirchner et al. 2011).

2.1.1 Main modelling approximations

Hydrostatic approximation The most common used approximation in ice-sheet modeling is the hydrostatic approximation (or hydrostatic assumption) (Greve & Blatter 2009). The vertical normal stresses are simply assumed to be fully balanced by the hydrostatic pressure

$$\tau_{xx} = -p \tag{2.1}$$
$$\tau_{yy} = -p \tag{2.2}$$
$$\tau_{zz} = -p \tag{2.3}$$

Moreover, the shear stresses in equation (1.8) τ_{zx} and τ_{zy}, because of their relative importance in comparison to τ_{zz}, are neglected. Considering 2.3, the vertical balance of momentum of equation 1.8 becomes:

$$\frac{\partial \tau_{zz}}{\partial z} = \rho g \tag{2.4}$$

After vertical integration over an ice column, the hydrostatic pressure equation is given by:

$$p = \rho g \left(h - b\right) , \tag{2.5}$$

Shallow Ice approximation The Shallow Ice Approximation (SIA, Hutter 1983) assumes that the ice flow regime is basically driven by shear stresses along the horizontal plane and by basal friction at the base. Neglecting all the stresses except τ_{xz} and τ_{yz} and using the hydrostatic approximation, the full Stokes equations become:

$$\frac{\partial}{\partial z}\left(\eta\frac{\partial u}{\partial z}\right) - \frac{\partial p}{\partial x} = 0 \tag{2.6}$$

$$\frac{\partial}{\partial z}\left(\eta\frac{\partial v}{\partial z}\right) - \frac{\partial p}{\partial y} = 0 \tag{2.7}$$

$$-\frac{\partial p}{\partial z} = \rho g \tag{2.8}$$

Then, vertically integrating over the ice column and using the Glen's flow law (1.9), is possible to write an expression for the SIA horizontal velocity U

$$\mathcal{U} = -(\rho g)^n(\nabla s \cdot \nabla s)^{\frac{n-1}{2}}\nabla s E_f \int_B^s A(T')(s-z)^n dz + u_b \tag{2.9}$$

Because of the approximations, the SIA should be applied to a grounded slow-flowing ice mass only, characterised by an horizontal length much larger than its thickness. Roughly speaking the ice flow is the result of ice deformation below its own weight with basal shear stresses completely balanced by the gravitational driving stress. Because of friction at the ice-bedrock interface, a high vertical shearing at the ice bottom develops, with almost no vertical shearing near the surface (Paterson 1994, Greve & Blatter 2009, Douglas Benn 2010).

Shallow Shelf approximation The Shallow Shelf Approximation (SSA, MacAyeal 1989) assumes that the ice flow regime is mainly due to longitudinal stresses.This so-called plug flow is characterized by depth-independent horizontal velocities(Greve & Blatter 2009)

$$\frac{\partial u}{\partial z} = 0 \tag{2.10}$$

$$\frac{\partial v}{\partial z} = 0 \tag{2.11}$$

As a consequence, the full Stokes equations become:

$$\frac{\partial}{\partial x}\left(2\eta\frac{\partial u}{\partial x}\right) + \frac{\partial}{\partial y}\left(\eta\frac{\partial u}{\partial y} + \eta\frac{\partial v}{\partial x}\right) - \frac{\partial p}{\partial x} = 0 \tag{2.12}$$

$$\frac{\partial}{\partial x}\left(\eta\frac{\partial u}{\partial y} + \eta\frac{\partial v}{\partial x}\right) + \frac{\partial}{\partial y}\left(2\eta\frac{\partial v}{\partial y}\right) - \frac{\partial p}{\partial y} = 0 \tag{2.13}$$

$$\frac{\partial}{\partial z}\left(2\eta\frac{\partial w}{\partial z}\right) - \frac{\partial p}{\partial z} = \rho g \tag{2.14}$$

Using the hydrostatic assumption and after a vertical integration, the above equations are manipulated to obtain the following set of elliptic differential equations for the vertically averaged horizontal components of ice velocity $\overline{u}$ and $\overline{v}$.

$$\frac{\partial}{\partial x}\left[2h\overline{\eta}\left(2\frac{\partial \overline{u}}{\partial x} + \frac{\partial \overline{v}}{\partial x}\right)\right] + \frac{\partial}{\partial y}\left[2h\overline{\eta}\left(2\frac{\partial \overline{u}}{\partial y} + \frac{\partial \overline{v}}{\partial x}\right)\right] - \tau_{bx} = \rho g h\frac{\partial s}{\partial x} \tag{2.15}$$

$$\frac{\partial}{\partial y}\left[2h\overline{\eta}\left(2\frac{\partial \overline{v}}{\partial y} + \frac{\partial \overline{u}}{\partial x}\right)\right] + \frac{\partial}{\partial x}\left[2h\overline{\eta}\left(2\frac{\partial \overline{v}}{\partial x} + \frac{\partial \overline{u}}{\partial y}\right)\right] - \tau_{bx} = \rho g h\frac{\partial s}{\partial y} \tag{2.16}$$

where $\bar{\eta}$ is the ice viscosity averaged over the ice thickness and $\tau_{bx}\,/\,\tau_{by}$ represents the drag over the bedrock in the x and y directions, respectively. The SSA can be applied to a grounded fast-flowing ice mass (e.g. an ice stream) or to an ice shelf (setting the friction term τ_b to zero). As in the SIA, the horizontal length scale has to be much larger than the ice thickness (Paterson 1994, Greve & Blatter 2009, Douglas Benn 2010).

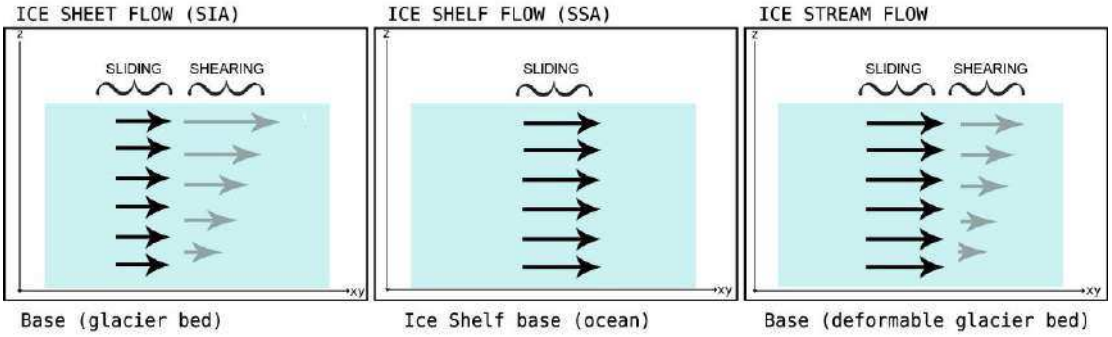

Figure 2.1: *The vertical profile of velocity in the ice for different approximations (black is sliding, gray is shearing). The velocity profile in the SIA (ice sheet flow), results from sliding at the base and shearing due to internal deformation. In the SSA (ice shelf flow) the velocity is vertically uniform, as the longitudinal stresses dominate. In the last panel the velocity profile of an ice stream flow is characterized by a significative contribution from both sliding and gliding, resembling a combined sheet and shelf flow profile.*

2.1.2 GRISLI Ice Sheet Model

The GRenoble Ice Sheet and Land Ice model (GRISLI), is an hybrid 3D-thermo-mechanical model capable of simulating both floating and grounded ice. It is written in finite differences using FORTRAN and has been developed at the LGGE in Grenoble (Ritz et al. 2001). GRISLI has been validated and used over Antarctica (Ritz et al. 2001, Ritz 2015) and successfully applied to study the evolution of ice sheets during the last two glacial cycles period (Peyaud et al. 2007; Alvarez-Solas et al. 2010, Colleoni et al. 2014, Colleoni et al. 2016) and to model the past and future Greenland ice sheet evolution (Peano et al. 2016). In the following paragraph an essential description of GRISLI is given, more details about the model can be found in Ritz et al. 2001 and Colleoni et al. 2014.

GRISLI Ice flow regions Depending on the ice flow regime, GRISLI applies different numerical approximations and treatments. Three main regions of ice flow are identified by GRISLI at each time step:

- Slow flowing grounded ice-sheet interior region: based on whether or not the ice is grounded. Then the ice-flow is solved using the SIA.
- Ice streams region: After checking that the ice is grounded, GRISLI evaluates the domain looking for:
  - narrow valleys
  - thick water-saturated sediment layers with low effective basal pressure (at least 150 m thick, with hydraulic head exceeding 250 m and effective pressure N lower than $3.5 \cdot 10^7$ Pascal)

  - ice thickness h and surface slope ∇s sufficiently low to satisfy $\rho g h \nabla s \leq 7 \cdot 10^6$ Pascal.

  If at least one of this three criteria are met then the ice flow in the region is computed by the SSA (Colleoni et al. 2014).

- Ice shelves region: is identified by GRISLI through a floatation criteria.

$$\rho H = \rho_w \left(sl - b \right) , \tag{2.17}$$

  where ρ_w is the ocean water density and sl stands for the sea level. The numerics for ice shelves is the same applied to ice streams (SSA) with the difference that basal drag is set to zero because no more friction at the ice base shelf base.

The above mentioned three regions are patched together at every time step. After the determination of the ice thickness solving equation 1.5, at each grid node of the computational domain the flotation criteria is applied.

Ice temperature GRISLI is a thermo-mechanical ice-sheet model and this means that ice temperature and velocities are coupled and solved consistently thanks to the alternately solution of the rheological Glen law 1.9 and of the energy equation 1.3 (Ritz et al. 2001). As explained in section 1.2.1, to solve equation 1.20, two boundary conditions are needed: one at the surface and one at the base of the ice sheet. GRISLI needs air temperature at surface and geothermal heat flux at the base. The energy conservation equation 1.20 is solved in the entire ice sheet domain and takes into account both vertical and horizontal advection as well as vertical diffusion of heat (Ritz et al. 2001).
A crucial quantity for the evolution of an ice sheet is the ice basal temperature T_b. In fact, depending on the temperature at the ice sheet base, basal sliding will occur or not. Therefore ice sheet mass balance and thermal evolution are strictly dependent on the basal temperature.
For T_b lower than the pressure-melting point (T_{mp}), the geothermal heat flux will simply be transferred into the ice column without causing any melting. For T_b at the pressure-melting point, the basal melt rate will be a function of the heat fluxes through the ice-bedrock interface and of the frictional heat produced by basal sliding. Finally for T_b exceeding T_{mp}, melting at the base will be driven by the heat in excess and T_b is reset is reset to the pressure-melting point ($T_b = T_{\mathrm{mp}}$), Colleoni et al. 2014.

Basal processes As explained above, basal sliding is allowed only if T_b is higher than or equal to the pressure-melting point T_{mp}. On the contrary, for temperature at the base lower than the pressure melting point no sliding occurs. Basal sliding is described through a Weertman law (1.24). Basal drag resisting the ice flow has the form of equations 1.26, 1.27, 1.28 for ice interior, ice streams and ice shelves respectively.

Climate forcing GRISLI requires two climate forcing: the monthly surface temperature and the total precipitation. The climate forcing is required at each time step and both the temperature and the precipitation are adjusted for changes in ice sheet elevation. The air surface temperature is corrected by means of an uniform atmospheric lapse

rate while changes in precipitation are related to changes in temperature corrections following the assumption that the saturation pressure of water vapor depends exponentially on temperature (Charbit et al. 2002).

Mass Balance In GRISLI the total mass balance is determined solving equation 1.5 and is a function of the climate forcing at surface, of the geothermal heat flux at the ice-bedrock interface and of the ocean basal melting at the ice-shelves ocean interface. At the ice sheet surface, the surface mass balance is given by the difference between accumulation and melting. Accumulation corresponds to the solid fraction of total precipitation (Marsiat 1994) while melting of snow and ice is parameterized using the Positive Degree Day semi-empirical method by Reeh (Reeh 1989). As described above the basal melting rate at the ice-bedrock interface for the ice-sheet interior and for ice streams depends on the basal ice temperature T_b and on the geothermal heat flux G_h, while under the ice shelves, the ice is melted by the heat fluxes coming from the ocean (more in 2.2, Colleoni et al. 2014).

Calving GRISLI has an ice-front-thickness-based calving law (Peyaud et al. 2007) applied only at the ice-shelves front. In GRISLI the ice-shelf front is identified looking for ice-shelf grid nodes adjacent to at least one ocean and zero-ice-thickness grid node. Once the ice-shelves front has been identified the calving scheme is applied. An ice-front grid node is characterized by a certain thickness $h_f(j)$ at the jth time step. If $h_f(j)$ is lower than a prescribed threshold $H_{calving}$ and/or if $s_m - b_m$ is negative, the ice-shelf front grid node is tested for calving (Colleoni et al. 2015). Starting from the upstream ice-shelf grid node with thickness h_{up}, and through a Lagrangian scheme, the ice thickness variation is computed, in the x direction, as follows

$$\frac{\partial h_{up}}{\partial t} = s_m - b_m - h_{up}\left(\frac{\partial u}{\partial x} + \frac{\partial v}{\partial y}\right) \tag{2.18}$$

The time in which ice flows from the upstream grid node to the ice front grid node is

$$t_f = \frac{\triangle x}{\triangle u} \tag{2.19}$$

while the ice front grid point thickness at the $(j+1)th$ time step has the following form

$$h_f(j+1) = h_{up} + t_f \cdot \frac{\partial h_{up}}{\partial t}\,. \tag{2.20}$$

Then if the $h_f(j+1)$ is lower than $H_{calving}$, calving occurs in the ice front shelf node. Viceversa calving does not occur and a new ice shelf grid node is created.

2.1.3 Úa ice flow model

Úa is an ice flow model developed at the British Antarctic Survey in Cambridge (Gudmundsson 2012).
It solves both the SSA and the SIA on an horizontally unstructured grid, using finite elements methods and is implemented in Matlab. Úa does not include thermodynamics and only the ice dynamics is taken into account, solving the vertically averaged form

of the horizontal stress balance and the evolutionary equation for the ice thickness 1.5. Úa has been used to calculate grounding-line migrations in various context (Durand 2009, Favier & Gudmundsson 2014) and has also succesfully participated to the Marine Ice Sheet Model Intercomparison Project (MISMIP) (Pattyn 2012). Úa identifies areas of grounded and floating ice using the flotation criteria 2.17 and, for each iteration, a floating/grounded mask is produced. In Úa the user can decide if using the SSA, the SIA or both (Hybrid mode as in GRISLI). The following model description is based on Gudmundsson, (2012), Favier et al., (2014) and on the available model documentation.

Inversion To overcome the absence of thermodynamics and thus the required link between climate conditions and ice flow, the ice viscosity and the slipperiness at the base are simultaneously obtained through a bayesian inversion approach(Gudmundsson & Raymond. 2008). A cost function, representative of the misfit between the observed and modelled surface velocities and the deviation from the priors and the retrieved fields, is minimised using a quasi-Newton method. The gradients of the cost function are calculated using the adjoint method. The results of the inversion procedure are the A coefficient for the Glen's law and the C_{sl} sliding coefficient at the base (Favier & Gudmundsson 2014).

Basal processes In Úa the basal friction term is always present in the set of the equations to be solved but is multiplied by $H(h - h_f)$,where H is the Heaviside step function and h_f the maximum possible ice thickness for floating ice according to equation 2.17. For an ice shelf $H(h - h_f)$ goes to zero, making the friction at the base dropping to zero. For grounded ice, the following Weertman-like friction law is applied:

$$\tau_b = C_{sl}^{-1/m}(\mid u_b \mid)^{1/m-1} u_b \tag{2.21}$$

where $u_b$is the basal sliding velocity, C_{sl} is the sliding coefficient, and m a stress exponent. The sliding coefficient C_{sl} can be manually set or prescribed after the inversion from surface velocities.

Climate forcing and mass balance Since Úa does not solve the energy conservation equation, there is no need to prescribe surface air temperature as in GRISLI. The only climate information that Úa needs to solve equation 1.5 are the distribution of surface mass balance and of melting at the ice sheet base. For both the surface and the base the user can directly prescribe a field of values, a uniform value or implement specific modules (as done in the present thesis for ocean basal melting, see section 2.2).

Meshing and elements deactivation In Úa the computational mesh domain is highly customizable depending on the needs of the user. The unstructured computational grid can be refined, increasing the elements resolution only where is needed.
Several remeshing criteria are available going from a thickness gradient criteria to a simple flotation criteria. All of the available criteria can also be used in combination, specifying the weight of each one in the refining procedure.
The flotation refinement criteria identifies the grounding line position using 2.17 and then refines the elements in a user-given range. The refinement area is defined through

the definition of a vertical flotation distance δ over which the refine has to be applied or, alternatively, by prescribing an horizontal distance from the grounding line and the desired elements size within this given horizontal distance.
The abovementioned meshing option can be applied to build the initial mesh computational domain but also to adapt the unstructured grid during runtime. Úa does not include a calving scheme and the closer option to simulate the calving process is the activation/deactivation of the mesh grid elements. Activation and deactivation of elements is based on the elements ice thickness, surface mass balance and on a combination of them.

2.1.4 GRISLI versus Úa: differences and key processes

The two main differences between Úa and GRISLI are:

- GRISLI is coded in finite differences while Úa in finite elements.
- GRISLI is a thermo-mechanical model while Úa solves just the ice flow dynamics, without any coupling to equation 1.3.

Finite elements vs finite differences The finite elements methods usually allows for the so-called "adaptive mesh refinement". Through adaptive mesh refinement, the resolution can be increased runtime and only where is needed. This is particularly useful for ice-sheet modelling mainly because key ice sheets processes demand very high spatial resolution, like ice streams and grounding lines, while large inner regions do not need such fine resolution. Another advantage of finite elements methods withrespect to finite differences method is that the numerical domain is typically made by a collection of irregularly shaped triangles, which is particularly favourable to deal with complex geometrical problems, as ice sheet modelling is (R.W. Lewis & Seetharamu. 2004, Cornford & Lipscomb 2013).
In a finite-difference model, like GRISLI, an increase in resolution has to be applied everywhere, because the grid is rectangular and regular. This clearly raise the computational cost of the numerical simulations, making some experiments unfeasible because too computationally demanding. Hence, the clear advantage of Úa is that, as explained in 2.1.3, the resolution can be increased exactly and only where requested (R.W. Lewis & Seetharamu. 2004).
This feature has been proven to be particular important in modeling marine ice sheets related-processes, since the resolution has to be as high as possible in the grounding line proximity (Gladstone 2010).
Both GRISLI and Úa determine the grounding line position using the flotation criteria 2.17 and when a migration is triggered the grounding line moves from one gridpoint/elements to another.
The neat advantage of Úa with respect to GRISLI in treating grounding line dynamics does not lie in flux corrections/buttressing parameterization at the grounding line (as for example Pollard & DeConto 2009 or Ritz 2015) but in a higher resolution at the grounding line.

Thermodynamics Thermodynamics has a major role in an ice-sheet model, linking climate conditions to ice flow velocities, as it is the case in nature.
As GRISLI is forced by the surface air temperature and the precipitation fields, the energy equation is solved, modifying viscosity coherently with the heat propagation. Instead Úa, as illustrated in 2.1.3, obtains the A coefficient for the rheological constitutive law trough the solution of an inverse problem based on observed surface velocities.
With respect to GRISLI the need for observed velocities represents a big limitation for Úa because it restricts its possible usages to only present-day. In fact, in analogy with weather forecasting, the results from Úa can be considered reliable if the length of the numerical experiment is lower or equal to the inertial thermodynamical memory of an ice sheet. This is because the initial state of the ice sheet is coming from observations and when the system, after a certain time span has evolved, those boundary conditions are not valid anymore. It is then clear that Úa cannot be used for paleoclimate applications or for long prediction runs in the future (more than a 50-100 yrs) (Arthern & Gudmundsson, 2010). On the other hand GRISLI has the advantage that, after a proper spin-up, as for atmospheric or oceanic models, there are no restrictions on the length of the simulations other than the computational cost (Colleoni et al., 2014, Ritz, 2015).

2.2 Ocean basal melting formulations

Given the role of ocean basal melting in determining the fate of Antarctic ice shelves, the importance of having a robust and reliable formulation able to capture the physics of the sub-ice shelf cavity in ice-sheet models is critical (Dinniman & Timmermann, 2016). The existing formulations for basal melting range from a simple depth criteria to more sophisticated dynamical models. The following section presents an overview of the ocean basal melting formulations used in the present work. Then, the 1D plume model developed for the purpose of this thesis is described in details.

2.2.1 Depth criterion

The less sophisticated formulation of ocean basal melting is based on a depth criterion (figure 2.2, Dumas, 2002). In this formulation ocean basal melt rates are not calculated but directly prescribed above and below an ad-hoc ocean depth z_m.
This formulation is easy to implement but many limitations arises: first, the absence of a feedbacks between the melt rates and the temperature and salinity of the surrounding ambient ocean. Second, the fact that the melt rates are constant in depth and more importantly the fact that the prescribed melt rates are based on observations of modern ocean conditions.
Therefore, even assuming that observations are satisfactory enough to reproduce realistic observed ocean basal melting, how to prescribe melt rates for past or future ice sheets simulations?

2.2.2 Helmer and Olbers (1989)

The Hellmer and Olbers (1989) parameterization is the most complete description of the ice-ocean interaction thermodynamics, also known as the "*three equations formulation*". This formulation takes into account both the thermal and salinity exchanges

with the surrounding ocean and depends on the state equation for seawater (equation 1.35). So, the full set of thermodynamics equations described in paragraph 1.3.1 is used to calculate the ocean basal melt rates.
The melt rate has the following expression:

$$\dot{m} = \frac{-\rho_W C_{pW} \gamma_T (T_b - T_W) + k_I \frac{dT}{dz}}{\rho L_I} \tag{2.22}$$

Where $\frac{dT}{dz}$ is the ice-shelf temperature gradient (usually neglected) and k_I the ice conductivity. Both the thermal and the salinity exchange velocities are used with fixed values ($\gamma_T = 0.0004 m/s$ and $\gamma_S = 5.05 \cdot 10^{-7} m/s$).

2.2.3 Martin et al. (2011)

This formulation neglects the salt exchange equations, considering only the heat exchange equation and the seawater state equation, therefore assuming infinite salt diffusivity. The choice of neglecting salt exchanges comes from the fact that, for a moderate thermal driving, the full set of thermodynamics equations can be approximated by an equivalent two-equation formulations because the non-linear dependence of melt rates to ocean temperature becomes apparent only at high thermal driving (Holland & Jenkins 1999, Holland et al. 2008). This parameterization has been designed by Martin et al. 2011 departing from the original work of Beckmann & Goosse 2003.

$$\dot{m} = \frac{-\rho_W C_{pW} \gamma_T F_{melt} (T_b - T_W)}{\rho L_I} \tag{2.23}$$

Here the F_{melt} tuning parameter was introduced, with a value of $5 \cdot 10^{-3}$, in order to match the present-day position of the grounding line in Antarctica (Martin et al. 2011). Both the thermal and the salinity exchange velocities are used with fixed values ($\gamma_T = 0.0004 m/s$ and $\gamma_S = 5.05 \cdot 10^{-7} m/s$), as in Helmer and Olbers (1989).

2.2.4 Pollard and DeConto (2012)

This formulation is based on Martin et al. (2011) with some discrepancies. They introduced a K_{shelf} parameter and a quadratic dependence on ocean temperature, following Holland et al. 2008, in contrast with the linear dependence of Martin et al. 2011. The K_{shelf} parameter takes a different value depending on the Antarctic sector to which the parameterization is applied. This is a way to account for the impacts of different ocean water masses, bathymetric features and ice-shelf geometrical properties on melt rates. The K_{shelf} parameter ranges between 1 and 8, as shown in table 2.1, while both the thermal and the salinity exchange velocities are used with fixed values as the F_{melt} tuning parameter, following from Helmer (1989) and Martin (2011) respectively ($\gamma_T = 0.0004 m/s$ and $\gamma_S = 5.05 \cdot 10^{-7} m/s$)

$$\dot{m} = \frac{-\rho_W C_{pW} \gamma_T K_{shelf} F_{melt} \mid T_b - T_W \mid (T_b - T_W)}{\rho L_I} \tag{2.24}$$

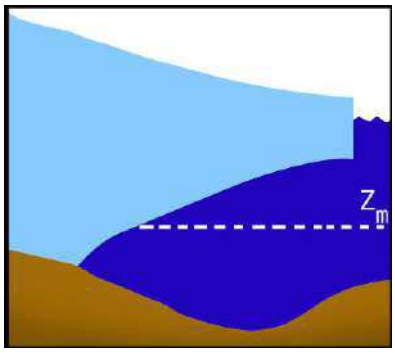

Figure 2.2: *In the depth criterion formulation, two values for basal melting are prescribed above and below* z_m

Area	K_{shelf}
Ross Sea	1
Weddel Sea	1
West Antarctic Seas	8
East Antarctic Seas	8

Table 2.1: K_{shelf} values from Pollard & DeConto 2012

2.2.5 1D plume model

The numerical implementation of this model has been specifically developed during the Ph.D. for the need of the study. The one-dimensional plume is a simplified sub-ice-shelf cavity ocean circulation model. Its physics is more complex than the parameterizations described previously but is nevertheless less sophisticated than in the case of a direct coupling with general or regional ocean circulation model. The conceptual idea behind the plume model is to keep the essential oceanic processes in act in the cavity and thus have a robust physical link between ocean conditions and basal melt rates. The first plume model of this type has been developed by Jenkins(1991).
The circulation below the ice shelf is summarized as a steady-state plume of Ice Shelf Water rising along the ice shelf draft. Generally speaking, a plume is a positively or negatively buoyant parcel of fluid rising or sinking in a denser or less dense ambient fluid (Turner 1989). The stationarity assumption comes from the consideration that the time needed for the ice shelf geometry to change enough to significantly impact the melt rates is higher than the time needed by the ocean current to reach a new equilibrium (Jenkins 1991, Smedsrud & Jenkins 2004).
More specifically the plume model is designed as a two-layers system (figure 2.3). A lower layer with ambient ocean water (T_W ,S_W) and an upper layer in contact with the ice shelf. This upper layer is made of well mixed Ice Shelf Water and is characterized by a thickness D, a bulk velocity U and a vertically-averaged temperature T and salinity S (Jenkins 1991). Because of the vertical averaging, the vertical dimension is neglected as well as the horizontal dimension, thus not considering the Coriolis effect. The upper layer is representative of the ISW plume. This plume rises up the ice-shelf draft, entraining the ambient water of the lower layer and thermodynamically interacting with the ice shelf. The plume thus interactively varies its own density, thickness, velocity, temperature and salinity.

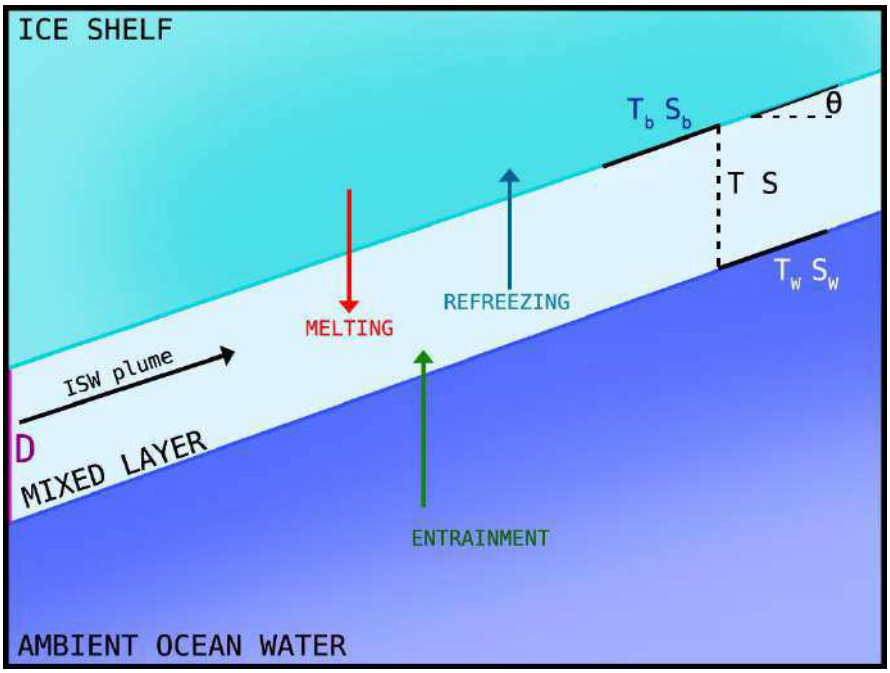

Figure 2.3: *Schematic representation of the 1D plume model. D is the plume layer thickness, θ the slope of the ice shelf base. T: plume temperature, S: plume salinity, T_w: lower layer temperature, S_w: lower layer salinity*

The plume prognostic variables D, T, S and U are function of the along ice-shelf flow dimension only and, although a curvilinear approach would be preferred, a simple cartesian frame of reference can used because of the sufficiently small slope and curvature of the ice shelf base (Jenkins 1991, Smedsrud & Jenkins 2004).
Four ordinary differential equations, obtained by neglecting the vertical and horizontal dimensions in equation 1.43, describe the conservation of mass, momentum, salt and heat of the plume:

$$\frac{d}{ds}(DU) = \dot{e} + \dot{m} \tag{2.25}$$

$$\frac{d}{ds}(DU^2) = -D\frac{\Delta\rho}{\rho_W} g sin\theta - C_d U^2 \tag{2.26}$$

$$\frac{d}{ds}(DUS) = S_W \dot{e} + S_b \dot{m} + (S_b - S)\gamma_S \tag{2.27}$$

$$\frac{d}{ds}(DUT) = T_W \dot{e} + T_b \dot{m} + (T_b - T)\gamma_T \tag{2.28}$$

where

$$\dot{e} = E_0 U sin\theta \tag{2.29}$$

is the rate of entrainment, θ the ice-shelf slope and C_d the drag coefficient.
The entrainment corresponds to the mixing of ambient water within a plume that is considered to be turbulent at a small distance from its source (Turner 1989). Expression 2.29 is based on parameterization of Pedersen (1980) where the suggested value of E_0 is 0.072 and is adimensional. In general, in order to compensate for the lack of the Coriolis deviation and the consequent fact that the plume would flow along shallower slopes, E_0 usually takes a value of 0.036 (MacAyeal 1985, Jenkins 1991). Here $\dot{e}$ is linearly

dependent on the bulk velocity of the plume and on the ice-shelf slope. The possibility for water to detrain from the plume to the ambient water environment is not considered. Only inflowing of ambient water through entrainment is allowed.
The continuity equation 2.25 considers melting and entrainment as mass sources while refreezing acts as a sink. In the momentum equation 2.26, the driving buoyancy term, function of the ice-shelf slope and of the density contrast between the ambient and Ice Shelf Water, is balanced by the ice-plume friction. A strong relationship comes out from both equation 2.25 and 2.26 between the plume thickness D and the bulk velocity U. As a result of friction and entrainment, a negative feedback on bulk velocity develops: as bulk velocity U rises, both drag and entrainment increase. A higher entrainment will strongly oppose to a velocity boost because of an increase in mass without a corresponding increase in momentum (MacAyeal 1985, Jenkins 1991). Thus an accelerating plume will become thinner, while a decrease in the plume bulk velocity will translate in a thickening of the plume.
Equations 2.27 and 2.28 express the salinity and the heat conservation respectively. In the heat conservation equation 2.28, freezing or melting at the interface move ambient water of temperature T_W out of or into the plume. In the salinity conservation equation 2.27, the ambient water of salinity S_W is entrained from below and some salt remains trapped in the ice. The salinity and temperature variations alter the plume density and consequently the plume buoyancy. The variation in density is taken into account through the following expression

$$\delta\rho = \rho_W \left[\beta(S - S_W) - \alpha(T - T_W)\right] \tag{2.30}$$

where β is the salt contraction coefficient and α a parameter expressing the thermal dependence of density.
Together with dynamics, the thermodynamic interactions between the ambient ocean and the ice shelf are taken into account as well. The salinity and thermal exchanges are calculated with equations 1.36 and 1.38. The main difference between the use of these three equations coupled with the dynamical plume model and the use of them in a stand-alone way as in 2.2.2 lies in the thermal and salinity exchange velocities. In the 1D plume model γ_T and γ_S do not have fixed values as in Helmer and Olbers (1989) but, instead, are computed interactively using the bulk velocity of the plume. Thus the strength of the plume model consists in a robust physical bond between ocean conditions and melt rate characterized by a non-linear temperature sensitivity and by an implicit dependence on ice-shelf geometrical features (Jenkins 1991, Holland & Jenkins 1999, Smedsrud & Jenkins 2004, Holland et al. 2008). The depth of the grounding line and the slope of the ice-shelf draft also influence the melting/freezing distribution. Depth determines the effective amount of sensible heat available to melt the ice while slope determines how quickly the plume rises up to the surface, which then influences the efficiency of turbulent transfer (via γ_T and γ_S).
In this thesis the 1D plume model has been coupled runtime to both GRISLI and Úa. In the Úa coupling, a runtime interpolation from the unstructured grid to a equally spaced grid on which the plume equations are actually solved, is performed at each time step. Once the plume equations are solved, the obtained melt rates distribution is interpolated back to the finite elements unstructured grid. The set of plume equations has been coded using an explicit finite differences Eulerian scheme and the online coupling has

been implemented as described in figure 2.4 and in the following paragraph (additional technical details on the implementation are explained in the following chapters when needed). At each grid node that belongs to the grounding line, a plume is allowed to develop and, consistently with its own buoyancy, to rise following a straight path toward the ice shelf front. Hence, from each grid point on the grounding line, there is a plume rising up along the ice shelf draft, thus forming a collection of plumes flowing below the ice shelf, side by side, and not interacting with each other (figure 2.4). To initialize the plume, the values for initial plume temperature (T_0), salinity (S_0), thickness (D_0) and starting bulk velocity (U_0) are prescribed by the user. In each grid cell, the plume is solved using as boundary conditions the final values of T, S, U and D from the previous grid cell (figure 2.4).

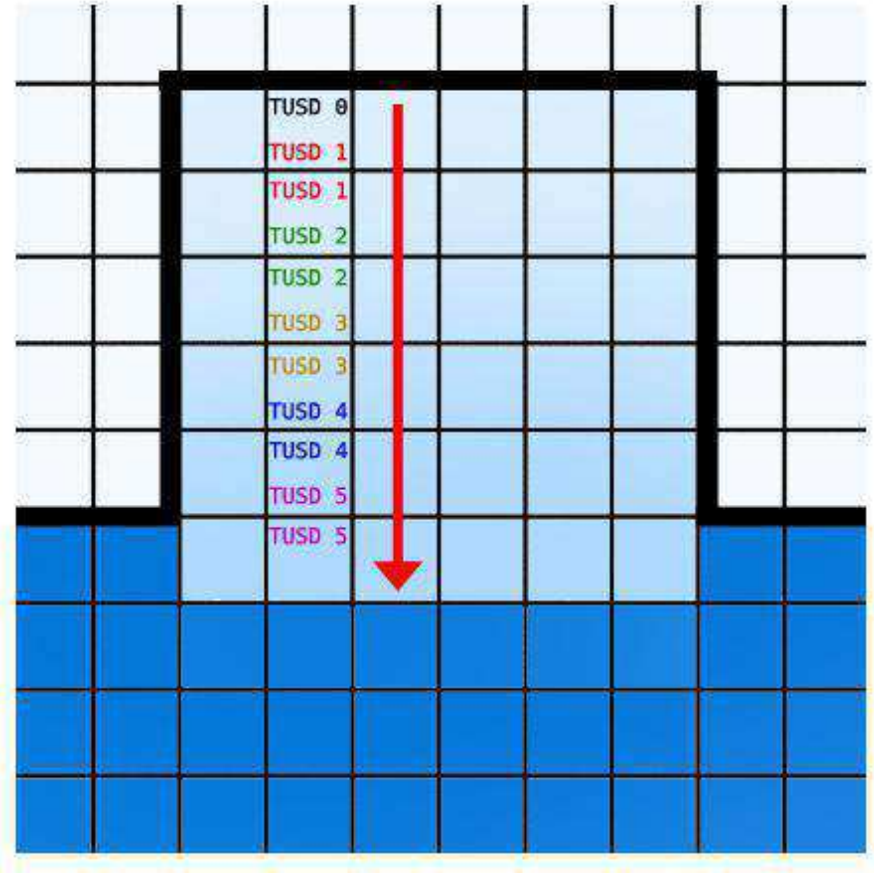

Figure 2.4: *A simplified representation of the plume numerical implementation. The black thick line represents the grounding line, marking the boundary between the grounded ice (white), the ice shelf (light blue) and the ocean (deep blue). The red arrow is indicative of the plume path, straight from the grounding line to the ice shelf front. At each grid cell in which the plume is solved corresponds two sets of prognostic variables T,S,U and D. The T,S,U,D are then passed to the next cell.*

Since the rise of the plume is mainly governed by buoyancy, and buoyancy is in turn linked to the evolving temperature and salinity of the plume during its path, a density-contrast-based condition is implemented in order to evaluate the plume buoyancy potential to rise through the entraining ambient water or if a detachment from the ice-shelf base occurs (using 2.30 the model checks when the plume becomes denser than ambient water). When/if the plume detaches, the melt rate is set to zero.

COMPETING PROCESSES IN GROUNDING LINE DYNAMICS

3.1 Introduction

As outlined in section 1.3, ocean basal melting and calving are the two most influential drivers for the evolution of an ice shelf. The first acts mostly and directly at the grounding line, while the latter is responsible for ice loss at the calving front thus influencing the buttressing that the ice shelf exerts on the grounded ice and the fluxes at the grounding line.
However, despite the importance of these processes, their implementation in ice-sheet models still lacks of robustness. This is especially true for the process of calving, for which the basic physics behind the icebergs formation remains unconstrained. The calving process is implemented by different means in ice-sheet models but there is no clear consensus about which formulation is the most robust and reliable. Furthermore numerous ice-sheet modelling studies have been conducted without investigating in depth which are the impacts of the numerical implementations and how calving compete with the other processes in determining grounding line migration. This issue is of particular interest for long term ice-sheet simulations, where the interaction between several processes acts and determines the magnitude of expansion of ice shelves.
Currently, future and paleo simulations of the AIS are usually performed by means of hybrid SSA-SIA ice-sheet models, at typical resolutions of 15 km to 40 km (Huybrechts and de Wolde, 1999; Pollard and DeConto, 2009; Greve et al., 2011; Martin et al., 2011; Ritz et al., 2015; Pollard and DeConto, 2016). Given the large number of ice shelves in the AIS and the role that they have in its dynamical evolution, higher spatial/temporal resolutions would be necessary to better resolve the grounding line migration. However, given the high computational cost of the long term spin-up procedure and the size of the AIS computational domain, the current numerical possibilities do not allow yet to systematically increase the resolution beyond 15 km.
In this chapter the competition between ocean melting and calving in driving grounding line migration is investigated using the hybrid SSA/SIA ice sheet model GRISLI (Ritz et al., 2001, section 2.1.2).

3.2 Experimental design and model setup

All the experiments presented in this chapter have been performed with GRISLI (Ritz et al., 2001, section 2.1.2) at 5 km of resolution.
The numerical experiments are performed in an idealized framework and are designed in order to isolate as much as possible the calving and ocean melting impacts:

- The computational domain is a regular cartesian grid of 40 x 160 grid nodes (200 km x 800 km) and consists in a narrow topographic channel of decreasing bathymetry, surrounded by a continental margin above sea level (figure 3.1). The channel is characterized by a bump, whose presence, provides two relevant bedrock condition: prograde and retrogade.

- The experiments are run on two idealized bedrocks morphology described by equation 3.1 (figure 3.1), taken from the design of the MISMIP+ experiment (Asay-Davis et al. 2016). Here the bedrock morphology is adapted to the experimental needs by increasing the horizontal dimension, extending the bedrocks margins in the cross channel direction from 80 to 200 km. The differences amongst the two bedrocks reside in the channel width (Bedrock B1 with half-width $w_c = 24$ km and bedrock B2 with half-width $w_c = 48$ km, (figure 3.1)).
  The equation describing the bedrock elevation in meter is

$$z_{Bedrock} = max(B(x) + B(y), -B_{max}) \tag{3.1}$$

  Where B_{max} is the maximum depth of the bedrock topography and $B(x)$ is equal to

$$B(x) = B_0 + B_2(\widetilde{x})^2 + B_4(\widetilde{x})^4 + B_6(\widetilde{x})^6, \tag{3.2}$$

  $B(y)$ equals to

$$B(y) = \frac{d_c}{1 + e^{-2(\frac{y - L_y/2 - w_c}{F_c})}} + \frac{d_c}{1 + e^{2(\frac{y - L_y/2 + w_c}{F_c})}} \tag{3.3}$$

  with

$$\widetilde{x} = \frac{x}{\overline{x}} \tag{3.4}$$

  Where L_x is the domain length (along ice flow), L_y is the domain width (across ice flow), B_0 is the bedrock topography (at x = 0), B_2 is the second bedrock topography coefficient, B_4 is the third bedrock topography coefficient, B_6 is the fourth bedrock topography coefficient, $\widetilde{x}$ is the characteristic along-flow length scale of the bedrock, f_c is the characteristic width of the side walls of the channel, d_c is the depth of the channel compared with the side walls and w_c is the half-width of the channel. The parameter values used in these equations are given in table 3.1.

Parameter	Value
L_x	800 km
L_y	200 km
B_0	-150.0 m
B_2	-728.8 m
B_4	343.91 m
B_6	-50.57 m
$\widetilde{x}$	300 km
f_c	4.0 km
d_c	500 m
w_c	24:48 km
B_{max}	720 m

Table 3.1: Parameters values in equations 3.1, 3.2 and 3.3. All the parameters have the same values used in the MISMIP+ design experiment, with the only exception of L_y. L_y has been increased from 80 km to 200 km.

- All the experiments are forced by a set of spatially fixed uniform temperature and surface mass balance fields, reported in table 3.2. The four selected mean climate

states can be considered representative of the range of values taken by temperature from a glacial/cold period to an interglacial/warm period (Petit et al., 1999). In this experiments the surface ablation is zero, thus the SMB is given by only accumulation of solid precipitation. The SMB value was chosen has representative of the average amount of precipitation on the Antarctic ice shelves (?).

- The geothermal heat flux at the base is set to a very low value (10^{-3} mW/m^2) to reduce the impact of the basal sliding component on the total ice flow. Thus, ice deformation represents the main driver for ice flow in all the experiments. Having a flow mainly deformation-driven allows to better evaluate the contribution of the air surface temperature to the ice flow. In fact, as illustrated in section 1.2.1, the ice deformation is tightly bounded to the air surface temperature through the heat diffusion equation and to the ice viscosity dependency on ice temperature. Figure 3.2 shows a comparison between the vertically averaged ice velocity and the sliding velocity at the ice base for one of the idealized simulations.

Climate forcing	T(°C)	spinup SMB(m/yr)
C1	-10	0.25
C2	-20	0.25
C3	-30	0.25
C4	-40	0.25

Table 3.2: Climate forcing used for the idealized experiments.

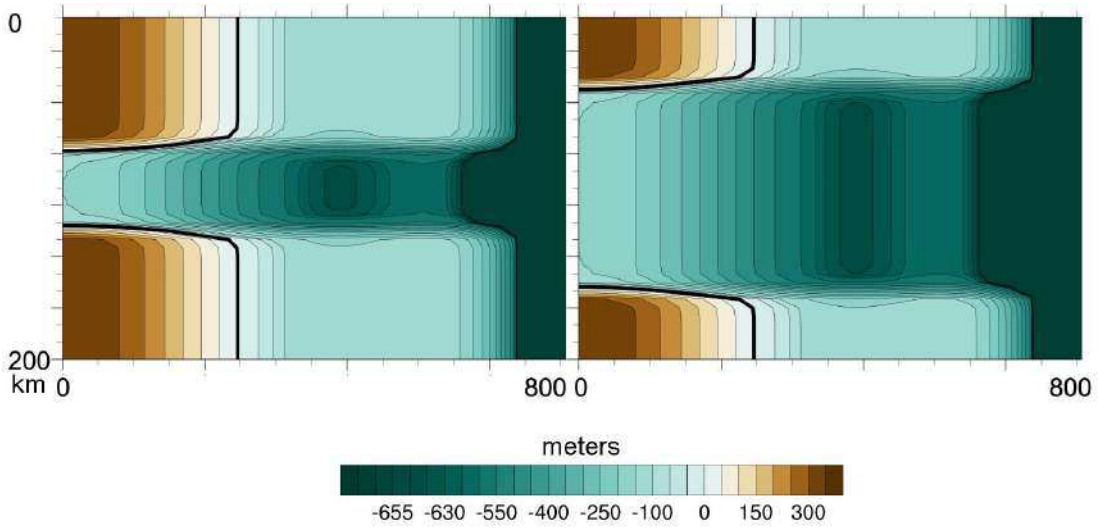

Figure 3.1: *The two idealized bedrocks used in the experiments seen from above. The black line indicates the boundary between the bedrock above and below sea level. The bedrock B1 is shown in the left panel, while the bedrock B2 is shown in the right panel. The difference between B1 and B2 resides in the channel width. Bedrock B1 has an half-width of w_c = 24 km, Bedrock B2 has an half-width w_c = 48 km.*

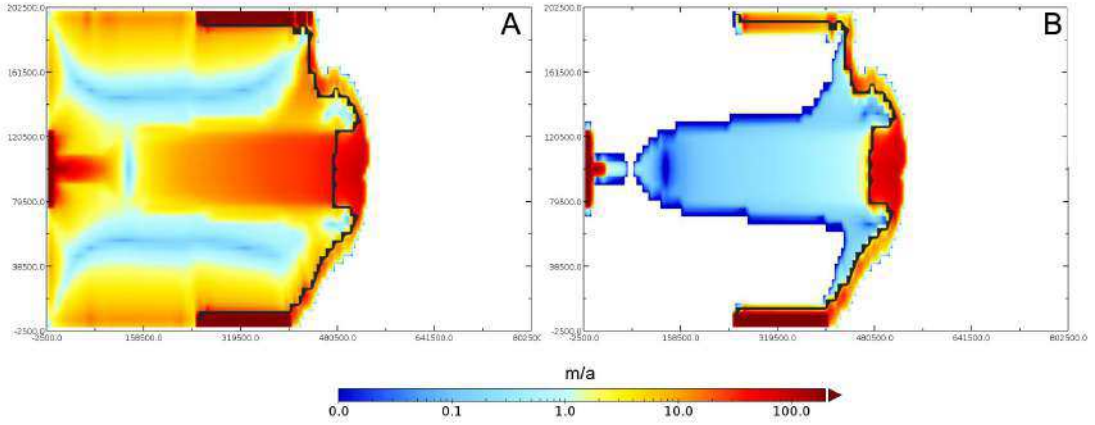

Figure 3.2: *Example of vertically averaged ice velocities (panel A) and basal sliding velocities (panel B) for one of the idealized experiments. The thick black line represents the grounding line.*

The numerical experiments are divided in two phases:

- Spin-up phase: the climate forcings described in table 3.2 are used to force an initial uniform ice layer of 100 m thickness, prescribed on the above sea-level bedrock. The run duration for this phase is 20000 yr. The objective of this phase is to obtain different ice shelves configuration on the two bedrocks. To do this, only the H_{coup} thickness threshold for calving is varied while any ocean basal melting under the ice shelves is inhibited.
- Sensitivity experiments: the climate forcings from table 3.2 are used to force a set of selected simulation from the previous spin-up phase. In those experiments, both the H_{coup} thickness threshold and ocean basal melting are varied. The runs duration in this phase is 1000 yr.

3.2.1 Spin-up phase

The objective of this phase is to obtain different ice shelves configurations on the idealized bedrocks B1 and B2 that are then used as the initial conditions for the sensitivity experiments (see next section 3.2.2). Each spin-up lasts for 20000 years. This duration was considered sufficient to reach a thermodynamical equilibrium with the applied forcings. From here on the B1,B2 bedrock notation will also identify the set of ice shelves that have in common the same bedrock.
A uniform ice layer of 100 m thick is prescribed on the emerged portion of the two bedrocks. Note that the initial ice distribution does not present any ice-shelves, as they grow during the experiments. The initial layer is forced succesively by the four climates C1,C2,C3 and C4 (table 3.2). Thus, for each bedrock, a set of four experiments differing in climatic forcing is obtained. Then, the calving thickness criterion H_{coup} is varied between 80 and 300 meters, while basal melting at the ice shelf base is set to zero for each of the four sets of experiments.
Depending on the climate forcing and on certain ranges of H_{coup}, ice shelves do not develop during the spin-up. In fact, for a given balance between ice velocities and calving magnitude, the upstream flow may not be able to sustain or feed the growth of an ice shelf. As explained in the methods (section 3.2), the ice velocity is largely connected

to climate forcing through the ice viscosity dependence on ice temperature. Ice flow velocities are thus expected to be higher under warmer climate conditions and viceversa under cold climate conditions.
In total, 80 simulations (20 different H_{coup} values varying between 80 m and 300 m x 4 Climates) have been run for each bedrock.

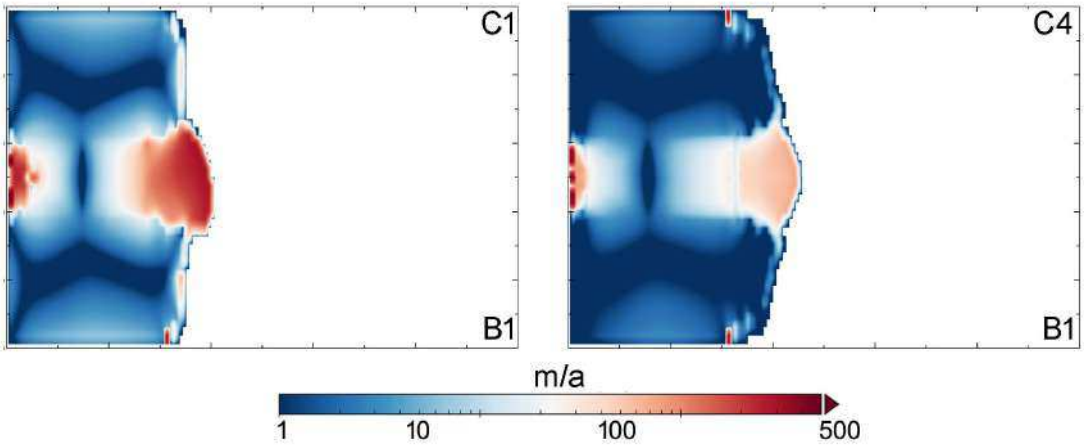

Figure 3.3: *Final ice velocities at the end of two sensitivity runs that differ only in the applied climate forcing. In the left panel is shown the ice shelf forced by C1 climate (warm, T_{air} = -10 °C) while in the right panel is shown the ice shelf forced by C4 climate (cold, T_{air} = -40 °C). The bedrock morphology is bedrock B1.*

The dependence of the final position of the grounding line on H_{coup} and climate forcing is shown in figure 3.4. The grounding line reaches final and stable position both on the prograde and retrograde portion of the bedrock.

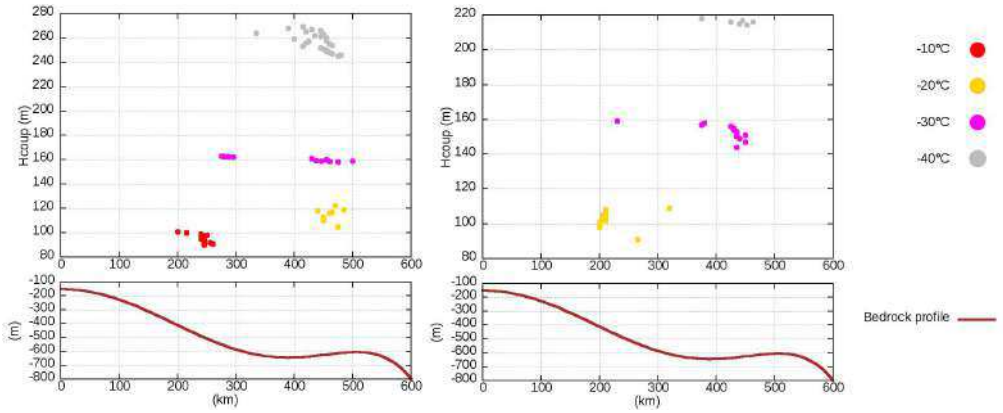

Figure 3.4: *Final spin-up grounding line positions of the vetical obtained ice shelves over bedrock B1 (left) and bedrock B2 (right). In the bottom left panels is displayed the bedrock profile over which the grounding lines are located. Each dot represents the final grounding line position of each ice shelf obtained during the spin-up phase. The final grounding line positions is calculated with respect to the distance from the left domain edge.*

After 20000 yr, all the ice shelves are in thermo-dynamical equilibrium with the applied forcings and result fully spun up.
At the end of the spin-up phase, for each bedrock, are selected the three ice shelves displayed in figure 3.5 that represent key state of dynamical equilibrium.

3.2.2 Sensitivity experiments

The objective of the sensitivity experiments is to investigate the interplay between calving and ocean basal melting on grounding line migration. The initial conditions for those experiments are selected from the spin-up phase (figure 3.5) and each melting run lasts for 1000 years.
Each selected spin-up ice-sheet ice-shelf configuration (table 3.3) is forced by the four climate forcings C1,C2,C3,C4 (table 3.2). Surface mass balance is set to zero in order to isolate as much as possible the contribution from calving and ocean basal melting.
The ocean basal melting is prescribed using a depth criterion (see section 2.2.1). The depth limit is set above the initial grounding line position of each of the three selected spin-up configuration (table 3.3). The values prescribed above (bmelt1) and below (bmelt2) this depth limit are reported in table 3.4. 72 combinations of ocean basal melting rates are obtained, by varying bmelt2 between 0.1 and 10 m/yr for each selected value of bmelt1. The ocean basal melting values are based on the present day observations from Rignot et al. (2013) and Depoorter et al. (2013). Those 72 ocean forcing combinations are divided in 8 groups (from A to H), (table 3.4). Setting the depth limit above the grounding line ensures that bmelt2 will impact the grounding line area while bmelt1 will influence the shallower part of the ice shelf base. In those simulations, the H_{coup} is set to 200 m. Then, the set of sensitivity experiments is repeated for H_{coup} = 100 m. A variation in the ice thickness criterion corresponds to a more or less effective calving. The two values for the H_{coup} thickness criterion are selected based on the observed ice-shelves front thickness (Colleoni et al. 2015).
The comparison between the two sets of simulations allows to investigate the competing effect between calving and ocean basal melting.
In total, of the 6 spin-up ice shelf configurations (table 3.3), 576 sensitivity experiments are performed as the result of the forcing by 4 different climates, 2 thickness criteria for calving and 72 combinations of ocean melting, leading to a complete set of 3456 sensitivity experiments.

Spin-up	Bedrock	Gline position(km)	Bmelt Depth limit(m)
B101	B1	260	500
B102	B1	335	550
B103	B1	480	550
B201	B2	260	500
B202	B2	330	550
B203	B2	470	550

Table 3.3: Initial conditions for the sensitivity experiments. Three spin up simulations are used as initial conditions phase. Initial grounding line position (Gline) on the bedrock; and ocean melting depth limit applied for melting under the ice shelves following equation REF.

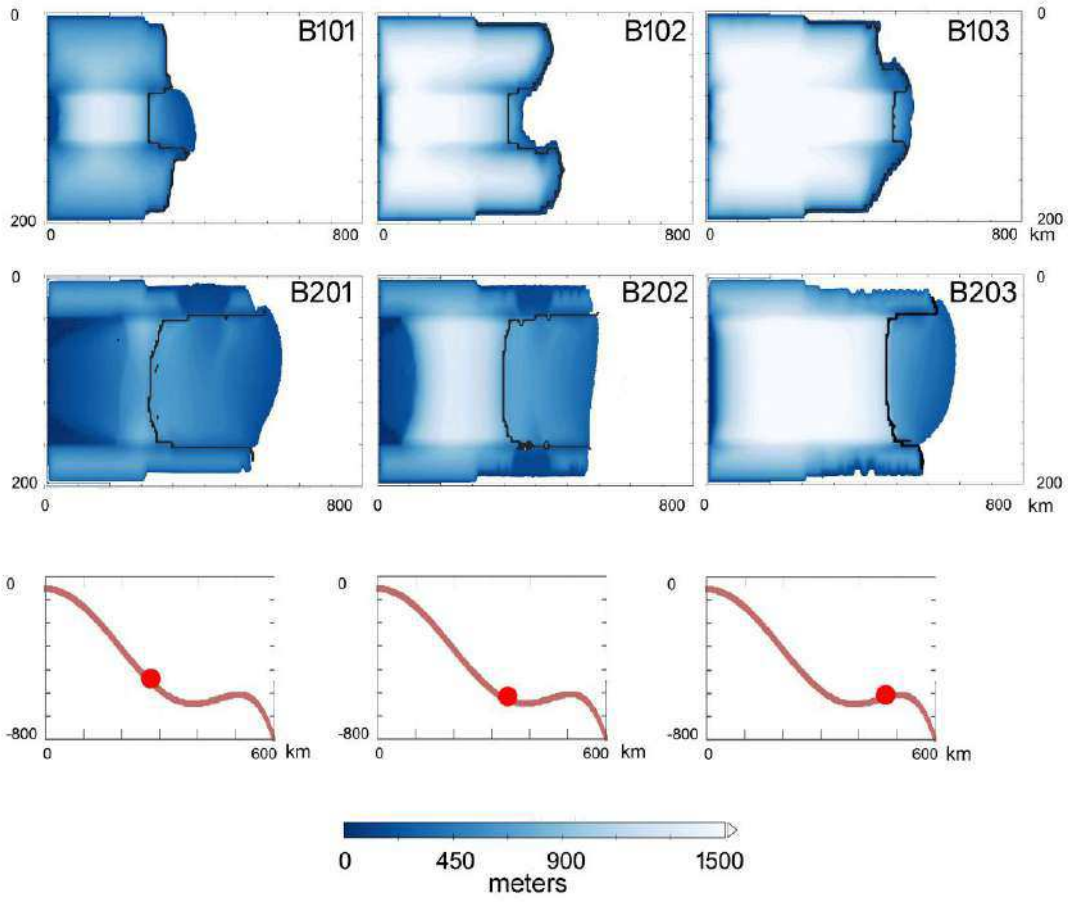

Figure 3.5: *Spin-up simulations used as initial conditions for the sensitivity experiments. In the the two top rows panels are shown the ice thickness of the six selected spin-up simulations for B1 bedrock (top row). B2 bedrock (second row). The bottom row displays the grounding line position of the six selected ice shelves.*

Ocean melting	**A**	**B**	**C**	**D**	**E**	**F**	**G**	**H**
Bmelt1(m/yr)	0.1	0.2	0.4	0.8	1	1.5	2	4
Bmelt2(m/yr)	0.1 : 10	0.1 : 10	0.1 : 10	0.1 : 10	0.1 : 10	0.1 : 10	0.1 : 10	0.1 : 10

Table 3.4: Ocean basal melting groups. Bmelt2 values ranges from 0.1 to 10 m/yr (with the sme increment of bmelt1) while bmelt1 is kept fixed within a group of experiments and increases from 0.1 to 4 m/yr from group A to group H.

3.3 Results

3.3.1 Ocean basal melting versus calving

In the following the variable of interest is the grounding line (GL) absolute and relative spatial migration. The relative migration is defined as the percentual change in position GL_{pc} reached at the end of an experiment (GL_{final}) compared with its initial position $GL_{initial}$:

$$GL_{pc} = \frac{(GL_{final} - GL_{initial}) * 100}{GL_{initial}} \tag{3.5}$$

The results are summarized in figures 3.6, 3.7, 3.8,3.9, 3.10 and 3.11. Figure 3.6 displays the percentual changes in grounding line position at the end of each sensitivity experiment for B101, B102 and B103.
The other figures (figure 3.7, 3.8, 3.9, 3.10 and 3.11) are considered to investigate the relative role of calving and ocean melting in driving the grounding line evolution. In these figures are displayed the final grounding line position values for each sensitivity experiment (final grounding line positions are indicated by the colored dots). Each dot is thus representative of the final grounding line position obtained by forcing the inital selected shelves (table 3.3) with one climate from table 3.2, one melt rates combination (table 3.4) and one H_{coup} value.

Impact of climate forcings The main impacts of the climate forcings is evident looking at figure 3.6 where is shown how the percentual changes in final grounding line position are larger with the C1 forcing and decrease moving toward the colder C4 climate forcing. As shown in figure 3.3, in a warmer climate the ice flow velocities are higher. A faster flowing ice shelf responds quicker than a slower one to perturbations by the ocean or by the calving process, amplifying the effects that these perturbations have. This suggests that, in a warm climate condition, the impact of external forcings have a magnitude increase with respect to a colder climate state. This explains the observed spread between warmer and colder grounding line positions of figure 3.6 and the larger retreat in figure 3.7.

Impact of ocean melting From figures 3.7, 3.8 and 3.9 the most evident and obvoius result is that after 1000 yr the grounding lines have migrated backward more for higher than for lower ocean melting. Moreover, looking at the percentual changes in figure 3.6, in the case of high ocean melting combinations (group G and H), there is an increase in the spread between the grounding line position relative to colder and warmer climates. In addition, it is interesting to note from figure 3.6, the higher sensitivity to intense ocean melting of the colder climates final grounding lines. In each melting group (A to H), the percentual change corresponding to the more intense combination (bmelt2 = 4 m/yr, 10 m/yr) is larger for colder climate conditions. This suggest that an ice-sheet-shelf system is actually more sensitive to intense ocean basal melting under cold climate conditions, than under warm climate conditions.

Impact of calving For a doubling of the $Hcoup$ thickness criterion for calving, the spread between the grounding line position relative to colder and warmer climates increases.
More importantly, there is a common pattern related to the two H_{coup} ensemble (green and yellow dots in figures 3.7, 3.8 and 3.9). Moving from warmer to colder climate shows that the two ensemble become almost overlapped. The only difference between the green and the yellow dots is the prescribed value of H_{coup} for calving. Thus when the two ensembles are overlapped means that the calving process is playing a minor role with respect to ocean melting in driving the grounding line migration.

Interplay between ocean melting and calving This overlapping pattern is present independently from the initial position of the grounding line or from the channel width considered (B2 bedrock in figures 3.10, 3.11) and can be explained by thinking again at the ice flow velocities. Within the same time period and for a slow flowing ice shelf (typical of a colder climate), ocean basal melting impacts more on the ice-shelf evolution instead of calving. This can be attributed to the ice shelf base remaining longer under the infuence of the ocean melting and thus the dynamical effects induced by calving are less evident or not recognizable in a cold climate.

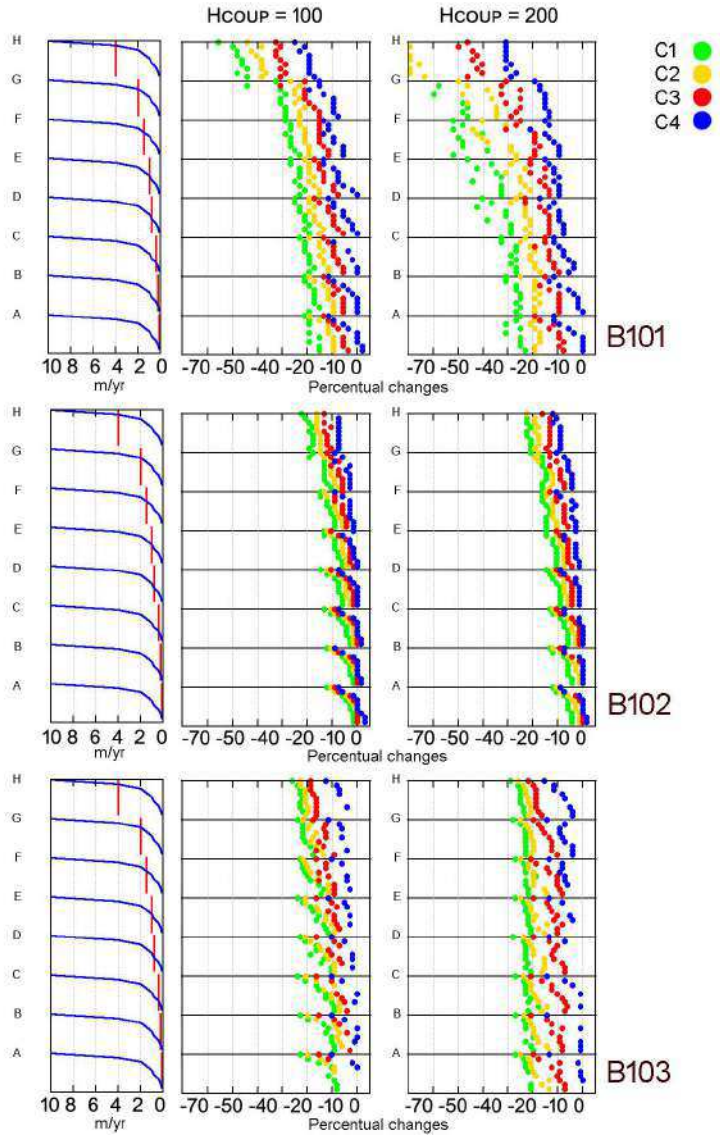

Figure 3.6: *Percentual changes in final grounding line position at the end of the melting experiments. The left panel shows the basal melting groups: going up from group A to group H the total basal melting increases because of higher bmelt1 values (red line). Bmelt2 is denoted by a blue line. Each dot in the central and right panels represents the percentual change in final grounding line position at the end of a melting experiment. Negative percentuale changes correspond to a grounding line retreat, positive percentual changes to a grounding line advance. Zero percentual changes correspond to no-grounding line migration.*

However, between B101/B102 and B103 there is a notably difference in the way through which the two H_{coup} ensembles overlap.
For the B101 shelf, in the warmer climate C1 case (upper left of figure 3.7), the final grounding line positions of group A look already almost unsensitive to variations in H_{coup}. Decreasing the forcing temperature the final grounding line positions become progressively overlapped. In the colder climate condition (C4) the two H_{coup} ensembles, except the dots belonging to group H, are overlapped. Thus for a grounding line starting from and migrating on a prograde bedrock, low values of ocean melting and cold climate conditions make the effects of the calving process to weak. On the contrary, calving remains effective in colder climate for intense ocean melting (group H). This interplay between calving and melting has the following explanation.
When an ice shelf retreats on a prograde slope its ice thickness generally decreases. A decrease in ice thickness increases the possibility that an ice shelf front portion will undergo a calving event (see section 2.1.2). Since for an higher ocean melting the grounding line retreats more, the ice shelf thins more and consequently calving will have higher impacts. The same is true also for the B102 melting experiments that show smaller retreats but the same "overlapping behaviour".
Now the attention can be moved to the B103 case displayed in figure 3.9. Contrary to case B101 the two ensembles start to be overlapped from group H in the warmer climate forcing (C1, upper left of figure 3.9). The same reasoning for B101 can be applied also in this case, with the difference of having the initial grounding line position on the retrograde portion of the bedrock.
When an ice shelf retreats on a retrogade slope its thickness increases, thus decreasing the possibility for calving to occur. So, to higher ocean melting corresponds bigger retreats and ice shelf thickening. This explains why, for combinations of high basal melting values (group H) the final grounding line positions are overlapped even in the warmer climate condition. For lower ocean melting the opposite argument applies, explaining the fact that in the colder climate the final grounding line positions of group A are still different.
However, the above statements about the interplay between ocean melting and calving are conditionally valid, since are related to a very particular idealized bedrock geometry. Thus it is interesting to evaluate how calving and melting are related for another bedrock morphology characterized by a wider channel (bedrock B2). The B2 bedrock morphology is displayed in figure 3.1 and the selected shelves are the one reported in table 3.3 and in figure 3.5. In the following only the absolute changes in grounding line position will be adressed, since a discussion about the percentual changes would be almost identical to the one made for B1.
The results from melting experiments B201, B202 and B203 differ from the ones performed starting from B101, B102 and B103 in one main aspect. Case B201, contrary to B101, does not show any final grounding line position. The reason is that, in the same time span (1000 yr) and with the given bedrock and shelf configuration, any perturbations applied to B201 leads to a total collapse of the shelf. From this perspective, a wider shelf can be considered as more sensitive to calving and melting perturbation for the following reasons:

- First of all, a wider shelf has a bigger basal area exposed to ocean melting and thus the melting impacts are higher with respect to the case of a narrow channel.

- Then, the B201 shelf is thinner than the B101, making the calving process to impact heavier on the ice shelf evolution.

However, the relative role of a more extensive melting and of a greater sensitivity to calving in leading to a complete ice shelf collapse, cannot be quantified from simple arguments. Despite this, some speculations can be made by looking at B202 case. In the two upper panels of figure 3.10, where are displayed the final grounding line positions for the B202 case, only the final grounding line positions relative to the lower H_{coup} value are present. With $H_{coup} = 200$ m, the ice shelf totally collapse. Given the fact that the imposed ocean melting are the same, calving looks to be actually the determinant factor in the ice shelf collapse. However, the selected shelves relative to B2 have generally a lower ice thickness than the ones relative to B1. This difference in ice thickness clearly affects the evolution of the ice shelves, promoting the occurence of calving events and thus complicating a comparison between B1 and B2 ice shelves.
Nevertheless this differences in ice thickness, an interesting comparison between the B1 and B2 experiments can be made. Both B202 and B203 melting experiments show the same "overlapping behaviour" described for case B103, indipendently from the grounding line being on the retrogade or prograde portion of the bedrock. Moreover, the grounding lines have retreated more in the B2 experiments in comparison to the B1 experiments. This suggests that a wider ice shelf results more sensitive to the effects of high ocean basal melting, indipendently from the underneath bedrock morphology. Moreover a widespread melting and the consequently thinning enhances the occurence of icebergs calving, thus amplifying the ongoing retreat. The ocean melting impacting the occurence of calving has also been observed and reported in Liu et al. (2015). Their results suggest that thinning associated with ocean-driven increased basal melt can trigger increased iceberg calving.

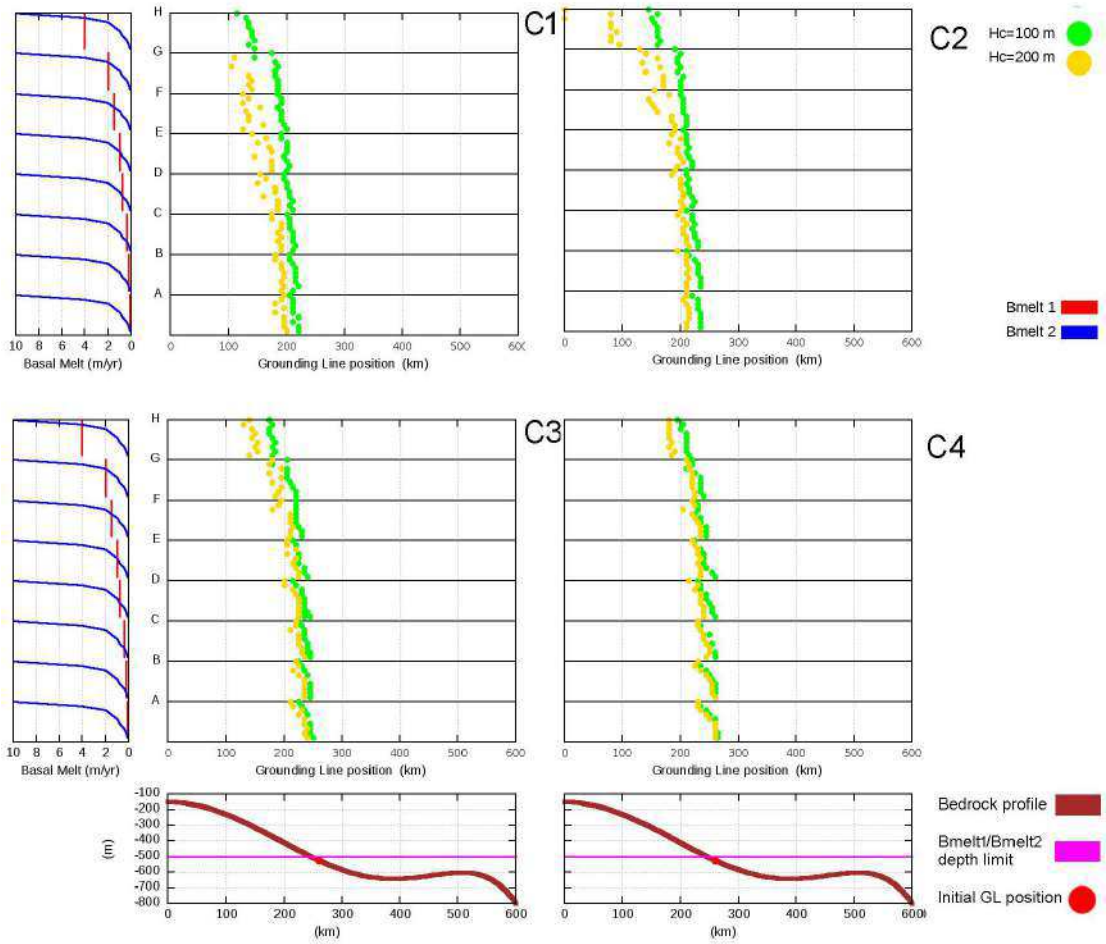

Figure 3.7: *Grounding line migrations for B101 as functions of the H_{coup} thickness criterion and of ocean basal melting. The bottom panel displays the bedrock profile with the initial position of the grounding line (red dot) and the selected depth limit (purple line). The left panel shows the basal melting groups: going up from group A to group H the total basal melting increases because of higher bmelt1 values (red line). Bmelt2 is denoted by a blue line. Each dot in the central panel represents the final grounding line position of each melting experiment. Depending on the used H_{coup} the color of the dot is different (yellow for $H_{coup} = 200$ and green for $H_{coup} = 100$)*

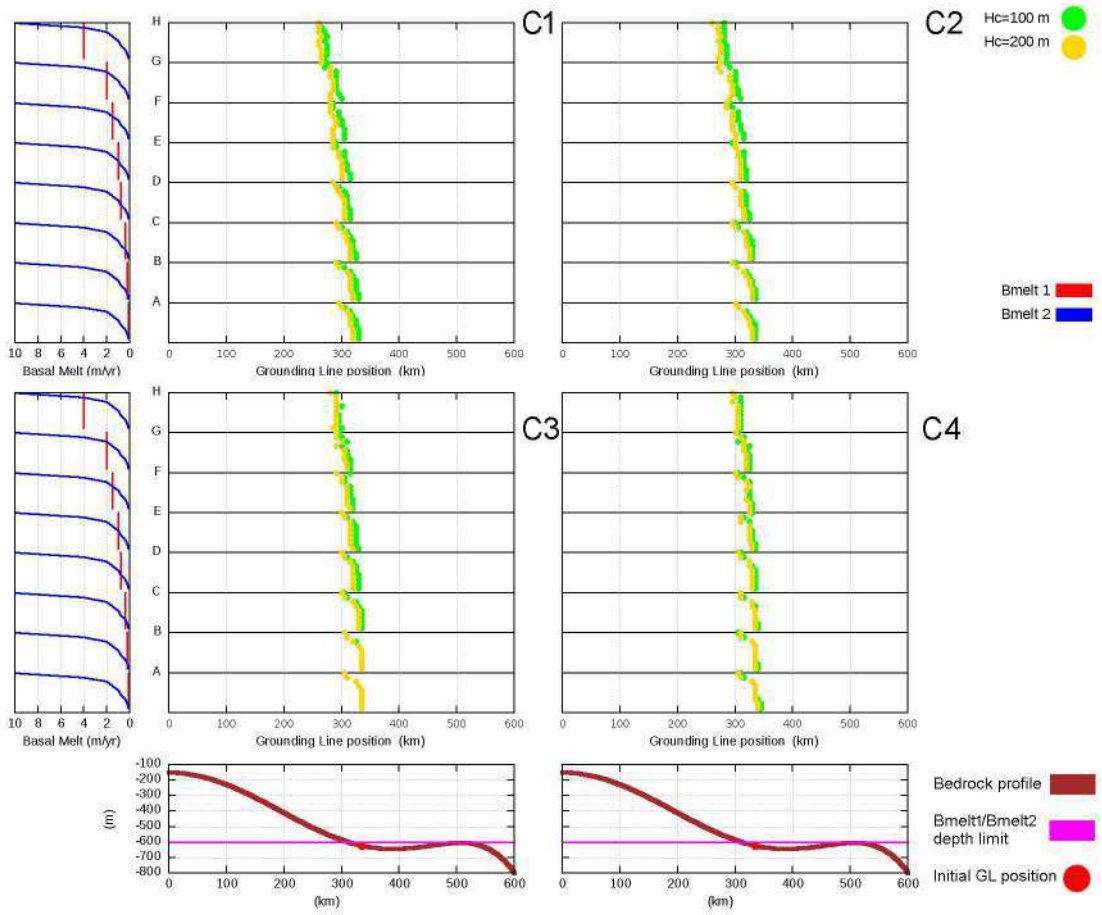

Figure 3.8: *Grounding line migrations for B102 as functions of the H_{coup} thickness criterion and of ocean basal melting. The bottom panel displays the bedrock profile with the initial position of the grounding line (red dot) and the selected depth limit (purple line). The left panel shows the basal melting groups: going up from group A to group H the total basal melting increases because of higher bmelt1 values (red line). Bmelt2 is denoted by a blue line. Each dot in the central panel represents the final grounding line position of each melting experiment. Depending on the used H_{coup} the color of the dot is different (yellow for $H_{coup} = 200$ and green for $H_{coup} = 100$)*

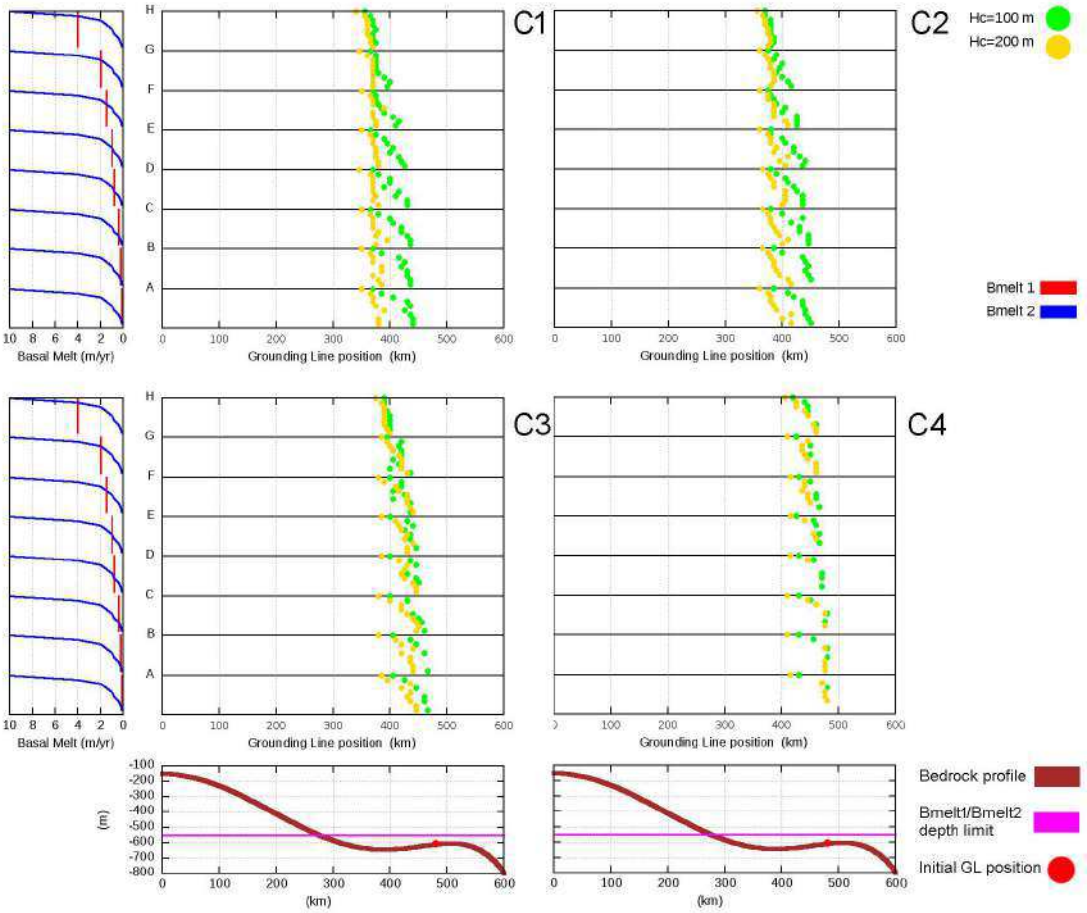

Figure 3.9: *Grounding line migrations for B103 as functions of the H_{coup} thickness criterion and of ocean basal melting. The bottom panel displays the bedrock profile with the initial position of the grounding line (red dot) and the selected depth limit (purple line). The left panel shows the basal melting groups: going up from group A to group H the total basal melting increases because of higher bmelt1 values (red line). Bmelt2 is denoted by a blue line. Each dot in the central panel represents the final grounding line position of each melting experiment. Depending on the used H_{coup} the color of the dot is different (yellow for $H_{coup} = 200$ and green for $H_{coup} = 100$)*

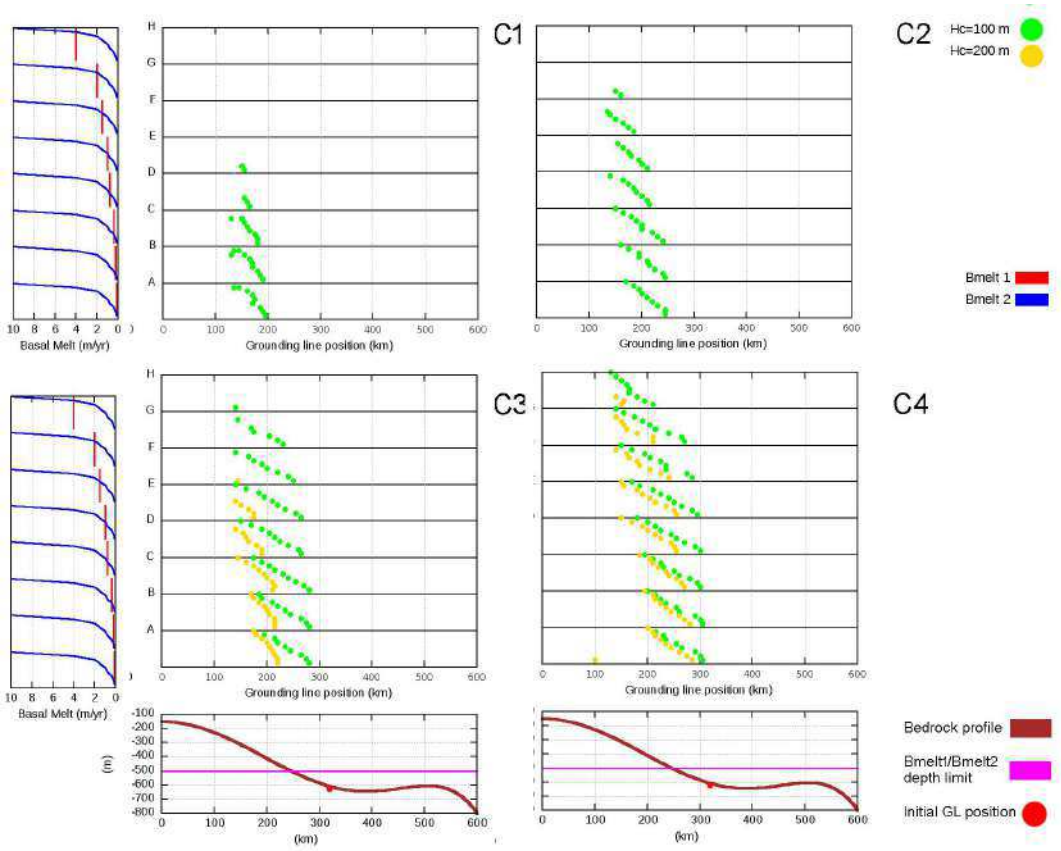

Figure 3.10: *Grounding line migrations for B202 as functions of the H_{coup} thickness criterion and of ocean basal melting. The bottom panel displays the bedrock profile with the initial position of the grounding line (red dot) and the selected depth limit (purple line). The left panel shows the basal melting groups: going up from group A to group H the total basal melting increases because of higher bmelt1 values (red line). Bmelt2 is denoted by a blue line. Each dot in the central panel represents the final grounding line position of each melting experiment. Depending on the used H_{coup} the color of the dot is different (yellow for $H_{coup} = 200$ and green for $H_{coup} = 100$)*

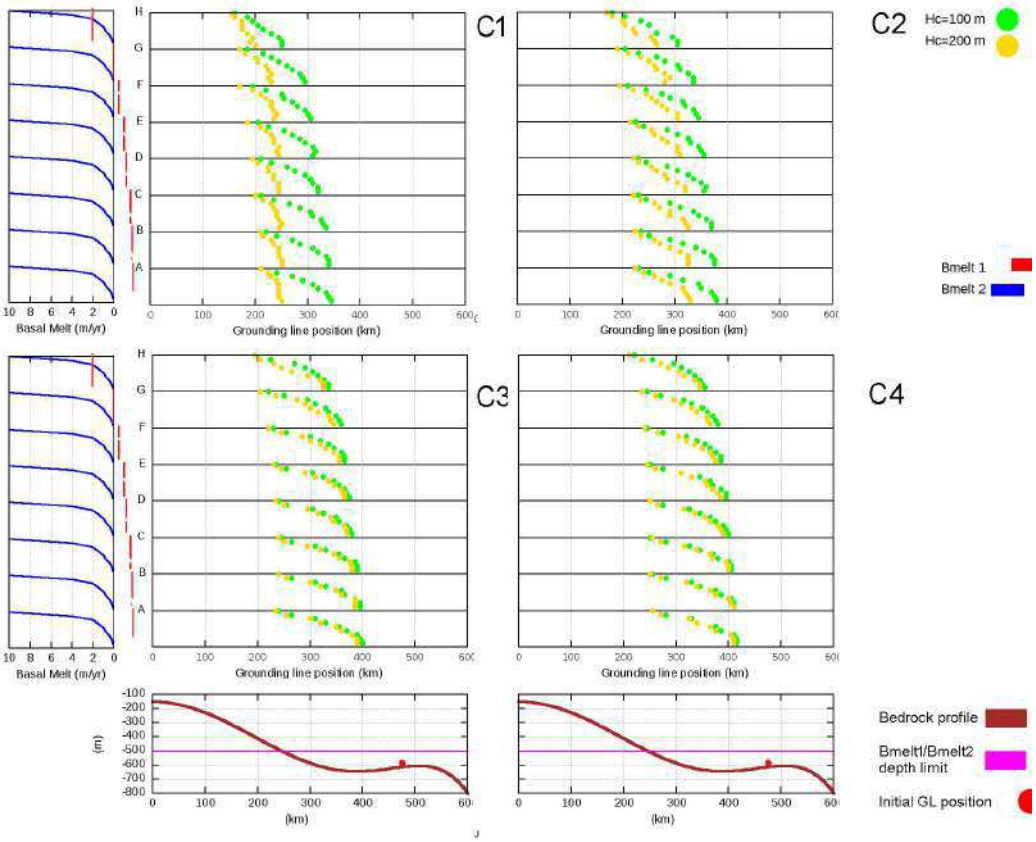

Figure 3.11: *Grounding line migrations for B203 as functions of the H_{coup} thickness criterion and of ocean basal melting. The bottom panel displays the bedrock profile with the initial position of the grounding line (red dot) and the selected depth limit (purple line). The left panel shows the basal melting groups: going up from group A to group H the total basal melting increases because of higher bmelt1 values (red line). Bmelt2 is denoted by a blue line. Each dot in the central panel represents the final grounding line position of each melting experiment. Depending on the used H_{coup} the color of the dot is different (yellow for $H_{coup} = 200$ and green for $H_{coup} = 100$)*

3.3.2 A comparison of ocean basal melting formulations

Four formulations for ocean basal melting were presented in chapter 2, and each of them presents its own peculiarities. Thus it is interesting to evaluate, for the same ocean temperature and salinity, whether or not, the parameterized ocean melt rates computed by those formulation converge or not. Given the impact that ocean melting has on the evolution of an ice-sheet-shelf system, it is thus necessary to asses the consequences of using one formulation instead of another.
We force the four ocean melting formulations with a spatially uniform vertical profile of temperature T$=-1.7$°C and salinity S$=35$ psu (figure 3.12). The results demonstrate that, depending on the formulations used, the melt rates largely differ. Here the ocean basal melting increases with depth, although the profile of temperature and salinity is vertically uniform. This is due to the pressure dependence of the freezing point of seawater. In the end, this can be considered as the impact of depth on melt rates. Moreover, the importance of the ice shelf slope on ocean melting is captured only by the plume formulation, showing increasing melting when the shelf base becomes steeper.
The four formulations are then applied for 1000 yr to B101, B102 and B103. The percentual changes in final grounding line positions are evaluated in figure 3.13. As expected by the formulation-dependent melt rates shown in figure 3.12 also the final grounding line positions do not converge to a common final value. Moreover, the impacts vary depending on the initial position on the bedrock and on the ocean conditions. Only in the above panel the four final grounding lines look to converge to a common value.

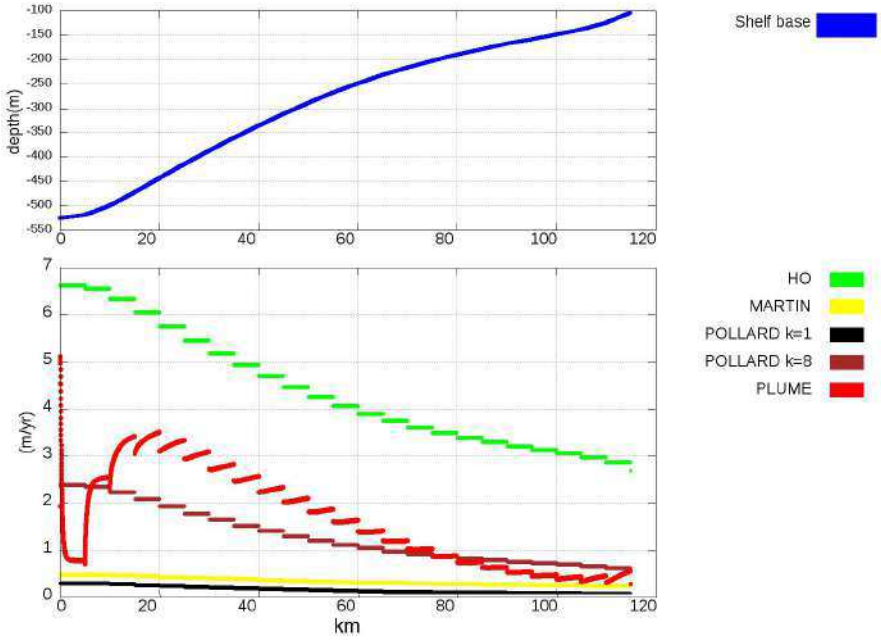

Figure 3.12: *Comparison of the four different ocean melting formulations forced by a vertical uniform profile of temperature T = -1.7 ° C and salinity S = 35 psu. Top panel: ice shelf draft depth for the B101 spin up configuration. Bottom panel: melt rates obtained using the foru formulations. The melt rates profile are discrete because of the discrete resolution of GRISLI.*

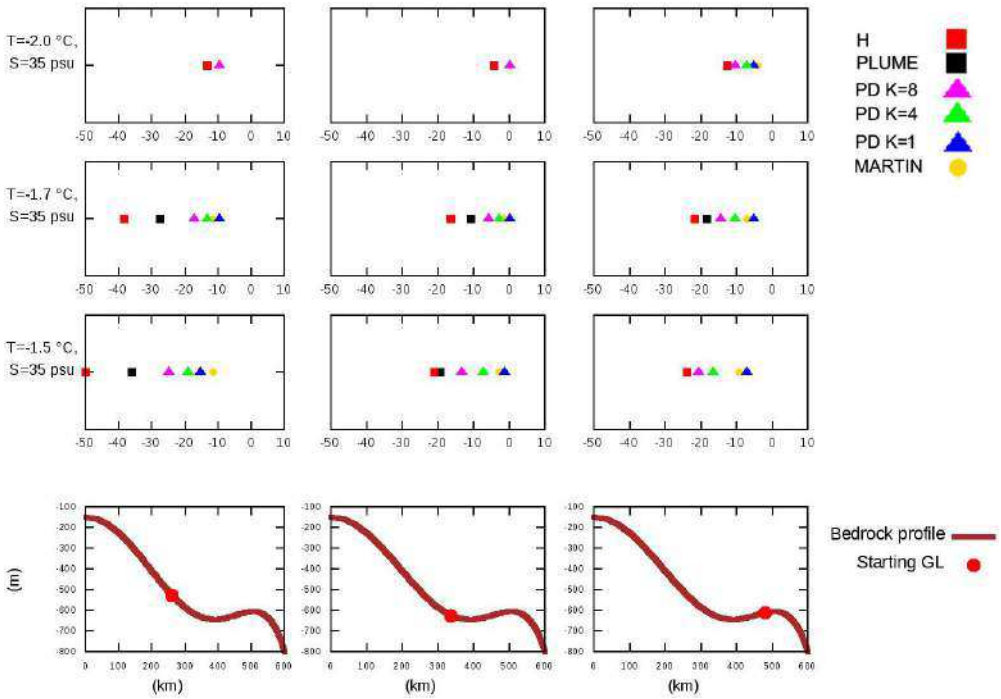

Figure 3.13: *Percentual changes in the grounding line position for the melting experiments using the four ocena melting formulations. In the top three lines are dsplayed the percentual changes relative to three different combination of ocean temperature and salinity, while in the bottom line the relative initial condition. In the bottom line: B101 (left), B102 (center) and B103 (right).*

However this can be attributed to the prescribed temperature ($T = -2^{\circ}$ C). An ocean water with this temperature has a low melting potential and thus limits the impacts on grounding line migration.
Given the magnitude of the simulated impacts on grounding line in this idealized framework, the impacts of using different formulations for ocean basal melting are investigated in details in the next chapter for two realistic cases.

3.4 Discussion

In this chapter, I investigated the response of the grounding line to the calving and ocean melting forcings. The aim was to understand the interplay between these two processes, especially as function of the mean background climate states and of the bedrock morphology. All the experiments have been performed with the hybrid ice-sheet-shelf model GRISLI at a 5 km of resolution. An hybrid SSA/SIA model does generally not represent the best model choice to investigate grounding line migration as it has been shown in some model intercomparison projects (MISMIP, MISMIP3D). In this intercomparison exercises, shallow approximation models (such as GRISLI) have shown to fail in reproducing grounding line migration correctly (Pattyn et al., 2012). This is true in particular for resolutions around 20 km at which continental-scale simulations are typically done (Huybrechts and de Wolde, 1999; Pollard and DeConto, 2009; Greve et al., 2011; Martin et al., 2011; Ritz et al., 2015). However, running paleo and future AIS simulations at resolution of hundreds of meters (as suggested for hybrid models in Docquier et al., 2011), with the present-day computational possibilities, is still not feasible. Thus, if

the aim of a study is to reconstruct or predict the past or future evolution of the AIS, the only available tools are hybrid ice-sheet-shelf model as GRISLI. This has motivated, in the first place, the choice of using GRISLI. In the modelling community other hybrid ice-sheet models, in order to match the requirements of the MISMIPs experiments, use flux corrections at the grounding line based on heuristic rule (e.g. Ritz et al., 2015; Pollard and DeConto, 2016). However, these flux corrections and their implementation are highly model dependent. From this point view, it was considered more robust to use GRISLI at high resolution, instead of running the experiments with models that make use of such internal tuning to the present-day grounding line fluxes. Moreover, the interest was to investigate how ocean melting and calving impact the grounding line migration and not in reconstructing, as an example, the correct grounding line position of an Antarctic ice shelf. Thus the real focus of this conceptual work is on the relative differences in grounding line migration due to the increase or decrease in magnitude of calving or ocean basal melting, and not on absolute positions.
Given these considerations on model capabilities, the main results from section 3.3 can be summarized as follow:

- under cold climate conditions, the ice shelf evolution is mainly driven by ocean melting.
- for certain ice shelf widths and for a grounding line starting from and migrating on a prograde slope, the calving process takes over ocean basal melting in driving the grounding line for high melt rates.
- for certain ice shelf widths and for a grounding line starting from and migrating on a retrogade slope, the calving process takes over ocean basal melting in driving the grounding line for low melt rates.
- in the case of large shelves, ocean basal melting becomes the dominant driver on the grounding line migration, eventually enhancing the occurence of calving due to the thinning of ice shelves.

These results have been obtained by forcing the model with different idealized climate states, ocean melting rates and calving threshsolds. However, although our prescribed melt rates are in the range of the observations (Rignot et al. (2013) and Depoorter et al. (2013)), this is not the case for the simulated calving process. As described in section 1.2.2, calving is an important mechanism for mass loss but, unfortunately, modeling of calving processes is still a major challenge. This lack of robust implementations of the calving process could question the ability of ice-sheet models to simulate past or future extension of the AIS. The inherently difficulty in developing a satisfying calving law is due to the fact that:

- a full calving model should take into account the different timescales at which the icebergs detach, the evolution of glacier geometry and the stress fields that arise when an ice block detaches (Pralong and Funk, 2005).
- the lack of observations and perhaps knowledge of missing mechanical processes to constrain the models.

However, in the last decades, several parameterizations of the calving process have been proposed and implemented. Some of these parameterizations relate calving to the ice-

shelf front thickness (as in GRISLI) while others consider the ice shelf strain rates (Levermann et al., 2012). Thus the calving occurence in GRISLI, as in all the other numerical ice-sheet models, is tightly related to the implemented calving formulation. However, in the sensitivity experiments the focus was not on the calving occurence but on the effects induced by calving on grounding line. A more detailed discussion about calving parameterizations is provided in the final discussion. The last thing whorty of discussion and that may need further investigations is the impacts of the degree of ice-shelf buttressing in the observed results. In general, for an unconfined ice shelf (or for a lower buttressing condition), ocean melting and calving should not impact the grounding line evolution (Gudmundsson, 2013). Hence, an improvement of this work would consist in performing new experiments, simulating idealized uncofined ice shelves and comparing the results with the case of confined ice shelves (already shown in this chapter). This because, in general, an increase in ice-shelf width decreases the buttressing effect on the ice interior (see equation 1.29). From this perspective, when in section 3.3 the ice-shelves width were increased (case B202 and B203), the buttressing effect decreased. This suggests that a decrease in the buttressing by ice shelves on the ice sheet interior makes the grounding line dynamics less sensitive to how the calving and melting process interact with each other and with the underlying bedrock.

Ocean basal melting plume model: application to Antarctica

4.1 Introduction

A comparison between the different ocean basal melting formulations has been presented in the previous chapter. The impact of the choice of the basal melting formulation on grounding line migration is huge, thus potentially affecting the entire ice-shelf/ice-sheet evolution. However most of the experiments were performed in an idealized framework, with thus a limited possibility to extrapolate the results to some realistic case.
The focus of the present chapter now shifts to investigate Pine Island Glacier (PIG) and Totten Glacier (TG) that, as illustrated in section 1.1.3, represent two hotspots of the WAIS and EAIS where the interaction with the ocean is crucial. Several studies using stand-alone ice-sheet models have adressed the future evolution of PIG and TG (e.g. Favier & Gudmundsson 2014; Sun et al. 2016) but none of them have tackled the problem of which ocean basal melting formulation is the most appropriate to use in a stand-alone ice-sheet model. In general, melt rate formulations are designed ad-hoc for the study area and tuned to present-day observations (Rignot et al. 2013; Depoorter et al. 2013). However, a tuning on present-day ocean conditions may be valid only if ocean conditions remains similar, thus raising the need for a more general ocean basal melting treatment in ice-sheet models. The first step in this direction, is to compare the existing formulations/parameterizations and evaluate their impact on the grounding line migration of existing ice-shelves and on the ice discharge into the ocean.

4.2 Experimental design: Pine Island and Totten Glaciers

The numerical experiments of this chapter have been performed with the Úa ice sheet model running the SSA (see section 2.1.3 and Gudmundsson 2012) and have the following structure:

- Initialization phase: Úa is initialized with the present-day ice thickness and bedrock elevation and by assimilating the observed satellite ice velocities to retrieve basal friction and ice viscosity (see section 2.1.3).
- Relaxation phase: the model evolves freely for 15 years in order to relax the interpolated ice thickness field.
- Sensitivity phase: the model is forced by different ocean basal melting formulations forced by realistic ocean conditions while surface mass balance is kept fixed (more details in the following sections).

4.2.1 Model setup and initialization

The Úa initialization was performed with ice thickness and bedrock elevation from the same dataset for both Pine Island (PIG) and Totten Glacier (TG). The same observed ice velocities dataset was used to perform the inversion procedure necessary to retrieve basal friction and ice viscosity. The initial fields for bedrock elevation(B), surface (s)

and bottom (b) ice elevations are taken from BEDMAP2 at 1 km resolution (Fretwell et al. 2013) while the observed ice-flow velocities ($\mathbf{u}$) come from Rignot et al. (2011). For TG, a modification of the bedrock elevation of BEDMAP2 was needed since the sea bed morphology beneath the Totten area is poorly represented in BEDMAP2 (Sun et al. 2014).Greenbaum et al. (2015) showed that downstream from the grounding line the bedrock below TG ice shelf is actually deeper than in BEDMAP2, possibly allowing warmer water to reach deeper portions of the ice shelf and thus enhancing melting (Greenbaum et al. 2015). However, for the purpose of this thesis, the impact on TG dynamics is limited to the possible presence of more and higher pinning points and does not account for the effects that this deeper cavity has on ocean circulation (since no 3D ocean circulation module is present in Úa). Following the work of Sun et al. (2016), the bottom bathymetry has been modified by gradually deepening the Totten cavity of 500 m along its length axis and so that no additional deepening occurs in the vicinity of the grounding line.
The surface mass balance field (present-day condition) comes from van de Berg et al. (2006) and is kept fixed in all the experiments. Moreover, no surface elevation feedback is employed in the following simulations. This means that the surface mass balance is not updated while ice extent and elevation changes during runtime. For most of the experiments analyzed in this section, ice density has been assumed horizontally homogeneous and set to 918 kg/m^3.
As explained in section 2.1.3, Úa allows for Automated Remeshing during runtime. However, in all the experiments of this thesis, the finite elements computational mesh was kept fixed. For both PIG and TG, a fixed unstructured mesh has been used. The computational meshes have been built in order to have high resolution in the nearby areas where the grounding line can eventually advance or retreat. In order to avoid the loss of any dynamical contribution to the ice flow, the PIG and TG computational meshes are representative of the ice drainage basins from Zwally et al.,(2012) (see appendix). The meshes features are summarized in table 4.1 and represented in figure 4.1.

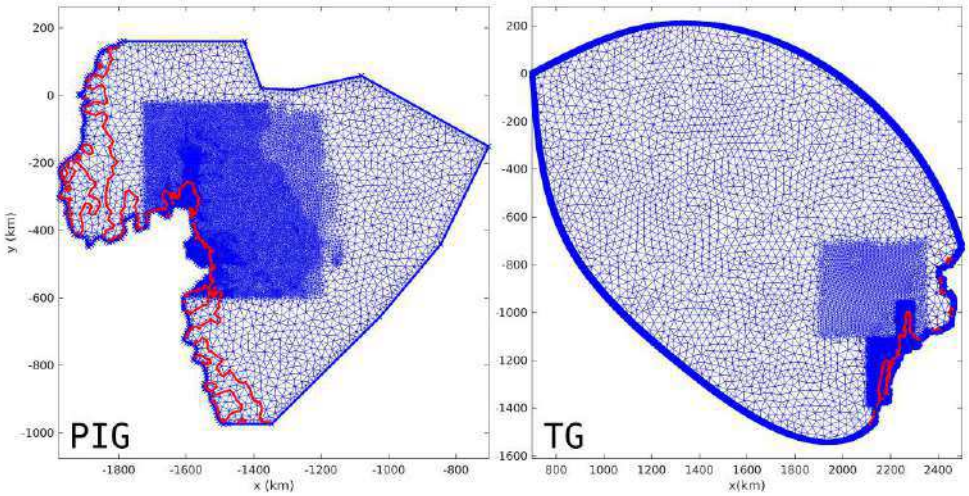

Figure 4.1: *Unstructured computational meshes for Pine Island and Totten glaciers. The boundary of the meshes approximates the ice drainage basins given in Zwally et al. 2012. The red line represents the initial modelled grounding line obtained by Úa.*

Ice shelf	Mean(m)	Median(m)	Maximum(m)	Minimum(m)	Total elements
PIG	4872	3934	30023	682	38912
TG	3797	875	44360	382	58333

Table 4.1: Mesh elements size for the PIG and the TG domains.

Figure 4.2 displays the obtained model ice velocites after the inversion. The modelled velocities are in good agreement with measurements for both PIG and TG. The only substantial differences are located in the upstream sector of PIG where the velocities are slightly under-estimated and on the western side, where minor ice fluxes into the ice shelf are not well reproduced.

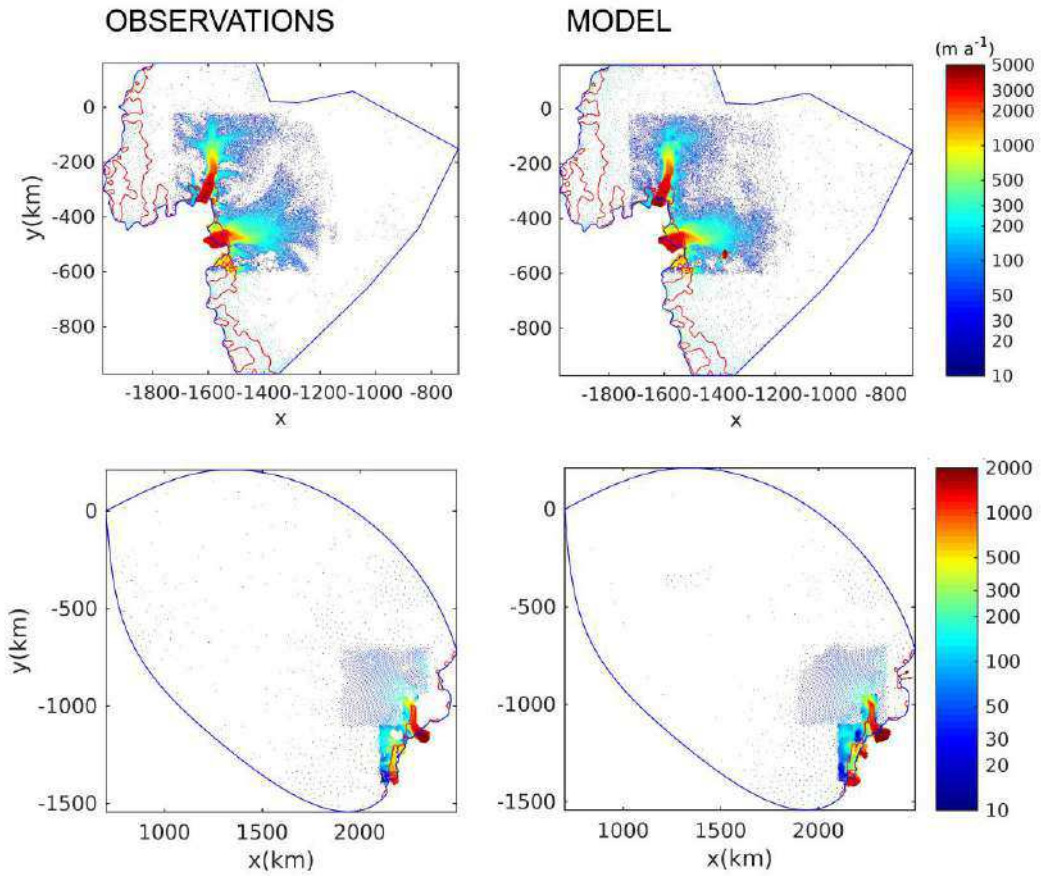

Figure 4.2: *Comparison between measured velocities by Rignot et al., (2011) and model velocities after inversion. The top panels represent PIG, the bottom panels represent TG.*

In addition to the description of the 1D plume provided in section 2.2.5, the following adjustments have been done to perform the experiments. Since the 1D plume equations are coded in finite differences and thus solved on a regular grid (there set to 1 km resolution), an interpolation from the unstructured mesh of Úa was necessary. The plume equations are solved on the ice-shelf draft, using its depth and slope (see section

2.2.5). The selected ice-shelf profile is approximated by the hypotenuse of the triangle shown in figure 4.3.
Moreover a rotation of the regular grid is performed, with the aim of having the ice shelf base spanned by a set of plumes rising perpendicularly from the grounding line to the ice-shelf front, without any deviation from a straight line. This need for rotation arises because the 1D plume does not accounts for the Coriolis effect and any deviations from a straight line would be artefact. Once all the plume equations are solved and the melt rate distribution has been obtained, this can be interpolated back to the unstructured mesh of Úa. The rotation of the grid has been necessary and performed for both PIG and TG (see figure 4.4).

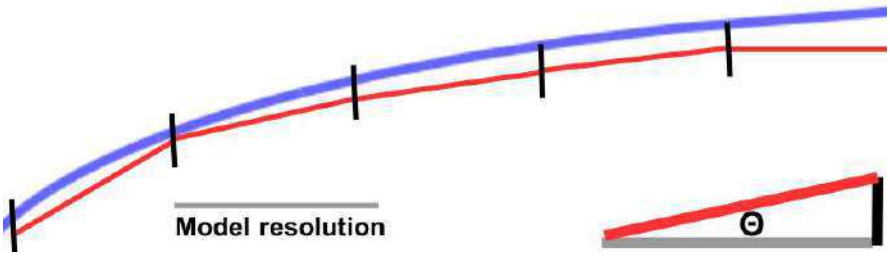

Figure 4.3: *The ice-shelf draft profile (in blue) is approximated by a series of inclined lines (in red). Each of these lines is the hypothenuse of the triangle that has a leg of 1 km (the regular grid resolution length, in grey) and the other leg equals to the change in ice-shelf draft depth (in black) from one cell grid to another.*

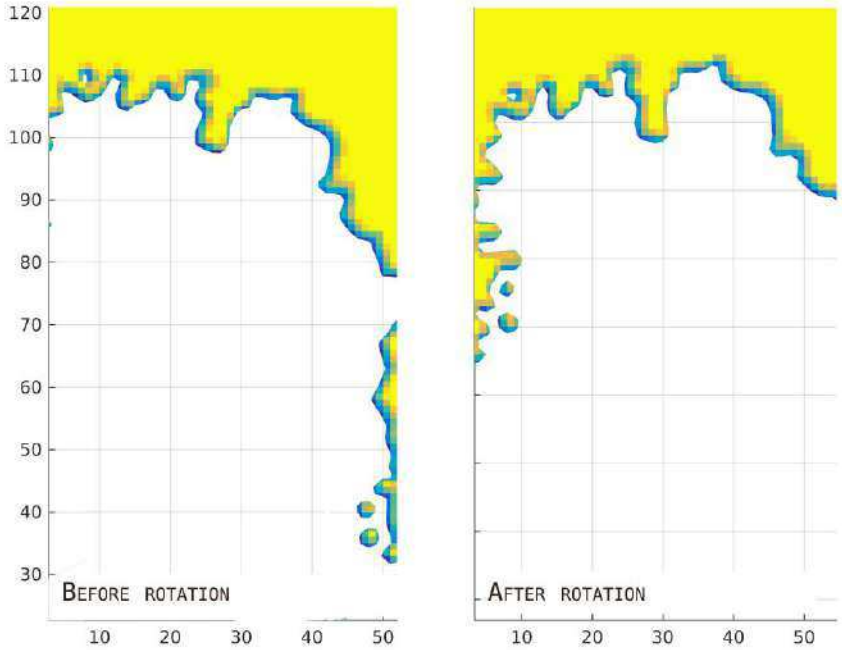

Figure 4.4: *Pine Island Glacier grounding line interpolated on the regular 1 km grid before (left) and after the rotation (right). The yellow part indicates the grounded ice while the white part represents the floating ice shelf.*

4.2.2 Relaxation phase

Relaxing the model is needed to adjust the initial geometry to the computational mesh and to smooth the boundary conditions to data collected on different time frames, (Favier et al., 2014). The relaxation run consists in a transient simulation of 15 model-years forced by the surface mass balance field parameterized from Van de Berg et al. (2006) and by a parameterized ocean melt rate vertical profile (figure 4.5) based on inferred melt rate estimates. Calving, as in all the other and following experiments, is not allowed. Thus the ice-shelf front position is fixed as well as the areal extension of the selected drainage basin. The grounding line, on the contrary, moves freely. As the grounding line evolves, what really changes in the computational domain is the fraction of floating ice.
The ocean melting used for PIG depends on depth and sets the melt rate equal to 100 m/yr for depths below -800 m, while for shallower depths the melt rate decreases linearly to zero until -400 m (figure 4.5). For depths above -400 m, the sub-shelf melt rate is set to zero. The same forcing method has been used in Favier et al. (2014) and is based on observations and measurements of in-situ ocean conditions combined with modelling (Bindschadler et al. 2011, Dutrieux et al. 2013, Jacobs 2011).
A value of 100 m/yr at the grounding line is almost an order of magnitude higher than the melt rates given by Rignot et al. (2013) and Depoorter et al. (2013) (see table 4.3). However, as it will also be discussed later, the values given in Rignot et al. (2013) and Depoorter et al. (2013) are melt rates averaged on the entire ice shelf area and thus only valid to estimate the total discharge of ice into the ocean. But, to correctly simulate ice-shelf dynamics, it is crucial to have the most reliable melt rates at the grounding line (and hence the correct spatial melting distribution). For PIG, Bindschadler et al. (2011) and Dutrieux et al. (2013) provide estimates of melt rates distribution, showing very high melting close to the grounding line (around 100 m/yr) and largely decreasing towards the ice-shelf front.

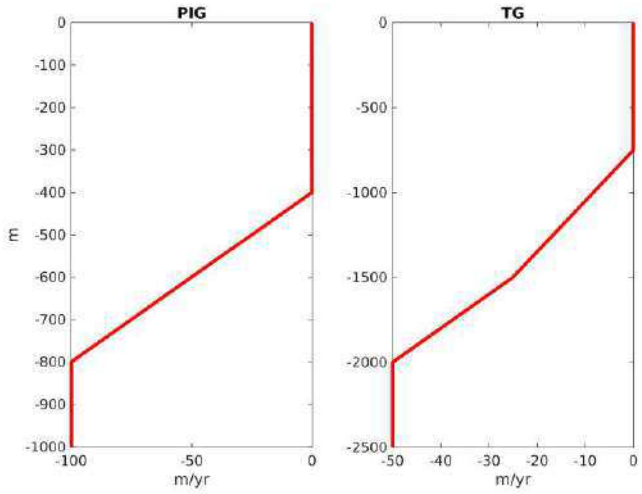

Figure 4.5: *Pine Island and Totten Glacier vertical ocean melting profile used in the relaxation runs.*

For TG, the ocean melt rate is again imposed as a piecewise linear function of the water depth. This depth-dependent melt rate is based on the results of Gwyther et al.

2014, who estimated the ocean melting below the Totten shelf to about 50 m/yr at the grounding line and decreasing to almost zero toward the calving front. Therefore, underneath TG, the ocean melting is equal to 50 m/yr below -2000 m and linearly decreasing to 25 m/yr at 1500 m of depth. From -1500 m to -500 m, the melt rate decreases linearly from 25 m/yr to 0 m/yr, and remains 0 m/yr above 500 m (figures 4.7). Figure 4.7 displays the spatial melt rate distributions, while the ice shelf base elevations for both PIG and TG are shown in figure 4.6.

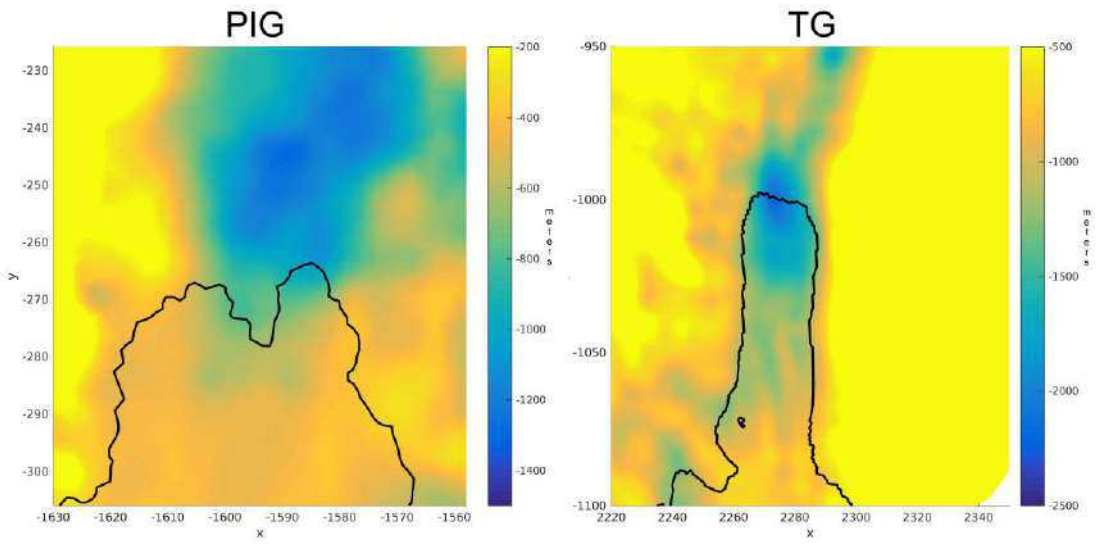

Figure 4.6: *Depth of ice-shelf base (m) for PIG (left) and TG (right). Note the different depths scales.*

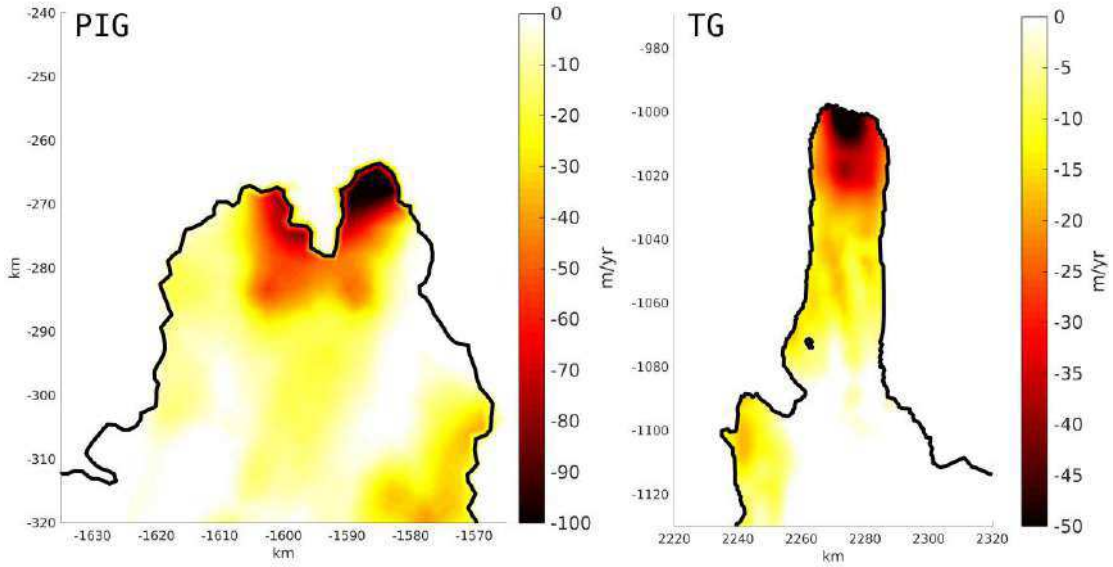

Figure 4.7: *Spatial distributions of the ocean melting rates used in the relaxation phase and based on melt rates profiles for PIG (left) and TG (right) of figure 4.5. Note the different scale for melting values.*

4.2.3 Ocean basal melting experiments

In all the experiments, the four formulations for ocean melting presented in 2.2 are forced by observation-based ocean vertical Temperature and Salinity profiles (TS profiles) and applied to both PIG and TG.
The initial condition for all the following experiments is the final state obtained at the end of the relaxation run.
From here on, the ocean melting formulations will be adressed as POLLARD for the Pollard and DeConto (2012) (with K_{shelf} equals to 8 as in their work), MARTIN for Martin et al. (2011), HELMER for the Helmer and Olber (1989) and PLUME for the plume model developed during the Ph.D. (based on Jenkins, 1991).
The TS profile for TG is based on the data gathered from Rintoul et al. (2016) (figure 4.8, Rintoul et al. 2016) and based on deRydt (2016) for PIG (figure 4.8, Rydt & Gudmundsson 2016). This last profile has been obtained by simplifiyng the observational records from the Pine Island Bay presented in Jacobs et al. (2011). For TG the observations of temperature and salinity from Rintoul et al. (2016) do not go deeper than -1000 m and thus the TS profile has been extended down (figure 4.8).
Two cases have been considered:

- Cold: In the deeper part, water is assumed to have properties similar to AASW ($T = -1.4°C$ and $S = 34.3psu$)

- Warm: In the deeper part, water is assumed to have properties similar to mCDW ($T = -0.7°C$ and $S = 34.7psu$)

The choice of using two different TS profiles is motivated by the fact that there are no existing ocean temperature and salinity observations in the deep cavity below TG. Hence using these two TS profiles provide a lower and an upper limit for the possible temperature and salinity range occuring in the cavity.
In the following section, only sensitivity experiments based on the cold TS profile are analyzed while the experiments based on the warm TS profile are adressed in section 4.3.2.
The cold profiles are motivated by the fact that the access to the cavities is thought to be regulated by narrow channels; thus presumably preventing large exchanges from the warmest water to the one in the cavity (Silvano et al. 2016).
The melting experiments have run for 20 years for both PIG and TG. However, in the following, analysis is based on the model outputs obtained after 10 years of simulations. This because PIG is generally in a favourable unstable condition, and its grounding line crosses the retrograde bedrock slope area while retreating after 20 years of simulation(Schoof, 2007; Favier et al., 2014).
Since the purpose of this chapter is to evaluate the impacts of the ocean formulations, in order to isolate this effect, the following approach has been followed. The analysis is performed at a selected time of the runs such that, the PIG grounding line does not cross the upsloping portion of the bedrock (10 model years).
In order to have comparable results, the analysis of TG runs is also performed at 10-model years, although the inherently major stability of the EAIS and the absence of any known instability mechanism in the TG area.

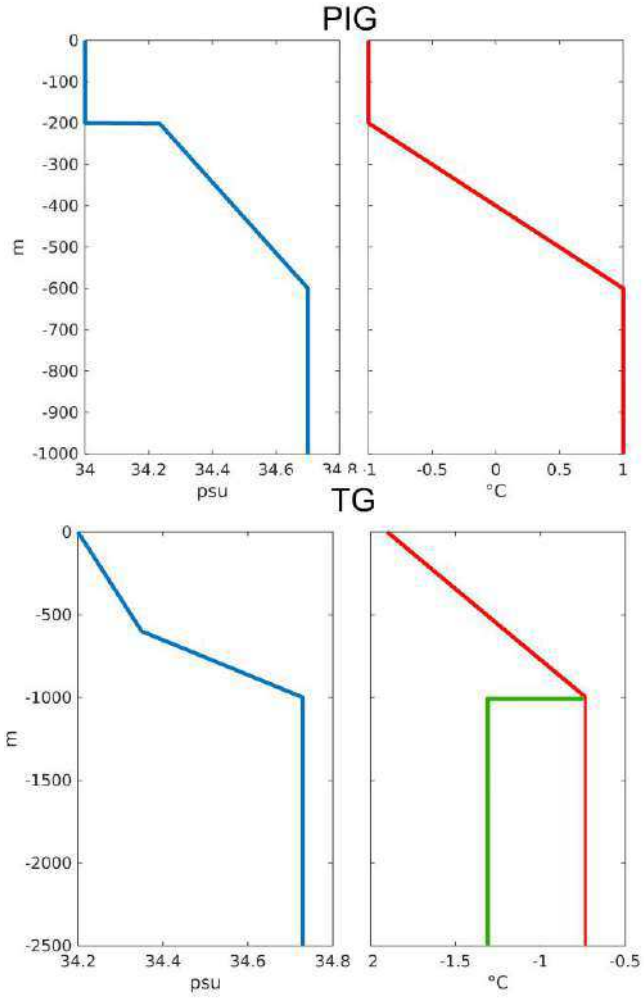

Figure 4.8: *Temperature and salinity profiles prescribed to force the melting formulations for Pine Island Glacier (upper panels) and Totten Glacier (bottom panels). The salinity profiles are displayed in blue while the temperature profiles are displayed in red. For TG are plotted two temperature profiles (red and green). The red one represents the warmer case, while the green one the colder case (see section 4.3.2.*

4.3 Results

The final grounding line positions, the melt rate distributions and the ice discharge values obtained for PIG and TG are presented in this section as the results from the:

- Sensitivity experiments forced by the TS profiles given in section 4.2.1.
- Experiments in which the TS profiles are perturbed.
- Experiments in which ice density is varied.

Here the ice discharge represents the integrated melt rate over the underside of the ice shelf and is measured in Gt/yr. In the last section, the four ocean basal melting formulations are applied to the entire AIS.

4.3.1 Grounding line, melting distribution and discharge rate

The initial and final grounding line positions for each ocean basal melting formulations are plotted in figure 4.9. The use of POLLARD and MARTIN formulation leads to an advance of the grounding line for both PIG and TG. This is especially visible for TG, where the forward migration is between 5 and 10 km from the initial position, while PIG grounding line, seems less sensitive to the different formulations, except when using HELMER.
In fact, the HELMER formulation gives a retreat in both PIG and TG of about 10 km and of 3 km circa, respectively. The coupled plume model gives similar results to HELMER in TG, while for PIG the grounding line experiences a small retreat or remains stable. Depending on the formulation used, the grounding line retreats, remains stable or advances. These differences in final grounding line positions are mainly determined by the computed melt rate distribution (Figures 4.10 and 4.11).
All the melting formulations exhibit, consistently with estimates (Rignot et al. (2013); Depoorter et al. (2013); Bindschadler et al. (2013); Gwyther et al. (2014)), higher melt rates in the deep grounding line proximity (table 4.2). All four formulations capture the signal of warmer water at intermediate depths (500 - 1000 m) for TG. The four melt rates distributions show two maxima: one at the grounding line and one in the middle of the ice shelf. The maximum value simulated at the grounding line, although the water is colder than at mid-depth, is due to the pressure dependence of the melting point leading to high melt rates (grounding line depth for TG is around and below 2000 m). On the other hand, altough the ice base in the middle of the ice-shelf is not as deep as in the grounding line area (figure 4.6), the computed melt rates are high due to the increase in ocean temperature prescribed in the TS profile (figure 4.8). HELMER gives the higher melt rate while MARTIN is the one giving the weaker melting. POLLARD shows melt rates similar to the average values given in Rignot et al. (2013) and Depoorter et al. (2013) while the PLUME formulation presents values comparable with the distributions obtained in Bindschadler et al. (2011) and in Gwyther et al. (2014) for PIG and TG respectively. Note that the linear behaviour of the MARTIN formulation is distinguible from the other ones. In fact, MARTIN is the only formulation not leading to an abrupt melt rate difference between the grounding line and the calving front.

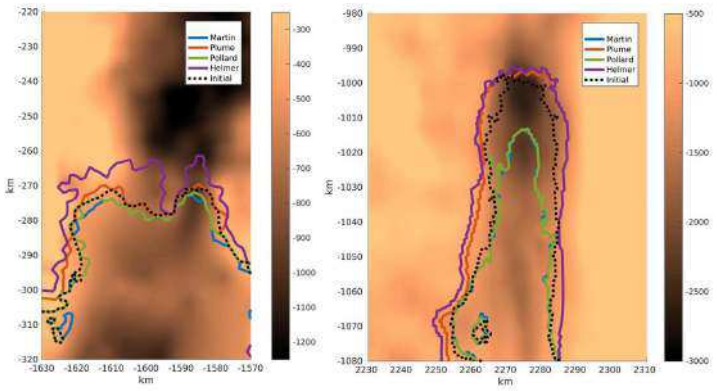

Figure 4.9: *Grounding line position at the end of the melting experiments for Pine Island (left) and Totten Glaciers (right). Initial grounding line (black dotted), PLUME (red), POLLARD (green), MARTIN (blue), HELMER (purple).*

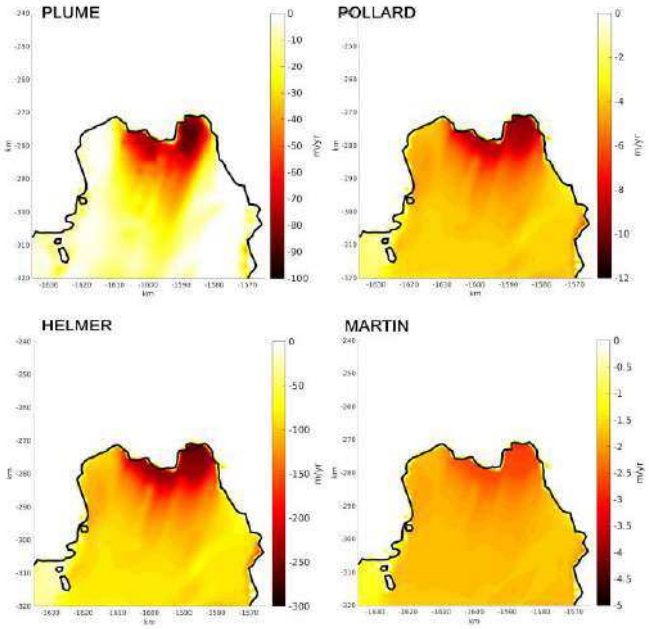

Figure 4.10: *Melt rates distribution for Pine Island Glacier. PLUME (upper left), HELMER (bottom left), POLLARD (upper right), MARTIN (bottom right). The black line corresponds to the grounding line. For both glaciers, the distributions are represented with a different color scale for each formulation, given the difference in the melt rates magnitude.*

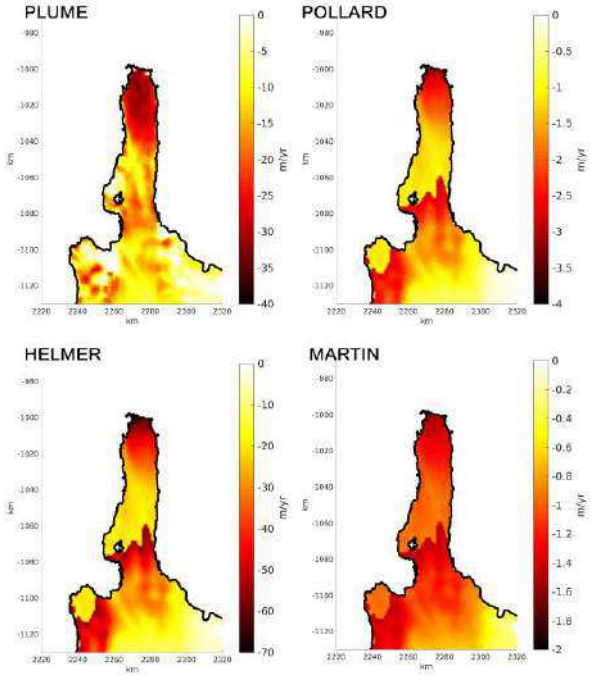

Figure 4.11: *Melt rates distribution for Totten Glacier. PLUME (upper left), HELMER (bottom left), POLLARD (upper right), MARTIN (bottom right). The black line corresponds to the grounding line. For both glaciers, the distributions are represented with a different color scale for each formulation, given the difference in the melt rates magnitude.*

Thus, from table 4.2, the POLLARD and PLUME formulation appears as the only ones in line with observational records. However, the melt rates given by Rignot et al. (2013) and Depoorter et al. (2013) have not been directly measured but computed dividing the inferred ice discharge into the ocean by the total ice-shelf area times the ice density and thus represent averaged melt-rates. Thus, in order to realistically compare our calculations with the observations, the averaged melt rates and the ice discharge are calculated from our simulations (figure 4.12).
The PLUME formulation, for both PIG and TG, behaves well, showing good agreement with the estimates given by Bindschadler et al. (2011) and Gwyther et al. (2015). On the other hand, the three other parameterizations, largely underestimate or overestimate the total discharge (table 4.3).

Formulations	**PIG**	**TG**
HELMER	300-100 m/yr	70-20 m/yr
PLUME	100-20 m/yr	40-10 m/yr
POLLARD	12-4 m/yr	4-1 m/yr
MARTIN	4-1 m/yr	2-1 m/yr
Estimates		
Rignot	16.2 ± 1 m/yr	10.5 ± 0.7 m/yr
Depoorter	16 ± 2 m/yr	10 ± 2 m/yr
Bindschadler	95-20 m/yr	—
Gwyther	—	50-10 m/yr

Table 4.2: Comparison between measured melt rates for Pine Island/Totten Glacier and the range of melt rates values computed with the four ocean melting formulations. All the formulations melt rate given in table are averages over the 10 yr of the sensitivity experiments. The upper boundary of the range corresponds to melt rates in the grounding line vicinity while the lower value is the melting at the calving front. All the values in table are in m/yr. Rignot et al. (2013), Depoorter et al. (2013), Bindschadler et al. (2011), Gwyther et al. (2014).

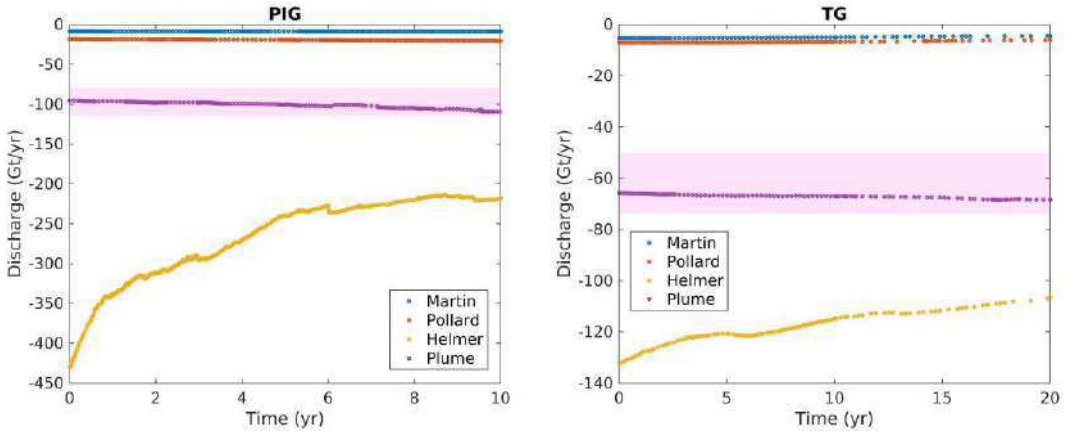

Figure 4.12: *Ice discharge induced by ocean basal melting for Pine Island and Totten Glacier over 10 model years. The pink shaded area represents the observational range from Rignot et al. (2013) and Depoorter et al. (2013).*

All the melt rates in table 4.3 have been computed dividing the total ice discharge by the area times the ice density.
The modelled PIG and TG ice-shelf area are 6197 km^2 and 6112 km^2 respectively,

comparable to the shelves areas used in Rignot et al. 2013 and Depoorter et al. (2013). Rignot et al. (2013) PIG area is 6249 km^2 while TG area is 6032 km^2. Depoorter et al. (2013) PIG area is 6000 km^2 while TG area is 6000 km^2.
As seen from the comparisons in figure 4.12 only the PLUME formulation is able to reproduce correctly both the averaged melt rates and the ice discharge for PIG and TG.

	HELMER	**PLUME**	**POLLARD**	**MARTIN**	**Rignot**	**Depoorter**
Ice discharge (Gt/yr)						
PIG	270	101	20	9	101.2 ± 8	95 ± 14
TG	120	67	7	5	63.2 ± 4	64 ± 12
Melt rate (m/yr)						
PIG	47.5	17.5	3.5	1.5	16.2 ± 1	16 ± 2
TG	21.5	12	1.5	1	10.5 ± 0.7	10 ± 2

Table 4.3: Comparison between simulated and observed ice discharge rates (Gt/yr) and average melt rates (m/yr) for Pine Island/Totten Glacier. Values from Rignot et al. (2013) and Depoorter et al. (2013) are reported for comparison.

4.3.2 Sensitivity to input ocean conditions

In the last section the plume formulation has proved to be the most robust to simulate the correct averaged melt and ice discharge rates. In the present section two sets of modified TS profiles are used to force the plume below PIG (figure 4.8). The first one consists in a perturbation of the TS profile used in the previous sensitivity experiments by a $0.5°C$ increase in temperature in the mid-depth. The second one consists in increasing temperature by $0.5°C$ at higher depths (for both the perturbations, see figure 4.13). The aim of those experiments is to evaluate the response to a warming of equal magnitude but at different location.

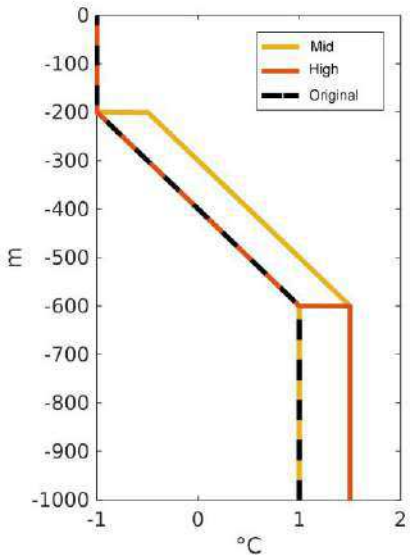

Figure 4.13: *The original TS profile used in experiments presented in section 4.2.3 and the two applied perturbations. Original TS (dotted black), mid-depth perturbation (yellow), higher depths perturbation (red)*

For TG the perturbed profile consists in the warm profile illustrated in figure 4.8 and discussed in section 4.2.1 (figure 4.8).
The impact of a perturbation in ocean conditions immediately affects the melt rate distributions, thus showing that the coupled plume formulation is sensitive to changes in ocean conditions (figures 4.15 and 4.14). For the warm profile, TG shows higher melt rates, a larger backward grounding line migration and an higher ice discharge. Thus, a temperature increase from -1.4 $°C$ to -0.73 $°C$ rises the melt rate at the grounding line from around 40 m/yr to 60 m/yr, and increase the ice discharge of about 30 Gt/yr (figure 4.17).
Regarding the warming perturbation experiments for PIG, for a warming of 0.5 $°C$ at high depths (figure 4.8), the melt rates at the grounding line increase from 100 m/yr to around 150 m/yr, with a corresponding increase of 10 Gt/yr on average. For the temperature increase at intermediate depths, the melt rates rise to 130 m/yr at the grounding line and the ice discharge increases by about $20Gt/yr$, which is larger than warming at higher depths (figure 4.18). For a mid-depth warming the melting values across all the shelf are in general higher. This melting peak is due to the presence of warm water the intermediate depths (figure 4.6 and 4.8). A wider part of the ice-shelf base surface is exposed to higher ocean melting, which increases the discharge. As a consequence the grounding line retreat, is slightly larger for a high depth warming than for a mid-depth warming.

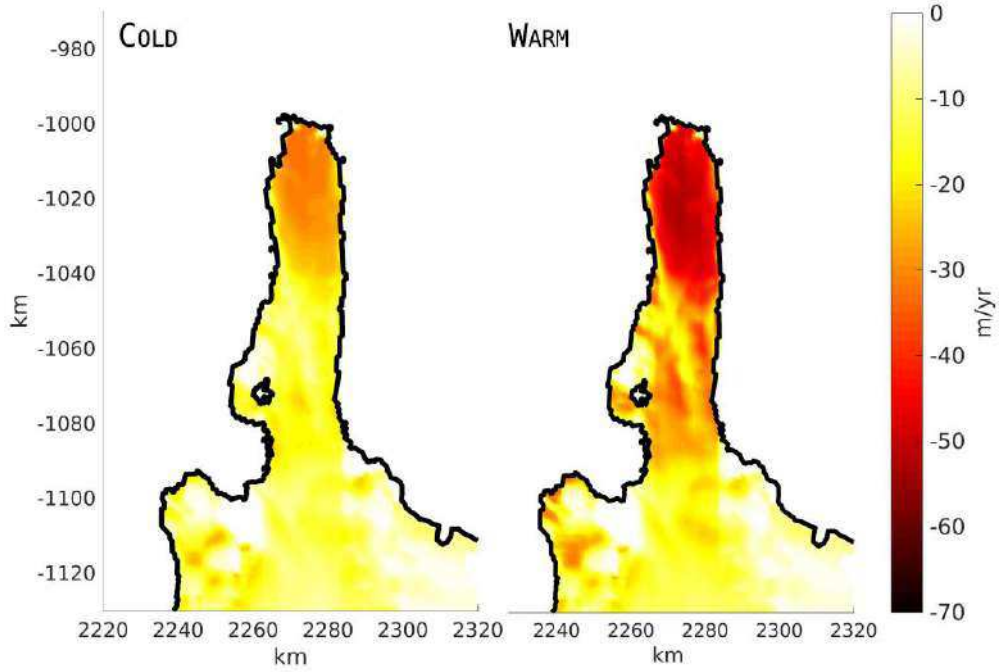

Figure 4.14: *Spatial melting distributions for the perturbed ocean conditions in Totten Glacier. Cold TS profile (left), warm TS profile (right).*

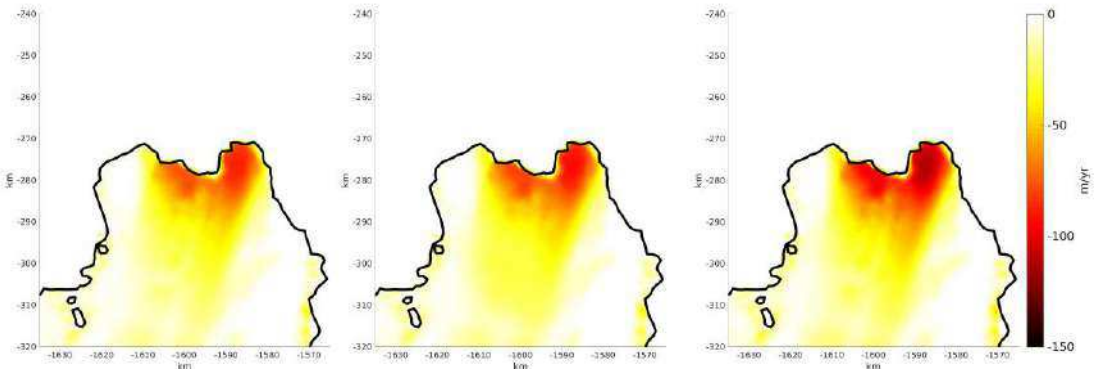

Figure 4.15: *Spatial melting distributions for PIG. From left to right: unperturbed TS profile, mid-depth warming, high-depth warming.*

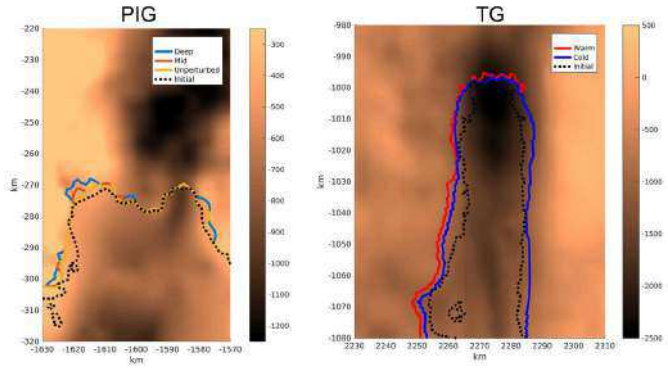

Figure 4.16: *On the left: PIG grounding line migrations comparison for a high and mid-depth warming, grounding line for high-depth warming (blue), grounding line for mid-depth warming (red), initial grounding line (black dotted). On the right: TG grounding line migrations comparison for warm and cold TS profiles, grounding line for warm TS profile (red), grounding line for cold TS profile (blue), initial grounding line (black dotted).*

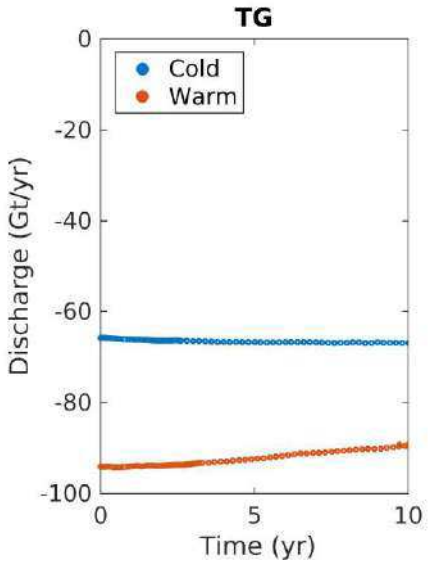

Figure 4.17: *Comparison of simulated rates of ice discharge for the warm and cold TS profile applied to TG*

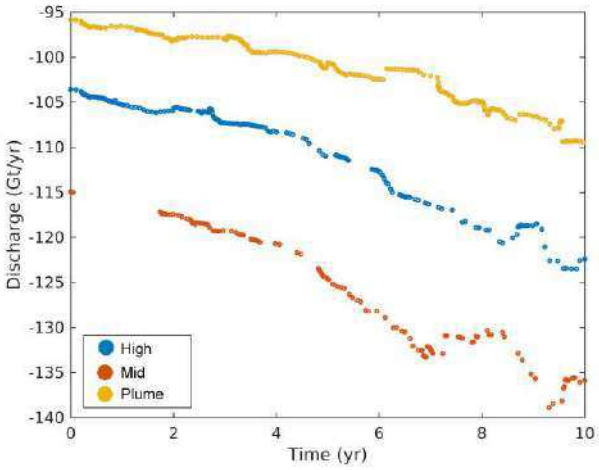

Figure 4.18: *Comparison of simulated rates of ice discharge for an increase in ocean temperature at the mid-depths or at high-depth applied to PIG.*

In addition to the high and mid-depth perturbations applied to PIG, two TS profiles have been extracted from a NEMO (Madec 2015) 1979-2014 hindcast run forced by ERA-INTERIM. Note that this NEMO version does not include the sub-cavity circulation module. The two zones have not been selected in the same area from where the observations (Jacobs et al., 2011) come from. This is because the NEMO bathymetry is not resolved and deep enough in the observation's area to provide TS profiles of adequate depth. Hence, Zone 1 (Z1) and Zone 2 (Z2) have been selected looking at the closer areas to the Pine Island bay (figure 4.19) where the NEMO bathymetry reaches dephts comparable to the observed TS profiles (figure 4.20).
The employed TS vertical profiles are the spatial mean of sixteen vertical profiles averaged over 2009 (2009 corresponds to the same year as in the original observational record by Jacobs et al. (2011)).

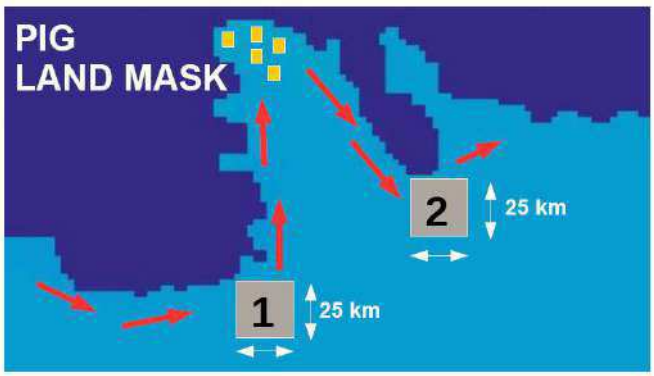

Figure 4.19: *Pine Island Glacier area in NEMO land-sea mask. The observation-based TS profiles (Jenkins et al. (2010)) correspond to the yellow squares. Zone 1 and Zone 2, from where the simulated TS profiles have been extracted, are identified by the two gray boxes, each corresponding to a 625 km^2 area. Each box contains 16 grid nodes and thus as many vertical profiles of temperature and salinity. The red arrows indicate the simplified averaged horizontal ocean circulation.*

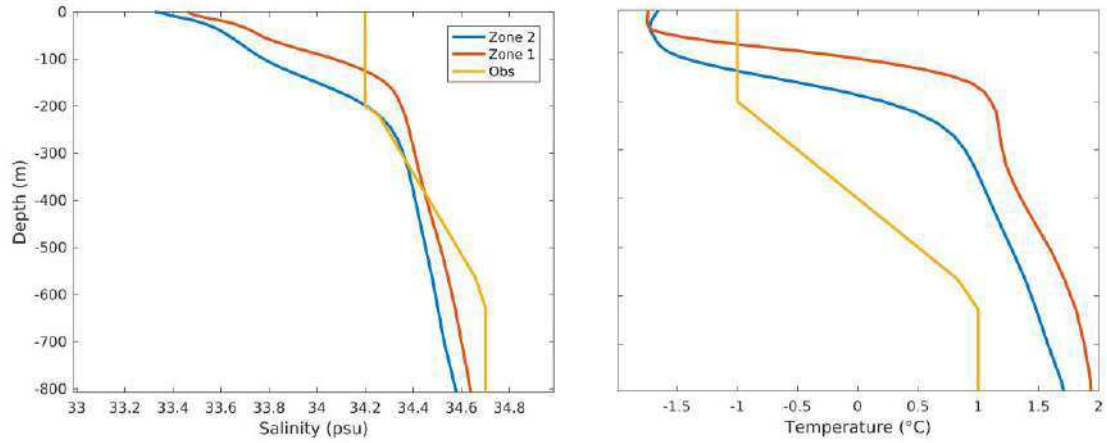

Figure 4.20: *Salinity and temperature from NEMO hindcast simulation compared to the observation based TS profile used in (Jenkins et al., 2010) the melting experiments.*

Both Z1 and Z2 show an ocean temperature $1°C$ higher than in the observations at shallow and high depths and almost $2°C$ higher at intermediate depths, while salinity shows a better agreement with the observation-based TS profile. The difference in temperatures is mainly due to the fact that the two NEMO TS profiles come from a more open-ocean area, where the cooling effect of the shallow continental shelf is not felt.
The use of NEMO TS profiles leads to higher melt rates in the plume under PIG (figure 4.15), increased ice discharge and significative differences in grounding line migration in comparison with the observations. This could suggest that the use of TS vertical profiles, extracted from open ocean areas may overestimate the grounding line retreat. In comparison to the observation-based TS profile, Z1 and Z2 profiles provide a difference in the final grounding line positions of about 7 and 5 km respectively. Also ice discharge drastically increases, being almost the double of the observation-based TS profile (180 Gt/yr against 100 Gt/yr) (figure 4.23).

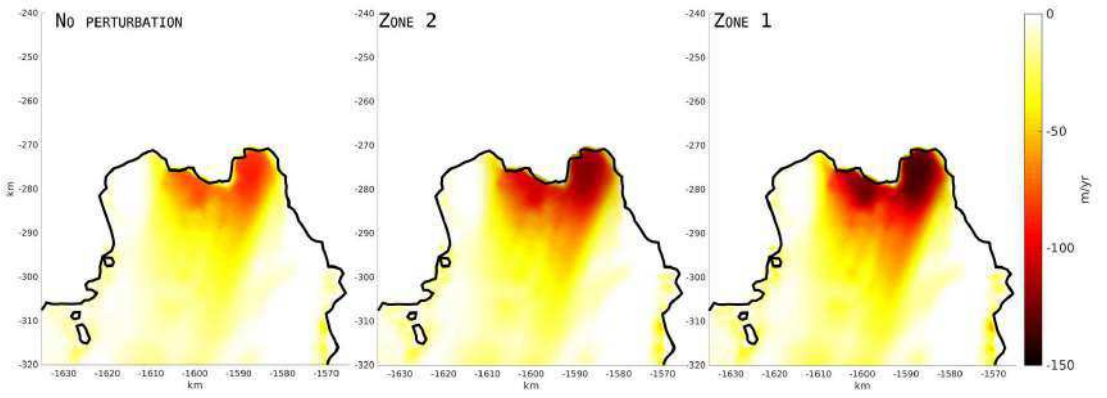

Figure 4.21: *Spatial melting distributions. From left to right: unperturbed TS profile, Zone 2, Zone 1*

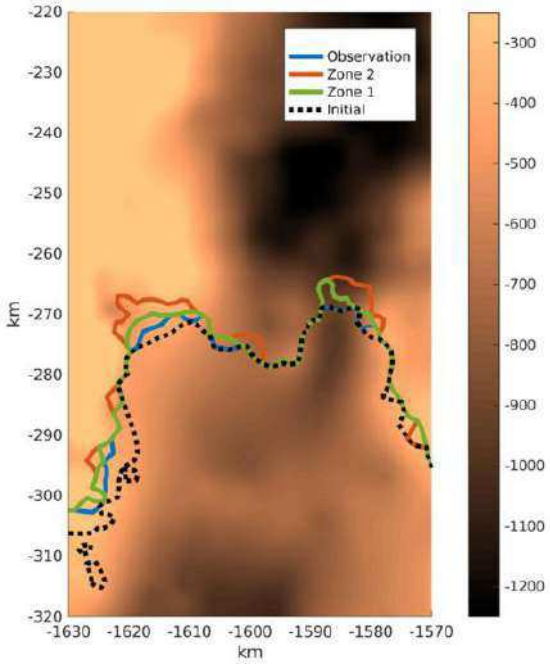

Figure 4.22: *Grounding line migrations due to the use of TS from NEMO hindcast run. Zone 1 grounding line (red), Zone 2 grounding line (green), observation grounding line (blue), initial grounding line (black dotted)*

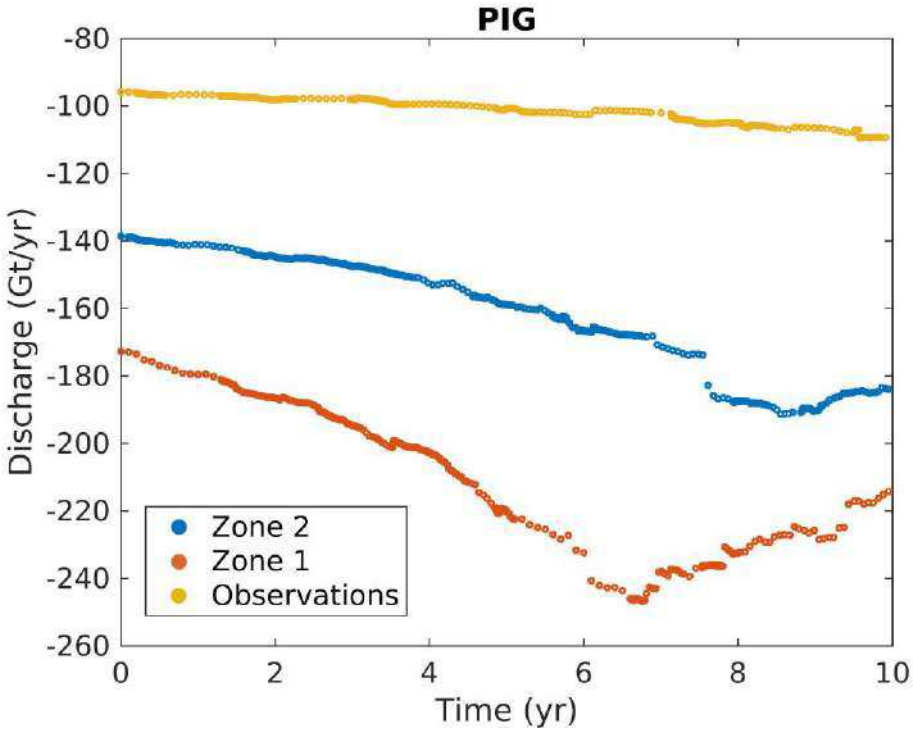

Figure 4.23: *Ice discharge rate comparison for TS profile extracted from NEMO run.*

The same type of experiments with TS profiles extracted from NEMO were run also for TG. The NEMO TS profile was selected where the bathymetry is resolved and deep enough to provide TS profiles of adequate depth (see figure 4.24).

Figure 4.24: *Totten Glacier area in NEMO land-sea mask. The NEMO simulated TS profile has been extracted from the gray box area that corresponds to a 625 km^2 area. The box contains 16 grid nodes and thus as many vertical profiles of temperature and salinity. The red arrows indicate the simplified averaged horizontal ocean circulation.*

The extracted TS NEMO profile is in good agreement with salinity observations while the NEMO temperature profile is way much warmer than the observation profile. From figure 4.25 is evident the temperature difference of almost 3 °C at deep and intermediate depths.

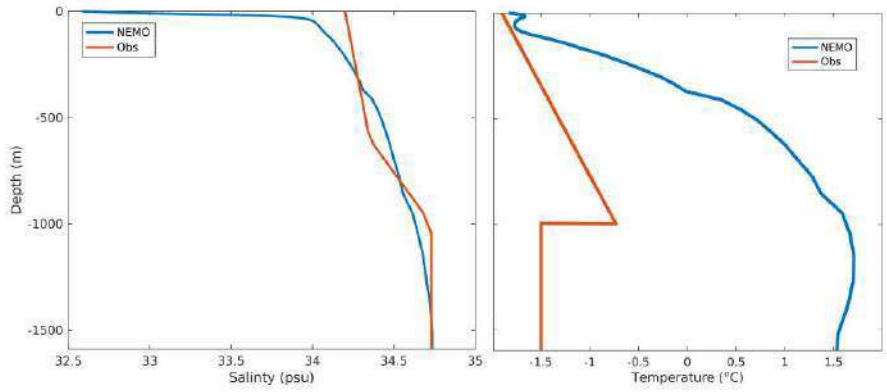

Figure 4.25: *Salinity and temperature from NEMO hindcast simulation compared to the observation based TS profile used in (Rintoul et al., 2016) the melting experiments.*

The employed TS vertical profiles are the spatial mean of sixteen vertical profiles yearly averaged. The use of NEMO TS profile leads to higher melt rates in the plume under TG, increased ice discharge and significative differences in grounding line migration in comparison with the observations (figure 4.14 and figure 4.27). As for PIG this may imply that the use of TS vertical profiles, extracted from open ocean area, may overestimate the grounding line retreat (this issue is adressed in details in the discussion).

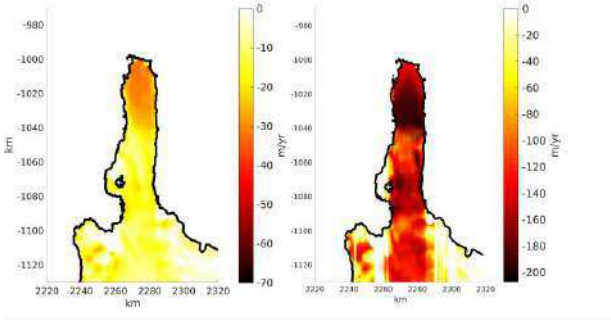

Figure 4.26: *Spatial melting distributions for TG using NEMO TS profiles. Note the different color scale.*

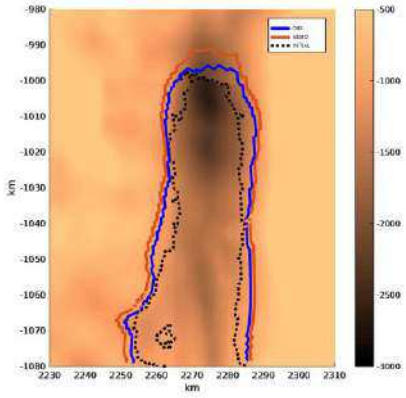

Figure 4.27: *Grounding line migrations due to the use of TS from NEMO hindcast run. NEMO grounding line (red), observation grounding line (blue), initial grounding line (black dotted)*

4.3.3 Application of the plume model to Antarctica

After succesfully testing the plume model on PIG and TG, the impact of the plume formulation and of the three parameterization is tested for the entire AIS. All the AIS simulations are performed with GRISLI at a 15 km resolution and follows Sato and Greve (2012) spin-up procedure (Sato & Greve 2012):

- The present day AIS geometry is relaxed for 100 years, keeping fixed both the grounding line position and the ice shelves. Surface temperature and sea level are representative of present day conditions, while the surface mass balance is set to zero.
- A run of 125 kyrs is performed with the entire topography kept fixed and forced by the air surface temperature of 125 kyrs ago (given the fixed topography the surface mass balance is not influential).
- A transient run of 125 kyrs with the topography kept fixed and with surface air temperature varying between the one of 125 kyrs ago and today. The time dependent temperature anomaly used in this transient run results from the Vostok δD record converted to temperature with the relation of Petit et al. (1999).

The final ice-sheet topography and flow velocities are represented in figure 4.28.

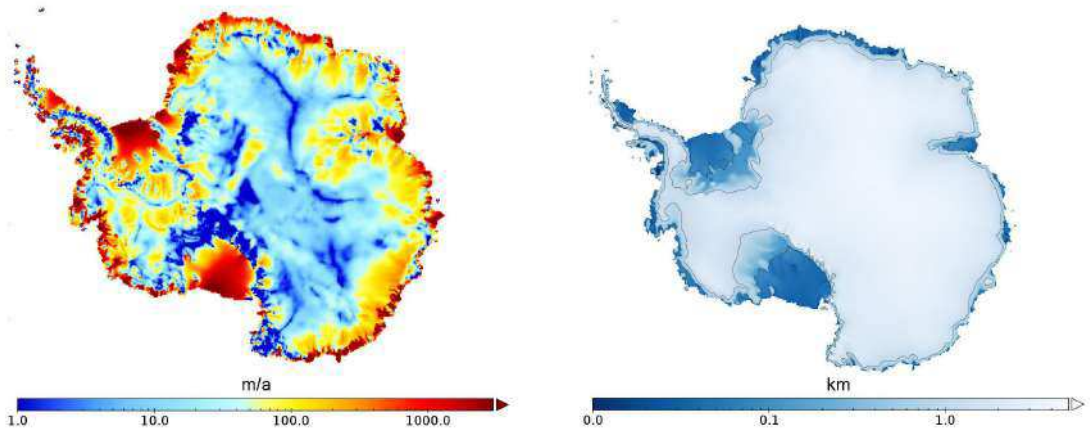

Figure 4.28: *Ice flow velocities and ice topography at the end of the spin up.*

The final spin-up AIS is used as the initial condition for the four 1000 yr experiments using each of the four basal melting formulations.
The prescribed TS ocean conditions for the three larger ice shelves of AIS are summarized in table 4.4.

Ice shelf	T (°C)	S (psu)	Reference
RIS	-1.7	34.8	Jacobs et al. 2002
FRIS	-1.8	34.6	Nicholls et al. 1993
AmIS	-1.9	34.6	Borreguero et al. 2013

Table 4.4: Prescribed temperature and salinity for the three largest ice shelves of the AIS. Filchner-Ronne Ice Shelf (FRIS), Ross Ice Shelf (RIS), Amery Ice Shelf (AmIS).

Figure 4.29 displays the surface topographies at the end of the 100 yrs runs. When using the HELMER formulation, a large part of the Ross, Ronne-Filchner and Amery shelves has collapsed, the glaciers of the Amundsen area exhibit a large retreat. On the contrary when using MARTIN a widespread advance and thickening of all the shelves is simulated. Similar results are obtained using the PLUME and POLLARD formulations except for the Antarctic Peninsula. In this region the PLUME formulation causes almost the entire collapse of the ice shelves.
The differences in simulated surface topographies are related to the different melt rates distribution computed below the ice shelves that, as shown in figure 4.30, differ greatly from each other depending on both the area and the melting formulation considered.
Looking at the entire AIS is instructive to compare the effects that the ocean melting formulations have on the major ice shelves: the Ross shelf (RIS), the Ronne-Filchner shelf (FRIS) and the Amery shelf (AmIS). Table 4.5 reports a comparison between modelled and observed average melt rates for the Ross, Filchner-Ronne and Amery ice shelves.
All the formulations, except HELMER, lead to average melt rates in the range of observations for both the RIS and the FRIS, while for the AmIS both the PLUME and MARTIN formulations do not capture the observed average melt rates. So, for the two larger ice shelves (FRIS and RIS) the choice of the ocean melting formulation has a substantial impact only when using HELMER. In facts the RIS and the FRIS exhibit an almost stationary behaviour except when using the HELMER formulation (figure 4.29).

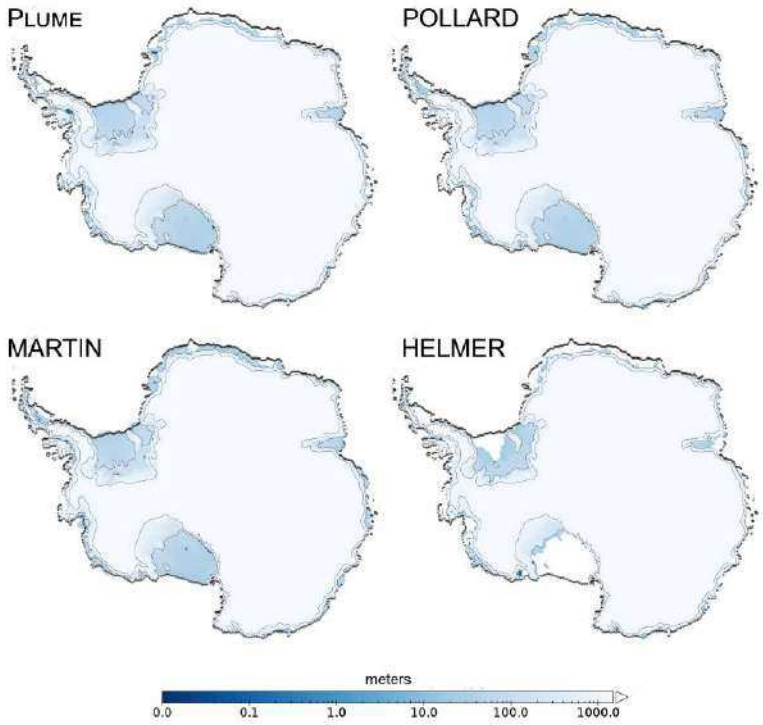

Figure 4.29: *Simulated final ice-sheet topographies at the end of the 100 yr runs using the four ocean basal melting formulations. The black line indicates the ice front of the spin-up topography of figure 4.28*

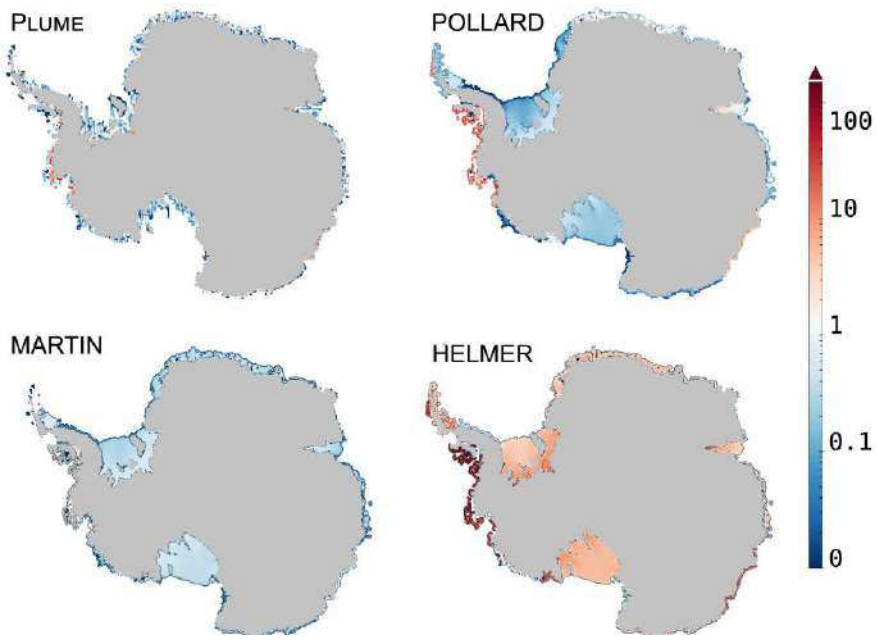

Figure 4.30: *Melt rate distributions over AIS obtained from each of the four ocean basal melting formulations.*

Ice shelf	HELMER	PLUME	POLLARD	MARTIN	Rignot	Depoorter
RIS	4.76	0.20	0.25	0.41	0.3 ± 0.1	0.07 ± 0.05
FRIS	4.70	0.4	0.22	0.35	0.3 ± 0.1	0.12 ± 0.09
AmIS	0.6	0.10	0.2	0.04	0.6 ± 0.4	0.65 ± 0.35

Table 4.5: Comparison between measured and modelled average melt rates for the Ross (RIS), Filchner-Ronne (FRIS) and Amery (AmIS) ice shelves and the range of melt rates values from Rignot et al. (2013), Depoorter et al. (2013).

4.3.4 Impact of ice density on the sensitivity of the grounding line

Generally, when modeling ice flow, the ice density is assumed uniformally equal to 918 kg/m^3 for all the computational domain. Seldom adressed as a major issue in ice sheet modelling, the choice of density is crucial in determining the driving stress. Moreover, assuming constant density is inherently incorrect since, for example, the ice shelf density is in general lower than density of the ice sheet interior due to the presence of fresh snow, firn and compacted snow (Ligtenberg et al. 2011). To test the impact that changes in density have on grounding line migration, five relaxations runs have been performed with the following densities: 830 kg/m^3, 850 kg/m^3, 870 kg/m^3, 900 kg/m^3 and 918 kg/m^3 (from here on the kg/m^3 will be dropped when refering to the related experiment).

The left panel of figure 4.31 shows differences in the initial grounding line positions due to the direct effect that density has on determing the grounding line position. In fact the grounding line is determined through a floatation criterion that depends on both ocean and ice density. Thus, a denser ice shelf will have a more advanced grounding line than a less dense one. For a domain like PIG, the initial position of the grounding line is crucial in defining the evolution of the ice shelf, given the effects that the bedrock morphology below the shelf has on grounding line dynamics. From the right panel of figure 4.31, the impact for the 830 grounding line which migrated back of almost 15 km. The 850, 870 and 918 grounding line final positions, after relaxation, show some advances and retreats but remain in the same positions on the average. The 900 shows the bigger variation in grounding line position, migrating back of around 25 km. To explain this large migration, the main effect on ice flow of using a different ice density needs to be taken into account.

The ice flow driving stress increases for higher density. Thus, although its initial advanced position, higher ice flow velocities combined to a unstable retreating conditions foster a faster grounding line retreat (Figure 4.32).

The effect of density on ice flow velocities can be observed, at the first order, looking at the 850 and 870 velocities. While the grounding line positions are almost the same, the ice flow velocities from the 870 simulation are larger (a peak velocity of almost 4000 m/a against 3000 m/a). The same reasoning can also be applied comparing the velocities for 830 and 900, showing a difference in peak velocities of around 2000 m/a (4000 m/a against 6000 m/a). Thus the choice of ice density has a crucial effect on grounding line evolution that cannot be neglected and needs further investigation. To further test the impact of density on our results, new simulations were performed in which the density is set to 900 kg/m^3 and in which a different ocean melting formulation is used. The grounding line final positions after 10 years is shown in figure 4.33 (as in the melting

experiment of section 4.2.3). The final grounding line positions, for all the ocean melting formulations, differ largely from the ones shown in figure 4.9.

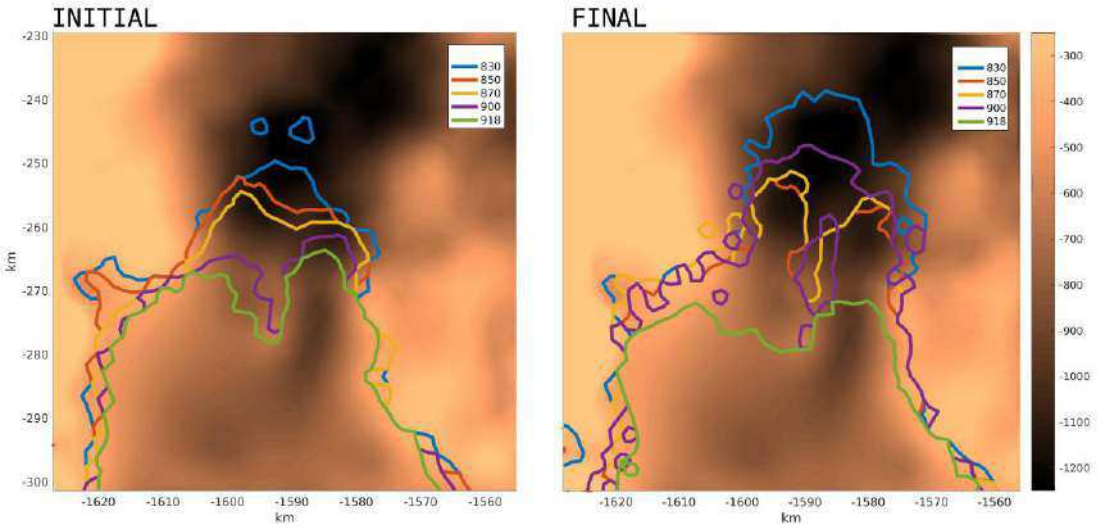

Figure 4.31: *Initial and final grounding line positions for different ice densities: 830 kg/m^3 (blue), 850 kg/m^3 (red), 870 kg/m^3 (yellow), 900 kg/m^3 (purple) and 918 kg/m^3 (green)*

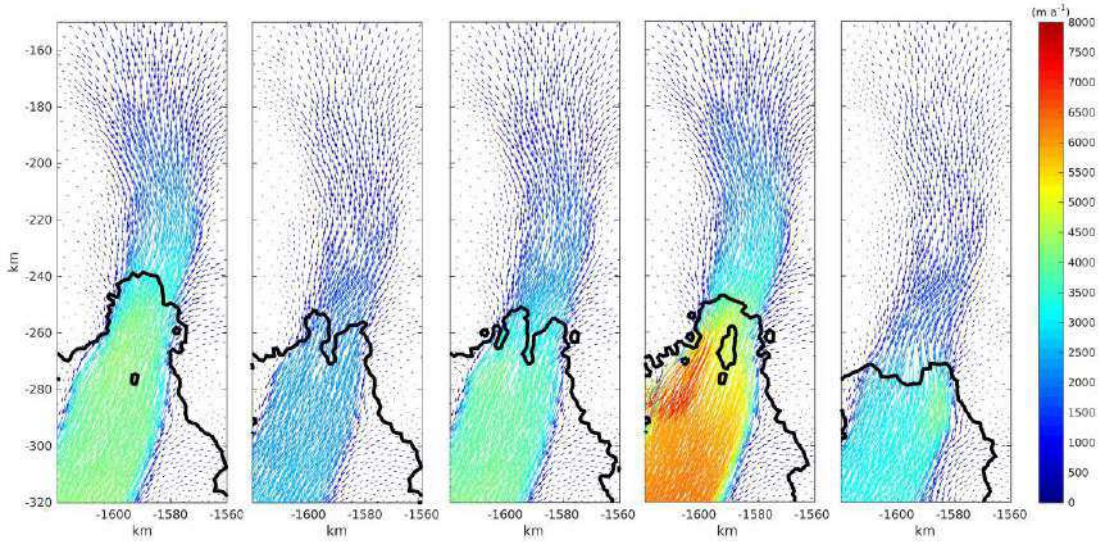

Figure 4.32: *Ice flow velocities. From left to right: 830 kg/m^3, 850 kg/m^3, 870 kg/m^3, 900 kg/m^3 and 918 kg/m^3*

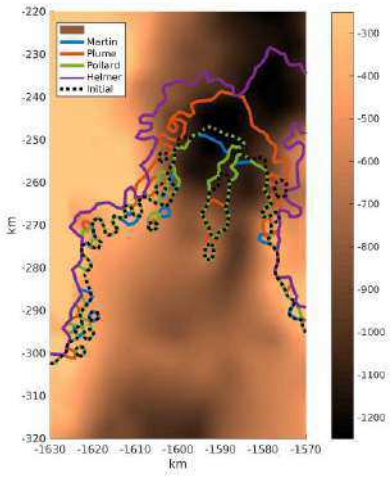

Figure 4.33: *Grounding line migration at the end of the melting experiments for Pine Island Glacier. Initial grounding line (black dotted), PLUME final grounding line (red), POLLARD final grounding line (green), MARTIN final grounding line (blue), HELMER final grounding line (purple)*

4.4 Discussion

This chapter analyzed and discussed the impacts of using different ocean melting formulations on the grounding line dynamics. In addition to three melting parameterizations, for the first time, a 1D plume model coupled runtime with the ice-flow model Úa and GRISLI has been used. The four tested formulations do not converge in terms of grounding line migration, and are not all in agreement with observations in terms of ice discharge and spatial distribution of melt rates. Only the plume model behaves robustly, for both Pine Island and Totten Glaciers.
However, some limitations of the plume model have to be discussed and taken into account in the interpretation of those simulations. The first caveat is that, in general, plume models neglect bathymetric effects, because the water in the layer below the ISW layer is considered to be still and because the forcing by the ocean is induced only by the ISW layer. This clearly prevents the plume from realistically representing the ocean circulation inside the ice-shelf cavity. Moreover, in the case of a 1D plume model, the Coriolis effect is not accounted for. Thus the path of the plume, as stated in Holland and Feltham (2006), has to be prescribed. In general the main effect of Coriolis is to deviate the plume along a direction that is typically parallel to the isobaths at the ice-shelf base. Thus a plume of Ice Shelf Water, deviated by the Coriolis effect, will entrain less and will rise slower than our 1D plume (Holland & Feltham 2006, Holland et al. 2007). To compensate, the entrainment factor of the 1D plume model is set to half its value (see equation 2.29) but, in general, the lack of Coriolis effect impacts the spatial melt rate distribution. The latter is true especially far from the grounding line. Therefore, assuming the path of the plume to be perpendicular from the grounding line to the ice shelf front, causes discrepancie with respect to the observed melt rates spatial distribution. Moreover, the implementation of the plume prescribes that when the ISW detaches the melt rate is set to zero. This choice was considered the most logical, instead of prescribing an artefact value. In figure 4.34, the melt rates distributions for the Amery and the

Filchner Ronne Ice Shelves are compared with observations. In figure 4.34, the melt rate is computed by the plume formulation coupled to GRISLI at 15 km of resolution (as in section 4.3.3). The plume formulation captures the melt rates distribution in the grounding line vicinity but fails at reproducing the observed distribution far from the grounding line. In particular, under the Filcher-Ronne ice shelf, the plume detached from about the ice shelf center. This also holds true for the Amery ice shelf, although the melt rate spatial distribution is better captured by the plume.

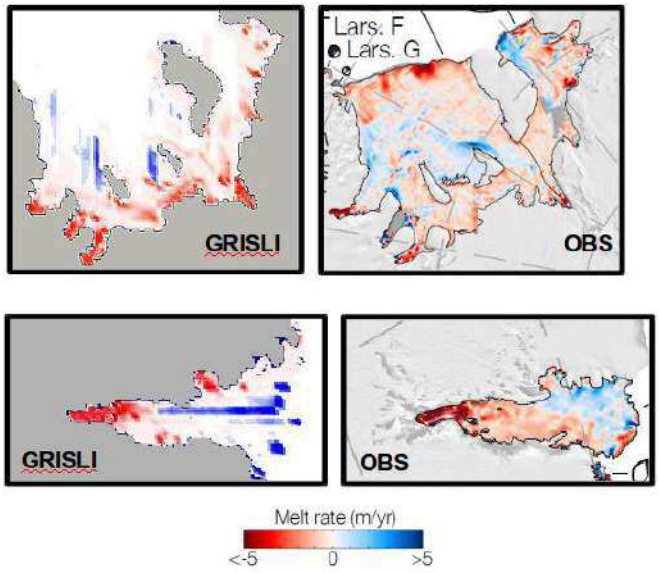

Figure 4.34: *Comparison between the spatial melt rate distributions simulated by the plume formulation coupled to GRISLI and the observations from Rignot et al. (2013). Upper panel: Filcher-Ronne ice shelf. Bottom panel: Amery ice shelf.*

The reason is that in wider shelf, where large horizontal circulations impacts on the melting distribution, the plume fails to correctly reproduce the observations due to the absence of the Coriolis deviation. However, in narrow ice shelves (such as TG, PIG and also the Amery ice shelf), the impacts of the horizontal ocean circulations is limited and thus, the melt rates simulated with the PLUME depends mainly on the ice shelf basal morphology.
However, in terms of ice shelf evolution, the interest is generally focused on what is happening in proximity of the grounding line, where the Coriolis force is not strong enough to overcome friction and to deviate the ISW plume. Moreover, for ice shelves (as TG and PIG) in which the width to length ratio is low, the errors in the melt rate distribution due to the lack of a Coriolis deviation is smaller than in the case of very large ice shelf (such as the Ross Shelf, where a large horizontal shelf circulation takes place). Anyhow, as shown in section 4.3.3, the modelled PLUME average melt rates simulates for the larger ice shelves (RIS, FRIS and AmIS) fall in the uncertainty ranges of the observations. This confirms the absolute importance, for an ocean melting formulation, to be able to primarily reproduce the correct melt rates in the grounding line vicinity.
Nevertheless, as shown by the perturbation experiments of TG and PIG, an uncertainty in the ocean conditions drastically affects the magnitude of the simulated melt rates and ice discharge. In Lane Seriff (1993) it is in fact demonstrated that ambient

water properties are the most influential input parameters in a plume model, with ambient temperature being the primary control on the distribution of melting and freezing (Lane-Serff et al. 1993). Jenkins (1991) tested the sensitivity of the plume model to modifications of the ambient ocean conditions, showing that the melting and freezing distribution is primarily sensitive to variation in temperature, but almost insensitive to the absolute ambient salinity. However, the gradient in ambient salinity drives the plume density that, in the end, controls where the ISW plume loses buoyancy (Jenkins & Bombosch 1995). In addition to being controlled by salinity, the plume density is also influenced by the presence of frazil ice. The formation of frazil ice is not accounted for in the coupled plume model and this may overestimate or underestimate the distance from the grounding line at which the plume actually detaches (Jenkins et al, 2014).
However, apart from the numerical implementation and the inherently limitations of the coupled 1D plume model, both the ocean melt distribution and the ice discharge rates are in good agreement with observations, making the plume model the best formulation available among the ones tested in this Ph.D. for PIG and TG. The PLUME behaves well also for the larger ice shelves, as also the MARTIN and the POLLARD formulation.
As outlined in the introductory section of this chapter, most of the parameterization are usually tuned on observed ocean melt rates. The tuning is typically performed by the introduction of multipling coefficients such as the F_{melt} in Martin et al. (2011) or the K_{shelf} in Pollard and DeConto (2012). In the case of MARTIN, the use of a fixed coefficient gives melt rates that are valid only in certain areas of the AIS (FRIS, RIS), while in other zones the melting is too low (PIG, TG). On the other hand, the use of an area-dependent parameter as in POLLARD, provides variable melt rates comparable to the average observed melt rates given by Rignot et al. (2013) and Depoorter et al. (2013). The real issue with this tuning method is related to the following question: will the tuning be still valid if the ocean conditions vary significantly, as in the remote past or in the quasi-near warming future? Will it be possible to correctly reconstruct or predict the past or future extension of ice shelves? There is clearly not a conclusive anwser but surely, avoiding the introduction of an area-dependent tuning parameter, will make any numerical experiment more robust. Precisely for this reason the plume model should be preferred to the other three formulations. In the 1D plume the link between the ocean conditions and computed melt rates is given by robust physical equations and is thus always valid in space and time.
Both in section 4.3.3 and in the above discussion has been said that the POLLARD formulation gives a melt rates range similar to average melt rates from Depoorter et al. (2013) and Rignot et al., (2013). However, as shown in table 4.2, the POLLARD formulation applied to PIG and TG does not return the correct ice discharge and area-averaged melting.
Two key things emerge:

- The real quantity of interest from the observational papers (Rignot et al. (2013) and Depoorter et al. (2013)) is the ice discharge due to basal melting and not the area-averaged melt rate.

- A robust ocean basal melting formulation should be primarily able to simulate the correct ice discharge rate and the spatial melting distribution, since the melting

rates at the grounding line heavily impacts the ice shelf evolution.

A clear example of the importance of correctly simulating the melt rate distribution is given in figure 4.35, showing a comparison between a run using the plume formulation and a run forced by a spatial uniform melt rate (called AVG from here on and equal to the average melt rate for PLUME in table 4.3). The lack of a realistic distribution is immediately evident, the AVG grounding line advances while the PLUME grounding line retreats.

In this chapter there are no claims about considering the simulated grounding line positions for PIG and TG as estimates for the future, since (1) no validation of the initial grounding line has been made through a comparison with observations, (2) because the calving front has been kept fixed in all the Ua experiments and (3) also the surface mass balance has been kept fixed troughout all the simulations (future projections for surface mass balance predict an increase and thus a positive contribute to ice-shelf mass balance (Ligtenberg et al., 2013)). The ability to reproduce the correct grounding line migration is of crucial importance in ice dynamics but, how the grounding line evolve is not related only to the ocean forcing but also to the simulated dynamics in the ice flow model.

Given that the purpose of this thesis was to compare the impacts of ocean formulations, the magnitude of the grounding line migrations are interesting just from qualitative point of view. Thus no attention should be paid to the absolute values of migration. However, correctly reproducing the grounding line migrations of the last decades would represent the next step in improving the coupling of the plume with an ice-sheet model. This problem will be the object of future works.

Another caveat is that reproducing and simulating correctly the grounding line migration, is complicated by the fact that reasonable ice density variations within the ice-sheet models drastically affect the initial and final grounding line positions. The fact that density has an impact on the floatation criterion and on the driving stressed is a known fact from the basic theory of ice dynamics. However, to make reliable projections for the future, the appropriate and the most reliable 2D density field should be employed. Figure 4.36 shows a density field for the PIG drainage basin obtained following Ligtenberg et al. (2011). This density field was already in Úa, implemented by Hilmar Gudmundsson and used in Favier et al. (2014). Based on this density distribution, it is clear that a uniform density value is not representative of reality and that this could lead to overestimates or underestimates of grounding line position and driving stresses. This is illustrated by the final grounding line positions obtained using the 2D density distribution for a relaxation run in Ua (figure 4.37). The final grounding line positions are largely different from both the 918 kg/m^3 and the 900 kg/m^3 cases, confirming the need for a more accurate treatment of ice density in ice-sheet models.

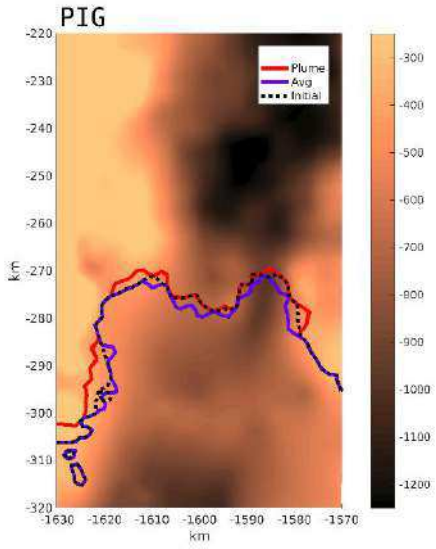

Figure 4.35: *Comparison of grounding line migration applying the PLUME formulation or the uniform AVG melt rate distribution for Pine Island Glacier.*

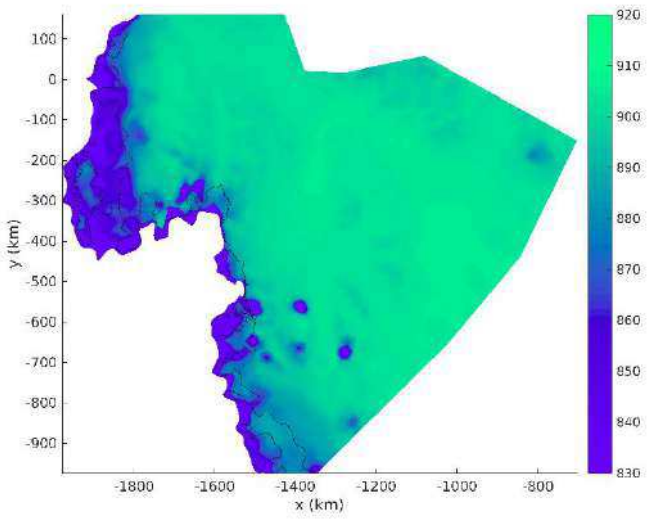

Figure 4.36: *Density field for the Pine Island Glacier drainage basin, obtained after Ligtenberg et al, 2011.*

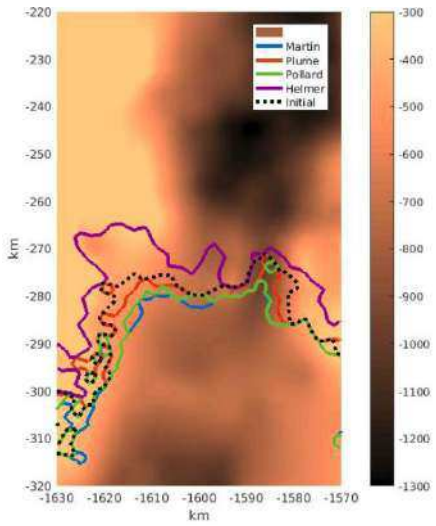

Figure 4.37: *Final grounding line positions for the four ocean melting formulations using the firn correction 2D density in the simulation. (to be compared with 4.9)*

.

Discussion and conclusion

In this thesis we investigated the ocean basal melting of ice shelves both in a conceptual and in a realistic framework by means of numerical modelling. The main focus was: (1) the interplay between calving and ocean basal melting in driving grounding line dynamics (2) on the impacts of different ocean basal melting formulations on the grounding line migration, the ice discharge and the basal melt rate for two melting hotspots of the AIS (Pine Island and Totten Glacier). The novelty of this work consists in the developing and in the online coupling of a 1D plume model (Jenkins, 1991) to the employed ice-sheet models. The impacts of this dynamical melting formulation, along with the three usally employed melting parameterizations (Helmer and Olbers, 1989; Martin et al., 2011; Pollard and DeConto, 2012), have been evaluated on both regional areas of Antarctica (Pine Island Glacier and Totten Glacier) and on the entire Antarctic Ice Sheet.
The major achievements of this Ph.D. can be summarized as follows:

- an ice-sheet-shelf system is more sensitive to the impacts of ocean basal melting under cold climate conditions than under warm climate conditions.
- ocean basal melting influences the occurence of the calving process that, in turn, boosts or damps the grounding line migration. This boosting/damping effect is a function of the underlying bedrock morphology and of the ice-shelf width.
- the choice of an ocean basal melting formulation has a large impact on the amplitude of simulated grounding line migration, ice discharge and melt rate distribution for the Pine Island and Totten Glacier areas (and also for the entire AIS). For the same forcing ocean conditions, the obtained melt rates and ice discharge rates do not converge to a common value.
- the 1D plume is the only formulation able to capture the proper observed melt rates and ice discharge values for both Pine Island Glacier and Totten Glacier. Applied to the entire AIS, the larger ice shelves of Antarctica (Filcher-Ronne, Ross and Amery Ice Shelf) exhibit a minor sensitivity to the choice of a melting formulation.

The initial hypothesis implications, limitations of those results as well as of the methods that I used to perform this Ph.D. are discussed in the following section.

5.1 Discussion

On Ice-Sheet Models The ice sheet models used in this thesis are both able to solve the SSA/SIA for ice flow. In particular: GRISLI has been run in hybrid mode (both SSA/SIA active) while Úa has run with only the SSA active. Úa run only with the SSA active (as in Favier et al.,2014), because PIG and TG are mainly constituted by ice-streams and ice-shelves, for which the SSA approximation is preferred to SIA.On the other hand, although Úa has performed well in the MISMIP experiments, the fact of runnig the simulations with the SSA only raises some issues that need to be discussed. As shown in Favier et al. (2014), Úa shows a faster grounding line retreat for Pine Island Glacier in comparison to full stokes and higher order models (ELMER and BISICLES

respectively). This was partly explained by the choice of the model parameters, and partly by the exclusive use of the SSA. Pattyn et al. (2013) compare different models run in an idealized framework and results indicate that the SSA models generally react much faster to a given external perturbation and that grounding lines reach their equilibrium position after about 30 years, against 80 years for models including vertical shears.
Although the horizontal stress gradients have a large control on the grounding line evolution, vertical shearing at the grounding line also plays a crucial role. An increase in shear stresses contributes in lowering the effective viscosity, thus influencing the ice velocities and thus causing changes in ice sheet volume and geometry.
In the case of the experiments performed in this thesis, the main impact of using the SSA is on the velocity of ice-shelves retreat, not on the final positions.
GRISLI runs have been carried out in hybrid mode (both SSA/SIA). The possible limitations of GRISLI in tracking grounding line migration have already been discussed in chapter 3. Although an hybrid model does not represent the best choice for tracking grounding line migrations, the interest of chapter 3 was in testing a model like the ones used for paleo/future simulations, therefore the only potential alternative was to choose one of the hybrid models that make use of the flux corrections at the grounding line.
For the experiments discussed in chapters 3 and 4, a full-Stokes model could have overcome those limitations. On the other and, these kind of models are highly computationally demanding. In fact, for the simulations carried out for chapter 4, it would not have been possible within the timeframe of the Ph.D., while for the ones presented in chapter 3, it would have not be feasible with the present computational possibilities. In addition, given the grounding-line-resolving characteristic of Úa, the use of a full-Stokes model would have probably not add anything significant to the results.
To overcome these SSA/SIA limitations and the large computational cost of full-Stokes physics, the ice-sheet-modelling community is focusing in developing multi-physics ice dynamics models (ISCAL, by Ahlkrona et al. 2016; RIMBAY by Thoma et al. 2014; ELMER-ICE under development at LGGE). These models include both SIA/SSA and Full-Stokes physics and are able to apply the necessary approximations only where needed.

On plume model I adressed the main limitations of the coupled 1D plume model in discussing chapter 4. However, as pointed out in chapter 4, the lack of the Coriolis effect is one of the major weakness of the plume and needs to be discussed in details.
In this thesis the one-dimensional plume model is coupled in two dimensions by using simultaneously a set of plumes rising straight from the grounding line to the ice-shelf front and not interacting with each others. The assumption of chosing the plume path beforehand has a particular importance, considering that a plume under the influence of the Coriolis deviation would actually be deflected and would rise primarily parallel to isobaths. As a consequence, an ISW plume would travel slower and would not become supercooled unless steered upslope by ice-shelf-base obstacles. This has been shown by Holland and Feltham (2006), who extended the 1D formulation to two dimensions. In particular their 2D plume banked up and became a narrow boundary current, slowed down by the drag at the domain border. Their model allowed treatment of both transient and turbulent horizontal diffusion but the increase from one to two dimensions led

to a significant increase in computational cost. Further, Holland et al. (2007), using the same 2D plume model, attempted to simulate the marine ice distribution beneath the FRIS. They were successful in regions where multiple plumes joined together and fed the ISW. The 1D plume formulation developed for this thesis is clearly not able to reproduce the merging of plumes as in Holland et al. (2007), given the neglect of the Coriolis deviation. Thus the prescribed straight plume's paths may lead to unrealistic melt rates far from the grounding line or in the area where, due to the Coriolis effect, the plumes would merge.
Moreover, also the frazil marine ice formation was not taken into account. This process has a big role in the sub-ice-shelf ocean dynamics, mainly because the presence of suspended ice crystals makes the ISW plume more buoyant. Thus frazil ice formation modifies the forcing on the overturning circulation, which in turns, influences where the ISW plume rises and detaches. As a consequence, the neglect of this process in the plume model may lead to incorrectly simulating the point from which the ISW plume detaches.

On ocean basal melting Several AIS paleo reconstructions/future simulations (Huybrechts and de Wolde, 1999; Pollard and DeConto, 2009; Greve et al., 2011; Martin et al., 2011; Ritz et al., 2015; Pollard and DeConto, 2016), using the simple depth-dependent parameterization for melting presented in section 2.2, have been published in the last years. Altough, as shown in section 4.3.3 the impacts of the three ocean melting formulations considered for the analysis (with the exception of HELMER) do not largely affect the evolution of the major ice shelves at Antarctic scale, this is not the case when applying them to specific glaciers, such as PIG and TG glaciers. However, although these two glaciers are small, their large inland drainage basins have a large potential contribution to future sea level changes.
When simulating the entire AIS at coarse horizontal resolutions typically used (15 km to 40 km), the ice sheet models cannot capture the outlets of smaller shelves or glaciers as PIG and TG whose drainage basin is however large and dynamically important to monitor the overall state of part of the AIS. Therefore, at coarse resolution, a physically-based formulation might not be usefull if the glaciers/ice-shelves systems are not properly captured. However, as shown in chapter 3, an ice-sheet-shelf system under a cold climate conditions (glacial periods), is more sensitive to ocean basal melting due to lower ice velocities. Thus, in order to properly simulate the fluctuation between glacial and interglacial states of an ice sheet, it is necessary to provide the correct ocean forcing, given the high sensitivity of a cold ice sheet to melting by the ocean.
Consequently, given the fact that ice-sheet models should be able to simulate correctly the main ice flow of the AIS, it is clear why a robust ocean melting formulation should be preferred and employed. However, also an improvement in the computational resources, with the aim of obtain higher resolutions, is fundamental.
Furthermore, the forcing ocean conditions (temperature and salinity) for the plume or other formulation remains an issue. The temperature and the salinity provided to the ocean formulations should be as close as possible to observations. However, temperature and salinity records in the sub-ice-shelf cavities are still too sparse to provide satisfactory forcing and comparison data sets. Thus it can be argued that a temperature and salinity 3D-field, obtained from a validated ocean model, would represent a better choice

than using few observed vertical profiles of temperature and salinity. In addition, from the perspective of paleo and future simulations, the forcing conditions will always be model-based. Thus, given the absence of widespread observations and the need for future and past ocean conditions, the use of ocean numerical models is fundamental. On the other hand, as shown in section 4.3.2, the use of modelled vertical profiles taken from far open ocean conditions may lead to wrong estimates of ice-shelf melting and ice discharge into the ocean. Anyhow, in the last years, ocean models have become able to simulate the ocean circulation below shelves cavities. The capability of simulating the circulation is now present in well-establisehd ocean models (NEMO, MitGCM, ROMS) and this has provided realistic simulations of ocean properties, circulation and basal melting (Mathiot et al. 2017). From this perspective, extracting vertical temperature and salinity profiles from this sub-shelf-cavity-circulation resolving models may provide more consistent results than the one shown in section 4.3.2. However, the fact the sub-shelf processes are better simulated do not directly imply that also the modelled ocean temperature and salinity will improve with respect to observations. The advent of the capability of resolving the circulation below the ice-shelves has opened new perspective in modelling ice-ocean interaction.
The cutting edge frontier in modeling ice-ocean interactions is the ice-sheet-ocean coupling. Many of the published studies (Sergienko, 2013; Kimura et al., 2013) deal with idealized shelf geometries and are usually not run in three dimensions. Moreover the coupling is yet performed offline by asynchronously exchanging models outputs (Goldberg et al., 2012; De Rydt and Gudmundsson, 2016), given the difficulties of ocean models to deal with a moving ice shelf geometry.

On calving Liu et al. (2015) shows how ocean basal melting and icebergs calving are tightly related (Liu et al. 2015). This is confirmed also from the conceptual simulations of chapter 3, where the occurence of calving boosts the melting-driven retreat of the grounding line. As outlined in section 3.4 the calving occurence in an ice-sheet simulation is largely model dependent, given the wide variety of existing calving formulations. The calving parameterization in GRISLI is based both on thickness at the ice shelf front and on the lagrangian scheme presented in chapter 2. Thus, GRISLI checks not only the ice thickness, but also if the upstream ice fluxes are able or not to mechanically sustain the stability or the expansion of the ice shelf. In a simpler approach, thickness criterion could be used, at the first order without any check on the fluxes at the grounding line, as representative of calving occurence. In fact, a thinner ice shelf is considered to be more prone to calving than a thicker one. So, even the use of a more physically-based criterion for calving (such as Timmerman et al., 2011;Albrecht et al., 2011; Christmann et al.,2016), should in principle not contradict the assumption that a thinner ice shelf is more prone to calving.
However, although assuming that a thinner ice shelf would undergo calving easier than a thinner one is correct, the use of a thickness-based formulation for calving could lead to unstable behaviour in the models as shown in figure 5.1.
As illustrated in chapter 3, for a more severe thickness threshold (H_{coup}=200 m) and for a stronger ocean melting (group G and H), the grounding lines retreat is larger than with a moderate calving threshold. Here the retreat started by ocean basal melting is boosted

by the calving process. On a prograde bedrock, as the grounding line migrates back, the ice thickness decreases. Thus if the calving thickness criterion is verified at the ice shelf front, it will be verified again for successive retreats. From this perspective the calving process may be misinterpret as a mechanism able to turn on positive feedback of retreat. However, this "ice calving instability" is a product of the numerical implementation.
Similarly to this mechanism Pollard and DeConto, (2015) introduced the so-called "Ice cliff Instability", a physical process involving the mechanical collapse of ice cliffs in places where marine-terminating ice margins approach 1 km in thickness with 90m of vertical exposure above sea level. This subaerial cliff faces are thought to collapse because of the longitudinal stresses exceeding the yield strengths of the ice. This process has been extensively used in Pollard and DeConto (2016) to reproduce the paleo-dynamics of the AIS, although there is no extensive literature about observations of this process. In Pollard and DeConto (2016), when the height of the ice cliff exceeds a certain threshold, the ice sheet grid point is cut. However, this proposed instability mechanism could be highly related to its numerical implementation. In analogy with the thickness-based calving formulation, but in the case of a retrogade sloping bedrock, if the criteria for ice cliff instability is verified in a downstream position it will be verified also in all upstream positions (on a retrogade slope, as the grounding line retreats, the ice thickness increases). This leads to an unstable retreat but, as in the case of calving for a prograde slope, is largely due to the numerics of how the process has been implemented.
However, this discussion on thickness-based processes formulations do not affect the results shown in chapter 3, since the objective was only to force the experiments with two calving magnitudes. In addition, as already discusses in chapter 3, the thinning induced by ocean melting really foster the calving of icebergs, thus not contradicting the assumption that a thin ice shelf is more prone to calving with respect to a thick one.

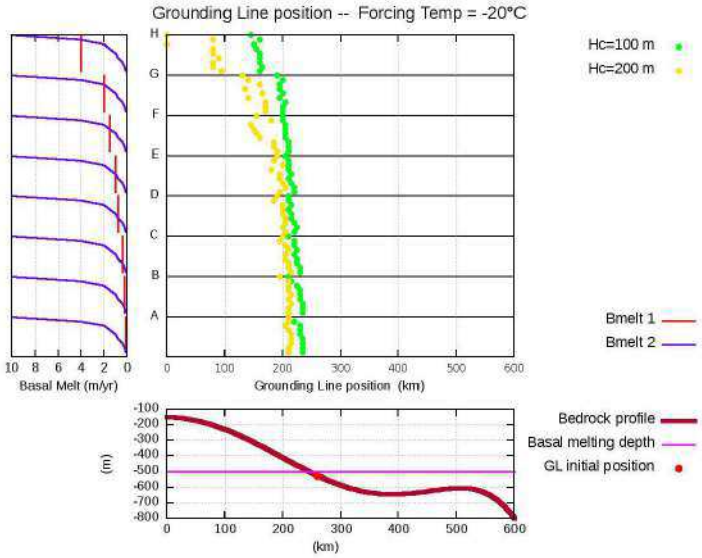

Figure 5.1: *Grounding line migrations for B101 spinup shelf (chapter 3) as a function of the H_{coup} thickness criterion and of ocean basal melting. The bottom panel displays the bedrock profile with the initial position of the grounding line (red dot) and the selected ocean melting depth limit (purple line). The left panel shows the basal melting groups: going up from group A to group H the total basal melting increases because of higher bmelt1 values (red line). Bmelt2 is denoted by a blue line. Each dot in the central panel represents the final grounding line position of each melting experiment. Depending on the prescribed H_{coup} value the color of the dot is different (yellow for H_{coup} = 200 and green for H_{coup} = 100). The positive feedback between ocean melting induced thinning and calving of grounding line retreat is obvious in group G and H.*

5.2 Conclusions and future works

In this thesis I have shown how crucial is the choice of an ocean melting formulation and the importance of using a physically based ocean melting treatment. The coupled 1D plume developed for this thesis represents a useful modelling tool to simulate the current, past and future Antarctic Ice Sheet dynamics. In addition to correctly reproducing the current observed melt rate patterns and magnitude, the PLUME model is also computationally fast, and thus usable for long term simulations.
The next step, after this thesis, will be to estimate the future contributions of freshwater to the ocean starting from the PIG and TG and extends the approach to other relevant regions (e.g. Twaithes Glacier).
To produce valid and robust projections for the future some improvements in the methodology employed in this thesis are needed, for example:

- a calibration and validation with observations of the initial grounding line position, in order to perform simulations consistent with observations. This is especially needed given the importance that the initial grounding line position have in the ice shelf evolution, as is the case for PIG (see section 4.3.4).
- although we have developed and coupled a physical formulation for ocean basal melting, the calving process and the evolution of surface mass balance were not accounted for. As the occurence of calving and variation of surface mass balance directly impact the evolution of the grounding line and of the ice flow from the

interior, this processes has to be taken into account in future projections.

- BEDMAP2 bedrock bathymetry (Fretwell et al., 2013) was used as boundary condition in all the simulations . However, although BEDMAP2 represents the state-of-the-art dataset for AIS modelling, there are some works that has provided refined bathymetry for several key areas of Antarctica (Timmerman, 2010; Schaffer, 2016). The ice-sheet models should run different available bedrock bathymetries (Davis et al. 2017; Greenbaum et al., 2015; Aitken et al., 2016; Timmerman et al., 2011; Heimbach et al, 2012), given the importance that the underlying bedrock morphology has on grounding line dynamics (Sun et al. 2014 Gasson et al., 2015).
- as discussed in the last section, the ocean forcing is the key aspect to improve marine-ice-sheet simulations. Given the recent disposability of sub-shelf-cavity-circulation resolving models, the main and the natural follow-up of this thesis is the ice-sheets-ocean model coupling. In fact, an ice-sheets-ocean coupled model would really represent an advance in the simulation and understanding of the future and past state of the AIS and of its contribution to climate.
- Pattyn et al. (2013) illustrate how the choice of the approximation of the Stokes equations is crucial for consistent short-term predictions of ice sheet evolution. This needs to be taken into account when simulating the near-future of the AIS, and thus the use of higher-order equations models should become more systematic to study topic involving the grounding line dynamics.

A.1 Acronyms and constants

Symbol	Description	Units	Value
ρ	Ice density.	kg/m^3	830 - 917
ρ_w	Ocean water density.	kg/m^3	1000 - 1030
g	Acceleration of gravity.	m/s^2	9.81
$\mathbf{u}$	Ice velocity.	m/yr	-
$\mathbf{u}_b$	Basal ice velocity.	m/yr	-
s	Surface topography.	m	-
b	Bedrock elevation.	m	-
h	Ice thickness.	m	-
α	Thermal expansion coefficient	$^\circ C^{-1}$	$3.87 \cdot 10^{-5}$
β	Saline contraction coefficient	psu^{-1}	$7.86 \cdot 10^{-4}$
a_0	Sea water state equation parameter.	$^\circ C$	$9.01 \cdot 10^{-2}$
b_0	Sea water state equation parameter.	$^\circ C/psu$	$-5.73 \cdot 10^{-2}$
c_0	Sea water state equation parameter.	$^\circ C/m$	$7.61 \cdot 10^{-4}$
sl	Sea level.	m	-
τ	Stress tensor.	Pa	-
τ_b	Basal drag.	Pa	-
τ_s	Lateral drag	Pa	-
B_{sl}	Basal sliding coefficient.	-	-
C_{sl}	Basal sliding coefficient.	-	-
c_f	Basal drag coefficient.	-	$10^{-5} - 10 \cdot 10^{-5}$
σ_b	Backpressure	-	
τ^D	Stress deviator tensor.	Pa	-
τ^*	Effective stress.	Pa	-
$\mathbf{D}$	Strain rate tensor.	1/s	-
η	Ice viscosity.	Pa/yr	-
$\dot{m}$	Basal melt rate.	m/yr	-
L_f	Latent heat of fusion.	J/kg	$3.34 \cdot 10^5$
c_{pW}	Seawater heat capacity	J/kgK	3974
C_d	Ice-water drag coefficient	-	$-3.5 \cdot 10^{-3}$
T_{mp}	Pressure-melting point.	°C	-
T_b	Basal ice temperature.	°C	-
G_h	Geothermal heat flux.	W/m^2	-
n	Glen's flow law exponent.	-	3
Pr	Prandtl number.	-	13.8
Sc	Schmidt number.	-	2432
Re	Reynolds number.	-	
Ω	Earth's frequency of rotation		
E_0	Entrainment constant.	-	0.072
R	Universal gas constant.	J/mol kg	8.3145
A_0	Pre-exponential coefficient.	Pa	-
c	Ice heat capacity.	Jkg/K	2009
κ	Ice thermal conductivity.	W/mK	2.1
Q_i	Ice deformational heat.	W/°Cm	-
τ_{xz}, τ_{yz}	Horizontal shear stresses.	Pa	-
τ_{xx}, τ_{yy}, τ_{xy}	Horizontal longitudinal stresses.	Pa	-
s_m	Surface mass balance.	m/yr	-
b_m	Basal mass balance	m/yr	-
N	Effective pressure.	kg/m^3	-
$H_{calving}$	Thickness threshold for the calving criterion.	m	100 - 300

Next page

From previous page

Symbol	Description	Units	Value
z_b	Shelf depth.	m	-
z_m	Depth threshold for ocean basal melting.	m	-
F_{melt}	Tuning parameter for Martin et al. 2011	-	0.005
K_{shelf}	Tuning parameter for Pollard & DeConto 2012	-	1 - 8

Table A.1: List of symbols and physical constants.

Acronym	Meaning
SSA	Shallow Shelf Approximation.
SIA	Shallow Ice Approximation.
ISW	Ice Shelf Water
CDW	Circumpolar Deep Water
$mCDW$	Modified Circumpolar Deep Water
$HSSW$	High Salinity Shelf Water
SW	Shelf Water
$AASW$	Antarctic Shelf Water
$AABW$	Antarctic Bottom Water
$NADW$	North Atlantic Deep Water
$AAIW$	Antarctic Intermediate Water
ACC	Antarctic Circumpolar Current
$MISI$	Marine Ice Sheet Instability
LGM	Last Glacial Maximum
TG	Totten Glacier
PIG	Pine Island Glacier
AIS	Antarctic Ice Sheet
$WAIS$	West Antarctic Ice Sheet
$EAIS$	East Antartic Ice Sheet
SLR	Sea Level Rise
SMB	Surface Mass Balance

Table A.2: List of acronyms

A.2 Ua and GRISLI numerical details

Ua All the runs have been performed employing a quadratic six-nodes elements and a time step automatically adjusted between 0.01 to 1 years.

GRISLI In table A.3 are reported the parameters value used in GRISLI in the chapter 3 experiments.

Symbol	Description	Unit	Value
ρ	Ice density.	kg/m^3	917
c_f	Basal drag coefficient.	-	10^{-5}
E	Enhancement factor.	-	3
n	Glen's flow law exponent.	-	3
λ	Lapse-rate value.	°C/km	4-8.2
γ	Precipitation-correction factor.	1/°C	0.03-0.1

Table A.3: List of GRISLI paramater values for chapter 3 experiments.

A.3 Additional figures

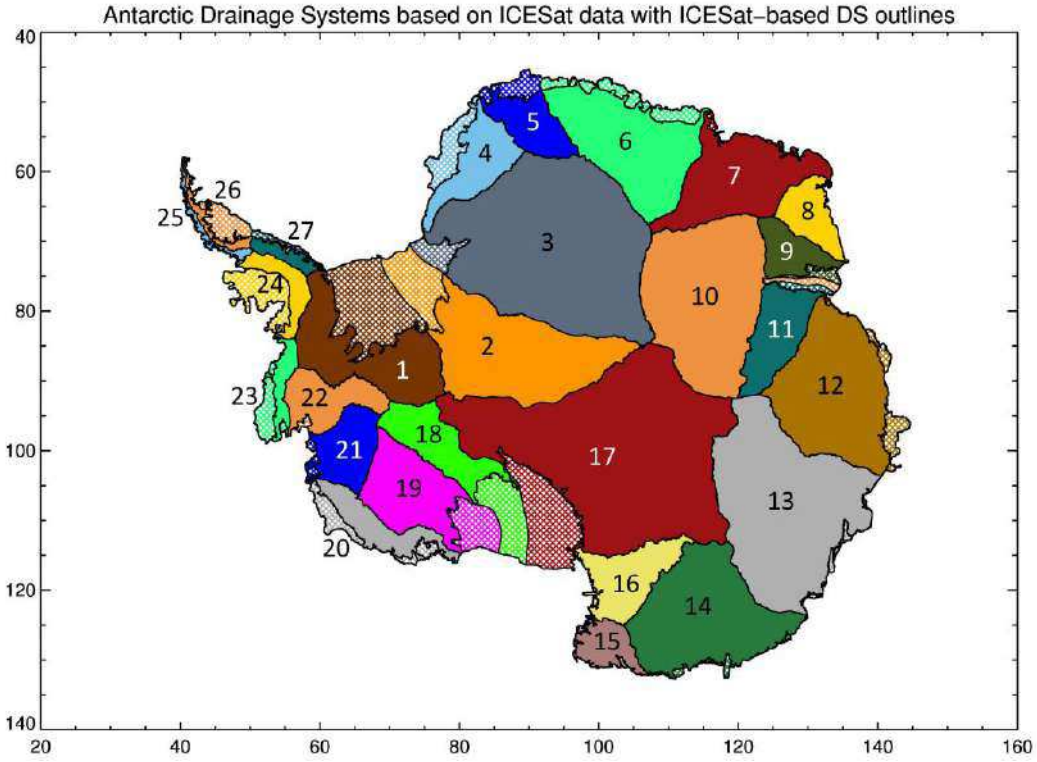

Figure A.1: *Antarctic drainage systems. The numbers on Antartica are the drainage system id's. The portions of the drainage systems within the grounding line are filled with solid color. The portions between the grounding line and the coastline are hatched. Drainage basin 22: Pine Island Glacier. Drainage basin 13: Totten Glacier (from Zwally et al. , 2012)*

Bibliography

Alvarez-Solas, J., Charbit, S., Ritz, C., Paillard, D., Ramstein, G., & Dumas, C. (2010). Links between ocean temperature and iceberg discharge during heinrich events. *Nature Geoscience*, 3(2), 122–126.

Arthern, R. J. & Gudmundsson., G. H. (2010). Initialization of ice-sheet forecasts viewed as an inverse robin problem. *Journal of Glaciology*, 56(197), 527 – 533.

Asay-Davis, Cornford, Galton-Fenzi, Gladstone, Gudmundsson, Holland, & Martin (2016). Experimental design for three interrelated marine ice sheet and ocean model intercomparison projects: Mismip v. 3 (mismip+), isomip v. 2 (isomip+) and misomip v. 1 (misomip1). *Geoscientific Model Development*, 112(11), 3263–3268.

Bamber, Jonathan L., e. a. (2009). Reassessment of the potential sea-level rise from a collapse of the West Antarctic Ice Sheet. *Science*, 324(5929), 901 – 903.

Barber, D. & Massom. (2007). The role of sea ice in arctic and antarctic polynyas. *Elsevier Oceanography Series*, (pp. 1–54).

Bassis, J. N. (2011). The statistical physics of iceberg calving and the emergence of universal calving laws. *Journal of Glaciology*, 57(201), 3 – 16.

Beckmann, A. & Goosse, H. (2003). A parameterization of ice shelf–ocean interaction for climate models. *Ocean modelling*, 5(2), 157–170.

Benn, D., Evans, D. J., et al. (2014). *Glaciers and glaciation*. Routledge.

Bindschadler, Vaughan, & Vornberger (2011). Variability of basal melt beneath the Pine Island Glacier ice shelf, West Antarctica. . *Journal of Glaciology*, 57(204), 581–595.

Bindschadler, R. (2006). The environment and evolution of the West Antarctic ice sheet: setting the stage. *Philosophical Transactions of the Royal Society of London A: Mathematical, Physical and Engineering Sciences*, 364(1844), 1583–1605.

Charbit, S., Ritz, C., & Ramstein, G. (2002). Simulations of northern hemisphere ice-sheet retreat:: sensitivity to physical mechanisms involved during the last deglaciation. *Quaternary Science Reviews*, 21(1), 243–265.

Cofaigh, Pudsey, D. & Morris (2002). Evolution of subglacial bedforms along a paleoice stream, Antarctic Peninsula continental shelf. *Geophysical Research Letters*, 29(8).

Colleoni, F. et al. (2015). Grenoble ice-shelf and land-ice model: a practical user guide. *CMCC Research Paper*.

Colleoni, F., Quiquet, A., & Masina, S. (2016). *Long-term safety of a planned geological repository for spent nuclear fuel in Forsmark – Phase 2: Impact of ice sheet dynamics, climat forcing and multi-variate sensitivity analysis on maximum ice sheet thickness*. Technical Report SKB TR-14-21, Swedish Nuclear Fuel and Waste Management Co, Stockholm, Sweden.

Colleoni, F., Wekerle, C., & Masina, S. (2014). *Long-term safety of a planned geological repository for spent nuclear fuel in Forsmark – Phase 1: Estimate of maximum ice sheet thicknesses*. Technical Report SKB TR-14-21, Swedish Nuclear Fuel and Waste Management Co, Stockholm, Sweden.

Cornford, Martin, G. & Lipscomb (2013). Adaptive mesh, finite volume modeling of marine ice sheets. *Journal of Computational Physics*, 232(1), 529–549.

Cornford, Martin, T. & Vaughan (2015). Century-scale simulations of the response of the west antarctic ice sheet to a warming climate. *Oceanology of the Antarctic continental shelf*, 9, 1579–1600.

DeConto, R. M. & Pollard, D. (2016). Contribution of Antarctica to past and future sea-level rise. *Nature*, 531, 591–597.

Depoorter, M., Bamber, J., Griggs, J., Lenaerts, J., Ligtenberg, S., Van den Broeke, M., & Moholdt, G. (2013). Calving fluxes and basal melt rates of antarctic ice shelves. *Nature*, 502(7469), 89–92.

Dinniman, Holland, J. & Timmermann (2016). Modeling ice shelf ocean interaction in Antarctica: A review. *Oceanography*, 29(4), 144–153.

Docquier, David, L. P. & Pattyn., F. (2011). Representing grounding line dynamics in numerical ice sheet models: recent advances and outlook. *Surveys in geophysics*, 32(4 - 5), 417 – 435.

Douglas Benn, D. E. (2010). *Glaciers and Glaciation, 2nd edition.* Hodder Arnold Publication.

Dumas, C. (2002). *Modélisation de l'évolution de l'Antarctique depuis le dernier cycle glaciaire-interglaciaire jusqu'au futur: importance relative des différents processus physiques et rôle des données d'entrée.* PhD thesis, Université Joseph-Fourier-Grenoble I.

Durand, Gaël, e. a. (2009). Marine ice sheet dynamics: Hysteresis and neutral equilibrium. *Journal of Geophysical Research: Earth Surface*, 114(F3).

Dutrieux, Vaughan, Corr, Jenkins, & Holland (2013). Pine Island glacier ice shelf melt distributed at kilometre scales. *The Cryosphere*, 7(5).

et al., T. (2017). Foehn-induced surface melting of the larsen c ice shelf, antarctica. *EGU General Assembly Conference Abstracts.*, 19.

Favier, Durand, C. & Gudmundsson (2014). Retreat of pine island glacier controlled by marine ice-sheet instability. *Nature Climate Change*, 4(2), 117 – 121.

Foldvik, A. & Gammelsrød., T. (1988). Notes on Southern Ocean hydrography, sea-ice and bottom water formation. *Palaeogeography, Palaeoclimatology, Palaeoecology*, 67(2), 3–17.

Fretwell, Pritchard, Bamber, & Catania (2013). Bedmap2: improved ice bed, surface and thickness datasets for Antarctica. *The Cryosphere*, 7(1).

Fricker, Helen Amanda, e. a. (2001). Distribution of marine ice beneath the Amery Ice Shelf. *Gephysical Research letters*, 28(11), 2241–2244.

Gladstone, R. M., e. a. (2010). Grounding line migration in an adaptive mesh ice sheet model. *Journal of Geophysical Research: Earth Surface*, 115(F4).

Glasser, N. F. & Scambos, T. A. (2008). A structural glaciological analysis of the 2002 larsen b ice-shelf collapse. *Journal of glaciology*, 54(184), 3 – 16.

Greenbaum, Young, & Siegert (2015). Ocean access to a cavity beneath totten glacier in east antarctica. *Nature Geoscience*, 8(4), 294–298.

Greve, R. & Blatter, H. (2009). *Dynamics of ice sheets and glaciers*. Springer Science & Business Media.

Gudmundsson (2012). The stability of grounding lines on retrograde slopes. *The Cryosphere*, 6, 1497–1505.

Gudmundsson, G. H. & Raymond., M. (2008). On the limit to resolution and information on basal properties obtainable from surface data on ice streams. *The Cryosphere Discussions*, 2(3), 413–445.

Gwyther, Galton-Fenzi, Hunter, & Roberts (2014). Simulated melt rates for the totten and dalton ice shelves. *Ocean Science*, 10(3), 267.

Hellmer, H. H. & Olbers., D. J. (1989). A two-dimensional model for the thermohaline circulation under an ice shelf. *Antarctic Science*, 1(4), 325–336.

Holland & Feltham (2006). The effects of rotation and ice shelf topography on frazil-laden ice shelf water plumes. journal of physical oceanography. *Journal of Geophysical Research: Oceans*, 36(12), 2312–2327.

Holland, D. & Jenkins, A. (1999). Modeling thermodynamic ice–ocean interactions at the base of an ice shelf. *Journal of Physical Oceanography*, 29(8), 1787–1800.

Holland, P., Jenkins, A., & Holland, D. (2008). The response of ice shelf basal melting to variations in ocean temperature. *Journal of Climate*, 21(11), 2558–2572.

Holland, P. R., Feltham, D. L., & Jenkins., A. (2007). Ice shelf water plume flow beneath filchner ronne ice shelf, antarctica. *Journal of Geophysical Research: Oceans*, 112(C5), 2312–2327.

Hutter, K. (1983). *Theoretical glaciology: material science of ice and the mechanics of glaciers and ice sheets*, volume 1. Springer.

Jacobs, Stanley S., e. a. (2011). Stronger ocean circulation and increased melting under pine island glacier ice shelf. *Nature Geoscience*, 4(8), 519.

Jacobs, S. (1992). Melting of ice shelves and the mass balance of Antarctica. *Journal of glaciology*, 38(130), 375–387.

Jenkins & Holland., D. (2007). Melting of floating ice and sea level rise. *Geophysical Research Letters*, 34(16).

Jenkins, A. (1991). A one dimensional model of ice shelf ocean interaction. *Journal of Geophysical Research: Oceans*, 96(C11), 20671–20677.

Jenkins, A. & Bombosch, A. (1995). Forced, angled plumes. *Journal of Geophysical Research: Oceans*, 100(C4), 6967–6981.

Jenkins, Adrian, e. a. (2010). Observations beneath pine island glacier in west antarctica and implications for its retreat. *Nature Geoscience*, 3(7), 468.

Joughin, Ian, e. a. (2003). Timing of recent accelerations of Pine Island glacier, Antarctica. *Geophysical Research Letters*, G30(13).

Joughin, I. & Alley, R. B. (2011). Stability of the west antarctic ice sheet in a warming world. *Nature Geoscience*, 4(8), 506–513.

Joughin, S. & Medley (2008). Marine ice sheet collapse potentially under way for the thwaites glacier basin, west antarctica. *Science*, 344(6185), 735 – 738.

Joughin, Benjamin, S. & Holland, D. (2010). Sensitivity of 21st century sea level to ocean induced thinning of pine island glacier. *Geophysical Research Letters*, 37(20).

Kader, B. A. & Yaglom, A. M. (1972). Heat and mass transfer laws for fully turbulent wall flows. *Int. J. Heat Mass Transfer*, 23(17), 2329–2351.

Khazendar, A., e. a. (2013). Observed thinning of totten glacier is linked to coastal polynya variability. *Nature communications*, 4.

Kirchner, N., Hutter, K., Jakobsson, M., & Gyllencreutz, R. (2011). Capabilities and limitations of numerical ice sheet models: a discussion for earth-scientists and modelers. *Quaternary Science Reviews*, 30(25), 3691–3704.

Kulessa, Bernd, e. a. (2017). Impact of surface melt and ponding on the stability of larsen c ice shelf, antarctic peninsula. In *EGU General Assembly Conference Abstracts*.

Lane-Serff, Linden, & Hillel., M. (1993). Forced, angled plumes. *Journal of hazardous materials*, 33(1), 75–99.

Lenaerts, J. T. M., e. a. (2012). A new high resolution surface mass balance map of antarctica (1979–2010) based on regional atmospheric climate modeling. *Geophysical Research Letters*, 39.

Lenaerts, J. T. M., e. a. (2017). Meltwater produced by wind-albedo interaction stored in an east antarctic ice shelf. *Nature climate change*, 7, 58–62.

Levermann, Albrecht, W. & Joughin (2012). Kinematic first-order calving law implies potential for abrupt ice-shelf retreat. *The Cryosphere*, 6(2), 273.

Lewi & Perkin (1986). Ice pumps and their rates. *Journal of Geophysical Research: Oceans*, 91(10), 11756–11762.

Li, X., Rignot, E., Morlighem, M., Mouginot, J., & Scheuchl, B. (2015). Grounding line retreat of totten glacier, east antarctica, 1996 to 2013. *Geophysical Research Letters*, 42(19), 8049–8056.

Ligtenberg, Helsen, M. M., & Van den Broeke, M. R. (2011). An improved semi-empirical model for the densification of antarctic firn. *The Cryosphere*, 5(4).

Linny, T. (2016). *Descriptive Physical Oceanography*. Elsevier.

Liu, Moore, Cheng, Gladstone, Bassis, Liu, & Hui (2015). The glimmer community ice sheet model. *Proceeding of the National Academy of Sciences*, 112(11), 3263–3268.

Lythe C., M. B. & Vaughan, D. G. (2001). Bedmap: A new ice thickness and subglacial topographic model of antarctic. *Journal of Geophysical Research: Solid Earth*, 106(6), 11335–11351.

MacAyeal, D. R. (1985). Evolution of tidally triggered meltwater plumes below ice shelves. *Oceanology of the Antarctic continental shelf*, (pp. 133–143).

MacAyeal, D. R. (1989). Large-scale ice flow over a viscous basal sediment: Theory and application to ice stream b, antarctica. *Journal of Geophysical Research: Solid Earth*, 94(B4), 4071–4087.

Madec, G. (2015). Nemo ocean engine.

Marchant, D. R., e. a. (2002). Formation of patterned ground and sublimation till over Miocene glacier ice in Beacon Valley, southern Victoria Land, Antarctica. *Geological Society of America Bulletin*, 114(6), 718–730.

Marsiat, I. (1994). Simulation of the northern hemisphere continental ice sheets over the last glacial-interglacial cycle: experiments with a latitude-longitude vertically integrated ice sheet model coupled to a zonally averaged climate model. *Paleoclimates*, 59(58).

Martin, M., Winkelmann, R., Haseloff, M., Albrecht, T., Bueler, E., Khroulev, C., & Levermann, A. (2011). The potsdam parallel ice sheet model (pism-pik)–part 2: Dynamic equilibrium simulation of the antarctic ice sheet. *The Cryosphere*, 5(3), 727–740.

Mathiot, Jenkins, Harris, C., & Madec, G. (2017). Explicit representation and parametrised impacts of under ice shelf seas in the z coordinate ocean model nemo 3.6. *Geoscientific Model Development*, 10(7).

Mercer, J. H. (1978). West Antarctic ice sheet and CO2 greenhouse effect: a threat of disaster. *Nature*, 271(5643), 321–325.

Millero, Frank J., A. L. S. & Shin., C. (1978). The apparent molal volumes and adiabatic compressibilities of aqueous amino acids at 25. degree. C. *The Journal of Physical Chemistry*, 82(7), 784–792.

Orsi S., Alejandro H., T. W. & Nowlin., W. D. (1995). On the meridional extent and fronts of the antarctic circumpolar current. *Deep Sea Research Part I: Oceanographic Research Papers*, 42(5), 641–673.

Park, J. W., e. a. (2013). Sustained retreat of the pine island glacier. *Geophysical Research Letters*, 40(10), 2137 – 2142.

Paterson, W. (1994). *The physics of glaciers*. Butterworth-Heinemann.

Pattyn, Frank, e. a. (2012). Results of the marine ice sheet model intercomparison project, mismip. *The Cryosphere*, 6(3), 573–588.

Pattyn, Frank, e. a. (2013). Grounding-line migration in plan-view marine ice-sheet models: results of the ice2sea mismip3d intercomparison. *Journal of Glaciology*, 59(215), 410–422.

Peyaud, V. (2006). *Rôle de la dynamique des calottes glaciaires dans les grands changements climatiques des périodes glaciaires-interglaciaires.* PhD thesis, Université Joseph-Fourier-Grenoble I.

Peyaud, V., Ritz, C., & Krinner, G. (2007). Modelling the early weichselian eurasian ice sheets: role of ice shelves and influence of ice-dammed lakes. *Climate of the Past Discussions*, 3(1), 221–247.

Pollard, D. & DeConto, R. M. (2009). Modelling west antarctic ice sheet growth and collapse through the past five million years. *Nature*, 458(7236), 329–332.

Pollard, D. & DeConto, R. M. (2012). Description of a hybrid ice sheet-shelf model, and application to Antarctica. *Geoscience Model Development*, 5, 1273–1295.

Pritchard, H., Ligtenberg, S., Fricker, H., Vaughan, D., Van den Broeke, M., & Padman, L. (2012). Antarctic ice-sheet loss driven by basal melting of ice shelves. *Nature*, 484(7395), 502–505.

Reeh, N. (1989). Parameterization of melt rate and surface temperature on the greenland ice sheet. *Polarforschung*, 59(3), 113–128.

Rignot, Jacobs, Mouginot, & Scheuchl (2013). Ice-shelf melting around antarctica. *Science*, 341(6143), 266–270.

Rignot, Bamber, D. & Meijgaard, V. (2008). Recent antarctic ice mass loss from radar interferometry and regional climate modelling. *Nature geoscience*, 1, 106–110.

Rignot, E. & Thomas., R. H. (2002). Mass balance of polar ice sheets. *Science*, 297(5586), 1502–1506.

Rignot, E. J. (1998). Fast recession of a west antarctic glacier. *Science*, 281(5376).

Rignot, E., J. M. & Scheuchl., B. (2011). Ice flow of the antarctic ice sheet. *Science*, 333(6048), 1427–1430.

Rignot, Jacobs, M. & Scheuchl (2014). Widespread, rapid grounding line retreat of pine island, thwaites, smith, and kohler glaciers, west antarctica, from 1992 to 2011. *Geophysical Research Letters*, 41(10), 3502 – 3509.

Rintoul, S. R., Silvano, A., Pena-Molino, B., van Wijk, E., Rosenberg, M., Greenbaum, J. S., & Blankenship, D. D. (2016). Ocean heat drives rapid basal melt of the totten ice shelf. *Science advances*, 2(12).

Ritz, C., Rommelaere, V., & Dumas, C. (2001). Modeling the evolution of antarctic ice sheet over the last 420,000 years: Implications for altitude changes in the vostok region. *Journal of Geophysical Research: Atmospheres*, 106(D23), 31943–31964.

Ritz, Catherine, e. a. (2015). Potential sea-level rise from antarctic ice-sheet instability constrained by observations. *Nature*, 528(7580).

Rott, Helmut, P. S. & Nagler., T. (1996). Rapid collapse of northern larsen ice shelf, antarctica. *Science*, 271(5250), 788.

R.W. Lewis, P. & Seetharamu., K. N. (2004). *Fundamentals of the Finite Element Method for Heat and Fluid Flow*. Wiley Ltd.

Rydt, D. & Gudmundsson (2016). Coupled ice shelfocean modeling and complex grounding line retreat from a seabed ridge. *Geophysical Research: Earth Surface*, 121(5), 865–880.

Sato, T. & Greve, R. (2012). Sensitivity experiments for the antarctic ice sheet with varied sub-ice-shelf melting rates. *Annals of Glaciology*, 53(60), 221–228.

Scambos, Ted, C. H. & Fahnestock., M. (2003). Antarctic peninsula climate variability: Historical and paleoenvironmental. *Earth and Planetary Science Letters*, 79(92), 79–92.

Scambos, Ted A., e. a. (2000). The link between climate warming and break-up of ice shelves in the antarctic peninsula. *Journal of Glaciology*, 46(154), 516 – 530.

Scambos, Ted A., e. a. (2004). Glacier acceleration and thinning after ice shelf collapse in the larsen b embayment, antarctica. *Geophysical Research Letters*, 31.

Schoof, C. (2007). Ice sheet grounding line dynamics: Steady states, stability, and hysteresis. *Journal of Geophysical Research: Earth Surface*, 112.

Shepherd, Andrew, e. a. (2001). Inland thinning of pine island glacier, west antarctica. *Science*, 291(5505), 862 – 864.

Siegert, Martin J., e. a. (2008). Recent advances in understanding Antarctic climate evolution. *Antarctic Science*, 20(4), 313–325.

Silvano, A., Rintoul, & Herraiz-Borreguero (2016). Oceanice shelf interaction in East Antarctica. *Oceanography*, 29(4), 130–143.

Smedsrud, L. H. & Jenkins, A. (2004). Frazil ice formation in an ice shelf water plume. *Journal of Geophysical Research: Oceans*, 109(C3), 20671–20677.

Solomon, S., Qin, S., Manning, M., Chen, Z., Marquis, M., Averyt, K., Tignor, M., & Miller, H. (2007). *IPCC, 2007: The Physical Science Basis. Contribution of Working Group I to the Fourth Assessment Report of the Intergovernmental Panel on Climate Change*. Cambridge University Press, Cambridge, United Kingdom and New York, NY, USA.

Sun, Cornford, Gladstone, & Moore (2016). Impact of ocean forcing on the aurora basin in the 21st and 22nd centuries. *Annals of Glaciology*, 57(73), 79–86.

Sun, Liu, & Moore (2014). Dynamic response of antarctic ice shelves to bedrock uncertainty. *The Cryosphere*, 8(4), 1561–1576.

Thoma, Malte, e. a. (2008). Modelling circumpolar deep water intrusions on the amundsen sea continental shelf, antarctica. *Geophysical Research Letters*, 35(18), 1427 – 1434.

Thomas, R. H. (1973). The creep of ice shelves: theory. *Journal of Glaciology*, 12(64), 45–53.

Thomas, R. H. (1979). The dynamics of marine ice sheets. *Journal of Glaciology*, 24(90), 167–177.

Turner, John, e. a. (2005). Antarctic climate change during the last 50 years. *International journal of Climatology*, 25(3), 279 – 294.

Turner, J. S. (1989). Turbulent entrainment: the development of the entrainment assumption, and its application to geophysical flows. *Journal of Fluid Mechanics*, 173, 431–471.

Van der Veen, C. (2017). *Fundamentals of Glacier Dynamics, Second Edition.* CRC press.

Van der Veen, C. J. (1985). Response of a marine ice sheet to changes at the grounding line. *Quaternary Research*, 24(3), 257 – 267.

Vaughan, D. G. (2008). West antarctic ice sheet collapse–the fall and rise of a paradigm. *Climate Change*, 91(1), 65–79.

Wahlin, A. K., e. a. (2010). Inflow of warm circumpolar deep water in the central amundsen shelf. *Journal of Physical Oceanography*, 40(6), 1427 – 1434.

Weertman, J. (1957). Steady-state creep through dislocation climb. *Journal of Applied Physics*, 28(3), 362–364.

Weertman, J. (1974). Stability of the junction of an ice sheet and an ice shelf. *Journal of Glaciology*, 13(67), 3–11.

Zwally, H. J., Giovinetto, M. B., Beckley, M. A., & Saba, J. L. (2012). Antarctic and Greenland Drainage Systems. *Cryospheric Sciences Laboratory.*